UNIVERSITY OF SOUTHAMPTON

Faculty of Engineering and Physical Sciences
School of Engineering

The Impact of Surface Texture on the Hydrodynamics of Aquatic Locomotion

by

Jonathan Massey

ORCiD: 0000-0002-2893-955X

A thesis for the degree of
Doctor of Philosophy

March 2024

University of Southampton

Abstract

Faculty of Engineering and Physical Sciences
School of Engineering

Doctor of Philosophy

The Impact of Surface Texture on the Hydrodynamics of Aquatic Locomotion

by Jonathan Massey

Fish have evolved over millions of years, achieving a level of swimming efficiency that far surpasses current human-engineered capabilities. A prevalent feature in many species is skin scales. Scholars posit that this surface texture may offer hydrodynamic advantages, although the mechanisms remain poorly understood. This thesis investigates the effect of roughness on aquatic locomotion. Utilising a combination of numerical simulations and innovative analysis methods, we investigate the intricate interplay between low-parameter, egg-carton-type surface roughness and self-propelled swimming. Our findings indicate that both the roughness wavelength and kinematics are instrumental in shaping the flow structures and power requirements. We observe that scaling the roughness wavelength with the boundary-layer thickness significantly enhances flow mixing, without a proportional increase in forces. Furthermore, the boundary layer of a swimming foil displays fundamentally unstable spatial structures, directly attributable to the swimming motion. This suggests that actuation at the wall could be an effective mechanism to stabilise the boundary layer. Additionally, we probe a parameter space concerning potential stabilising roughness shapes. We demonstrate that surface roughness can be used to improve swimming performance and that variable roughness functions could potentially outperform fixed small-scale roughness, given proper tuning. Our results reveal that the interaction between roughness and kinematics is complex and nonlinear, suggesting that roughness studies on static shapes do not transfer directly to unsteady swimmers.

Contents

List of Figures

List of Tables

Declaration of Authorship

I declare that this thesis and the work presented in it is my own and has been generated by me as the result of my own original research.

I confirm that:

1. This work was done wholly or mainly while in candidature for a research degree at this University;
2. Where any part of this thesis has previously been submitted for a degree or any other qualification at this University or any other institution, this has been clearly stated;
3. Where I have consulted the published work of others, this is always clearly attributed;
4. Where I have quoted from the work of others, the source is always given. With the exception of such quotations, this thesis is entirely my own work;
5. I have acknowledged all main sources of help;
6. Where the thesis is based on work done by myself jointly with others, I have made clear exactly what was done by others and what I have contributed myself;
7. Parts of this work have been published as:

    - Massey, J., Ganapathisubramani, B., and Weymouth, G. (2023). A systematic investigation into the effect of roughness on self-propelled swimming plates. *Journal of Fluid Mechanics*, 971:A39

Signed:..... Date:.....

To Mum and Dad, for kindling my curiosity.

Acknowledgements

First and foremost: thank you to Gabe and Bharath for keeping me on track; this thesis would be an incoherent jumble of thoughts without you. Thanks also to Andhini and Marin for answering all my *Lotus* questions; I'd still be stuck trying to compile it without you. Thank you to Rodrigo, your reciprocated frustration at the trials and tribulations of having human supervisors has been a vast comfort, and a welcome outlet. Thanks to Leo, and James, and all the Weymouth group affiliates for the hive mind insights. Thank you to everyone at Southampton and at Delft for your company; I have learnt a lot about the world over lunch. Lastly, thank you to my family, and to Emily, your patience and support has been invaluable, I couldn't have done it without you.

Nomenclature

Acronyms

BDIM	Boundary Data Immersion Method
PSD	Power spectral density.
SDF	Signed Distance Function
SPS	Self-propelled swimming

Matrices

Λ	Eigenvalues.
A	Linear operator.
D	Diagonal matrix or singular values.
V	Direct eigenvectors.
W	Adjoint eigenvectors.

Operators

$\cdot^*$	Complex conjugate.
$\cdot^+$	Adjoint.
$\cdot^\dagger$	Pseudo inverse.
$\mathcal{B}$	Body governing equation.
$\mathcal{F}$	Fluid governing equation.
$\mathcal{K}_\epsilon$	Convolution kernel with radial support ϵ.
$\mathcal{M}$	Meta-equation.
$\oint$	Integral around a closed curve.
$\bar{\cdot}$	Average in time.

$\vec{\nabla}$ Gradient operator.

Scalars

ν Kinematic viscosity.

ρ Density.

p Pressure.

t Time.

α Angle of attack.

δt Time step.

Δx Grid spacing in the x direction.

Δy Grid spacing in the y direction.

Δz Grid spacing in the z direction.

δ Boundary-layer thickness.

ϵ Radius of the smoothing kernel.

η^n Error at time n.

κ Curvature.

λ Wavelength of the roughness.

$\mathcal{A}$ Autocorrelation.

μ Dynamic viscosity.

$\mu_{0,1}$ First and second moments of the cosine kernel.

ω Angular frequency

Re The Reynolds number.

φ The frequency normalised time ($2\pi ft$).

ς Singular values.

ζ Phase speed of the travelling wave.

$A(x)$ Amplitude envelope.

A_1 Amplitude of the trailing edge.

a_i Polynomial coefficients.

b Intermediate velocity field divergence.

C_L Lift coefficient.

C_P Pressure coefficient.

C_T Thrust coefficient.

d Euclidean distance from the kernel.

f Frequency of the undulation.

h Bump amplitude.

k_x Streamwise wavenumber.

L Body length.

m Truncation of modes.

n_x Number of grid points in the x direction.

n_y Number of grid points in the y direction.

n_z Number of grid points in the z direction.

r Radius of the bump.

r^n Residual at time n.

S Planform area of the plate.

sb Bump spacing.

St Strouhal number.

t_{total} Total simulation time.

(n, s) Normal, tangential body coordinates.

Vectors

$\vec{u}$ Velocity vector.

$\vec{x}$ Spatial vector.

$\hat{n}$ Unit vector normal to the body.

$\hat{y}$ Unit vector in the vertical direction.

$\vec{f}$ Force vector.

$\vec{N}$ Total number of grid cells in the computational domain.

$\vec{U}$ Uniform inflow velocity.

$\vec{v}(\vec{x}, t)$ Body velocity.

M Discretised Laplacian operator.

Chapter 1

Introduction

Modern homo-sapiens have existed for a mere 160,000 years. Yet in that time we have wrought irreparable damage on the ecosystems that support us. Our engineering prowess, once a beacon of human ingenuity, now casts a dark shadow over the oceans. Our monstrous vessels stand as stark monuments to our disconnection from the natural world.

Consider the colossal drill ships that plunge deep into the ocean floor. They are not mere structures but invasive species in our marine landscapes. Their presence disrupts delicate aquatic ecosystems, often leading to catastrophic oil spills like the 780,000m^3 Deepwater Horizon (BP) spill (NRT Response Committee, 2011). Such spills do not merely stain our shores; they asphyxiate marine life, smother coral reefs, and poison the intricate food webs that sustain countless species, including our own.

This relentless assault on the natural world reflects a deeper malaise: our belief that the ocean is an inexhaustible resource for exploitation and a convenient dumping ground for our wastes. We have forgotten that the ocean is a living, breathing entity, a complex ecosystem that sustains all life on Earth. We have forgotten that we are part of this ecosystem, not apart from it. We stand at a crossroads. Our engineering feats, once symbols of progress, now need to be reimagined in harmony with the rhythms of the ocean. We must shift from exploiters to stewards, respecting the intricate web of life beneath the waves, to preserve the marine world not only for its inhabitants but for future generations of humankind.

Evolution encodes a reservoir of knowledge into the designs of aquatic creatures, honing their forms over millions of years to navigate the fluid dynamics of water with maximum efficiency. One curiosity of fishes evolution is that the vast majority of species has developed some sort of surface texture in the form of scales. This adaptive pathway leads us to query the traditionally held beliefs that we must do everything to reduce surface roughness. The caveat, of course, is that fish do not adhere to the channel

flow physics of traditional roughness studies. Their motion is composed of a balance between propulsive pressure forces, and drag inducing friction forces. The study of the interaction between surface textures and kinematics in aquatic locomotion is, therefore, a step towards understanding the potential benefits of surface textures in engineering systems of the future.

1.1 Kinematics

Underwater propulsion is an area of research that brings together engineers and biologists alike; it has fostered a deeper understanding of aquatic locomotion and inspired innovation in underwater systems. The kinematics have the most significant effect on the locomotive properties of marine animals (Lighthill, 1960, 1971; Triantafyllou et al., 1991, 1993; Borazjani and Sotiropoulos, 2008; Eloy, 2012; Saadat et al., 2017; Di Santo et al., 2021); however, some intricacies of animal evolution, such as the skins of sharks and odontocetes, have sparked research into the benefits of aquatic surface textures. Understanding the fluid dynamic interaction between kinematics and surface textures will help us to elucidate the contribution of surface textures to aquatic locomotion.

Previous work has identified important non-dimensional kinematic parameters for efficient swimming. The Reynolds number (Re) affects the efficiency of swimmers which can be in the viscous ($Re \approx 10^2$), transitional ($Re \approx 10^3$), and inertial ($Re \to \infty$) regime (Borazjani and Sotiropoulos, 2008, 2010). The Strouhal number (St) describes the ratio between the product of the wake width and the shedding frequency, and the flow velocity; Triantafyllou et al. (1991, 1993) found that the optimal Strouhal number should be in the range $0.25 - 0.35$. Eloy (2012) tested the kinematics of fifty-three different types of fish based on Lighthill's elongated body theory (Lighthill, 1960, 1971) and found that for thin tails, the optimal Strouhal number range was $0.2 - 0.4$. Saadat et al. (2017) showed that the Strouhal number was insufficient for efficient locomotion and defined a range of optimum motion amplitude to length ratio of 0.05 to 0.15. Di Santo et al. (2021) recently compared forty-four species of fishes and found that despite fishes' different morphologies—categorised as; anguilliform, subcarangiform, carangiform, and thunniform—they shared a statistically significant oscillation amplitude, a.k.a. kinematic envelope. This work is noteworthy as previous work suggested the presence of different kinematics was dependent on the morphology.

Self-propelled swimming (SPS) is defined as the constant movement of a swimmer through water solely through its own effort, without the influence of any external forces. The study of fish models under SPS facilitates the evaluation of a swimmer's performance under migratory conditions, where efficiency is of utmost importance. Significant efforts have been made to assess the realistic performance of this swimming mode, aiming to understand the key parameters involved. One model of SPS is a

tethered swimming scenario. This is where the x position of the swimmer is fixed, and the kinematics, or the inflow velocity is changed to centre the forces around a zero mean. This is experimentally feasible and has facilitated a number of works (Anderson, 1996; Ulrike K Müller et al., 2001; Zhu et al., 2002; Drucker, 2002; Nauen and Lauder, 2002; Tytell and Lauder, 2004; Tytell, 2007; Hultmark et al., 2007; Dewey et al., 2012; Oeffner and Lauder, 2012; Wen et al., 2014). However, throughout a swimming cycle, there is a cyclic variation in the forces that lead to the fish accelerating and decelerating (Hess and Videler, 1984). By solving Newton's equations and the 2-D Navier-Stokes equations simultaneously, Carling et al. (1998) demonstrated that the swimming speed from the coupled model was 0.77 times that of the tethered version. This model was deemed unnecessary for instances where a swimmer's performance is gauged by power requirements rather than its swimming speed; a conclusion supported by Maertens et al. (2017), who discovered that fixing the x location of the foil does not influence the power needed for swimming, aligning with the findings of Bale et al. (2014).

1.2 Surface textures

While kinematics have received the majority of the literature's attention, they are not the only factor affecting the locomotive properties of swimmers. Almost ninety years ago, Sir James Gray conducted work looking at the drag on a swimming dolphin (Gray, 1936). He supposed that dolphins must produce energy at seven times the rate of any known mammalian muscle to overcome drag, the conjecture was later termed *Gray's paradox*. *Gray's paradox* was later found to be false due to Gray's incorrect assumptions of muscle force, but not before sparking a field of research into drag reduction techniques of dolphins' and eventually other animals.

Numerous studies have highlighted the drag-reducing properties of certain textures, though predominantly applied to static geometries. There is, however, a suggestion that these effects could extend to unsteady aquatic propulsion. The channels depicted in figure 1.1, running along the length of the shark, led to its early characterisation as a riblet, as noted by Raschi and Musick (1984). Riblets are small-scale, two-dimensional transverse grooves, scaling with the viscous flow scales, known for their drag-reducing capabilities (see Walsh (1982); Park and Wallace (1994); R García-Mayoral (2011); Cui et al. (2019)). These channels passively reduce drag by diminishing velocity RMS fluctuation near them and by isolating high shear stress regions to the riblet tips, thereby reducing overall drag.

Bechert et al. (1997) explored a range of geometrical parameters for these idealised 2-D extrusions, aiming to optimise drag reduction. They discovered that blade-shaped riblets were most effective, achieving a frictional drag reduction of approximately 10-12%. The potential of riblets for drag reduction, given proper tuning, remains clear. However,

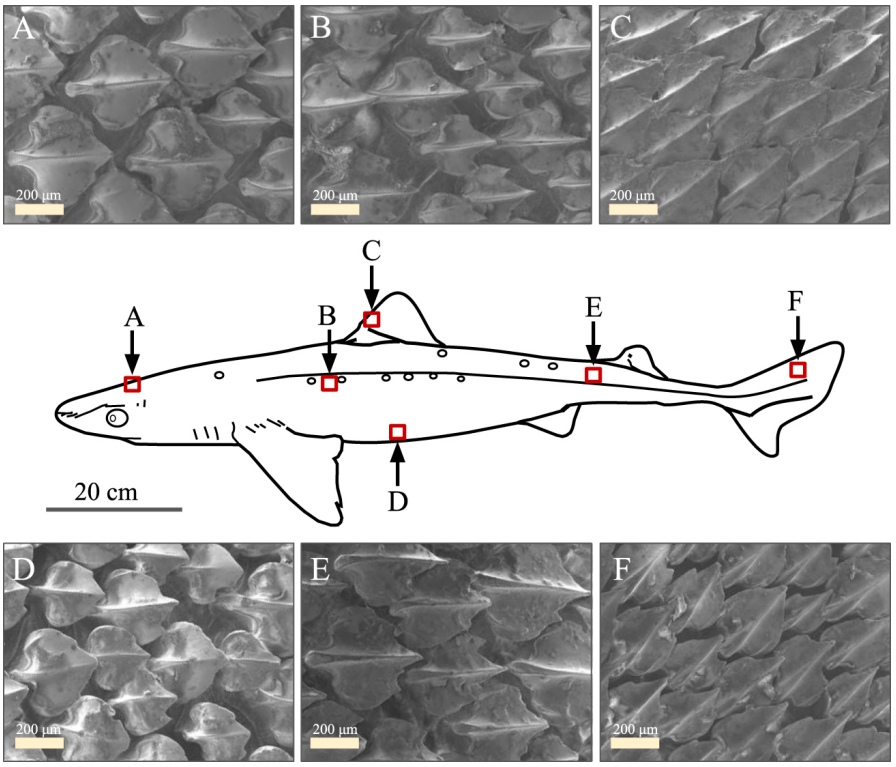

FIGURE 1.1: Figure taken from Guo et al. (2021) showing scanned electron microscopy sections of skin at various key positions along a spiny dogfish.

issues arise if riblets are not viscously scaled or if they possess larger-scale features, such as varied inclinations, which can generate new flow features and potentially increase drag (refer to Bechert et al. (2000a); Nugroho et al. (2013); Boomsma and Sotiropoulos (2016); Von Deyn et al. (2022); Rouhi et al. (2022)).

Moreover, when denticles do not completely interlock, their three-dimensionality may be counterproductive, increasing drag. This was corroborated by Boomsma and Sotiropoulos (2016), who compared two shark denticle shapes with a scallop riblet design using DNS simulations. They observed that the denticles increased drag by 44-50%, while the riblets reduced it by 5% compared to a smooth surface. These findings imply unresolved hydrodynamic issues with shark skin. The non-universality of shark denticles forming perfect riblet grooves and the sensitivity of riblets to specific flow conditions raise questions about their efficacy in enhancing unsteady swimmer performance.

During a swim cycle, the surface of a swimmer might briefly encounter the viscous scales set out by Bechert et al. (2000a) for drag-reduction of riblets however, the morphing of the body and the fluctuating viscous length scales force the near-wall flow outside the conditions that cause riblets to decrease drag the majority of the time. To comprehend the potential hydrodynamic benefit of surface textures, we must look at them in the context of a larger, dynamic system. For example, vortex generators are often low-profile roughness elements that can significantly effect the flow and stimulate massive increases

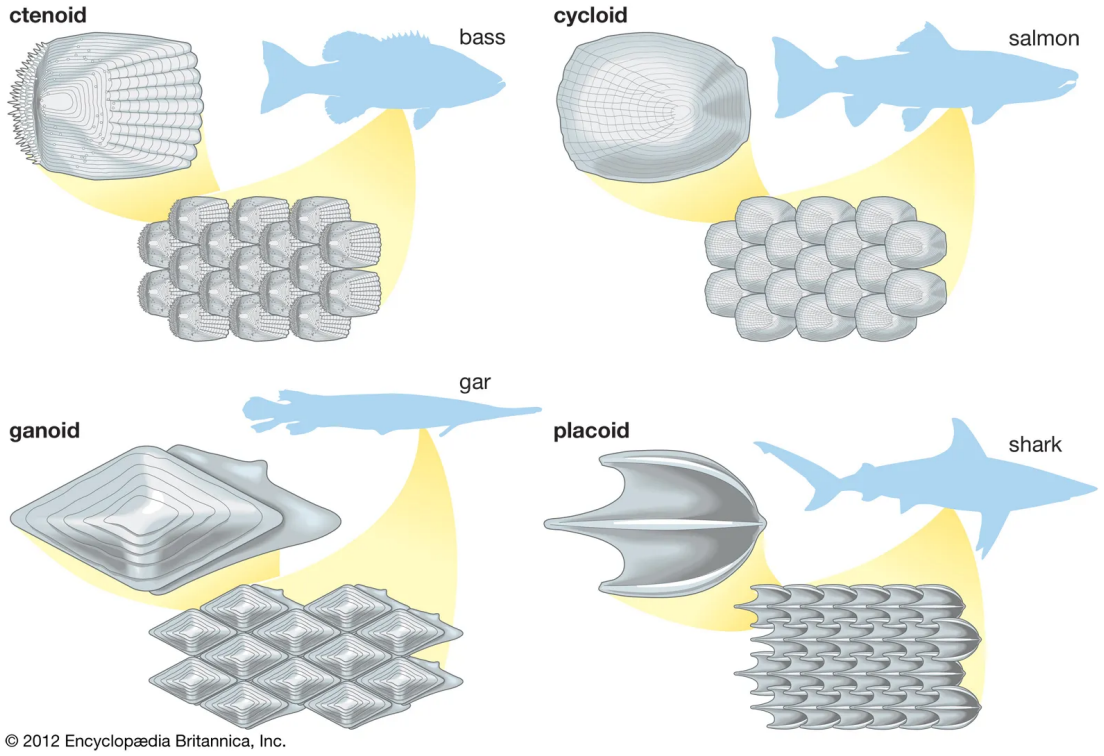

FIGURE 1.2: The diversity of fish scale morphology taken from the

of aerodynamic performance when positioned correctly (Lin et al., 1994; Lin, 2002). Similarly, studies suggest that shark skin uses passive control in the flank region to bristle the skin while swimming, increasing boundary-layer mixing and helping to keep the flow attached at areas of flow reversal Lang et al. (2008); Afroz et al. (2016); Santos et al. (2021). In this vein, Oeffner and Lauder (2012) tested samples of skin from the midsection of a short-fin mako shark on both a rigid flapping plate and a flexible plate. They found that the skin actually reduced the rigid plate's propulsive effectiveness. They also found that adding shark skin increased the flexible plate's swimming speed by 12%. However, they do not provide the amplitude envelope for the flexible plate which would ensure constant kinematics between the cases tested. Similarly, Wen et al. (2014) covered an undulating plate in 3D printed denticles of 100× actual size and measured a 6.6% efficiency increase. Again, they do not provide an amplitude envelope to ensure the kinematics between the smooth and the rough surfaces remain constant. The denticles in the above-mentioned work (Oeffner and Lauder (2012); Wen et al. (2014)) are not scaled with local viscous scales so that they are within the drag-reducing regimes set out by Bechert et al. (2000a).

Figure 1.2 illustrates the diverse morphology of fish scales, highlighting that sharks are not the only aquatic swimmers with surface textures that may reduce drag. Research on grass carp, for instance, demonstrated that a bionic surface replicating their scales resulted in a drag reduction of about 3% in towing tank experiments, as reported by Wu et al. (2018). Additionally, studies on European sea bass scales have furthered

this understanding. A biomimetic surface, designed to echo the overlapping scales of sea bass, was found capable of generating parallel streamwise velocity streaks in the boundary layer. This mechanism is thought to play a role in delaying the transition to turbulence, a concept that aligns with earlier fundamental studies. Such streaky structures, induced by cylindrical roughness elements or vortex generator arrays, have been previously observed to delay transition and contribute to drag reduction (Fransson et al., 2006).

In a related study, Muthuramalingam et al. (2020) investigated biomimetic fish scales on a flat plate in a water channel. Their findings revealed a 55% delay in transition to turbulence and a theoretical 27% drag reduction. These results suggest that fish scales can stabilise the laminar boundary layer, thereby offering potential advantages for drag reduction in aquatic locomotion.

Therefore, the physical mechanisms responsible for the differences between rough and smooth surfaces remain unclear and illustrates the need for a systematic study to examine the interaction between surface textures and kinematics.

1.3 Research objectives and approach

This research aims to elucidate the contribution of surface textures to aquatic locomotion efficiency. While previous work has explored, either, the effects of kinematics on swimming performance, or the effects of surface texture on performance, less attention has been paid to the combination. Yet the morphological diversity of fish scales, as well as shark skin denticles, suggests an evolutionary advantage to these surface features.

The central objectives are: 1) Systematically investigate the first mode effects of the interaction between roughness and kinematics; 2) Investigate the stability of the boundary layer of a swimming foil at high *Re*. 3) Extend the study to realistic swimming shapes and scales, and map out the parameter space of potential control surfaces.

1.4 Thesis outline and contributions

Chapter 2 addresses the computational methods employed in this thesis. It introduces the equations solved, and the methodologies used for their solution. Additionally, extensive verification across various flow regimes and geometries is detailed.

Chapter 3 conducts a detailed examination of the impact of surface roughness on a self-propelled swimming plate. This chapter demonstrates that, as expected, roughness increases drag on the body, requiring a higher wave speed to maintain self-propelled

swimming. However, the interplay between roughness and kinematics extends beyond merely increasing drag, revealing more complex dynamics.

Chapter 4 implements resolvent analysis on a swimming foil at $Re = 100,000$. The chapter shows that the swimming motion significantly affects the boundary-layer stability. We also uncover specific spatial scales of the response modes that suggest an effective control mechanism might be found with the introduction of surface roughness.

Chapter 5 explores the effects of roughness in higher Reynolds numbers (*Re*) and smaller roughness scales. It is shown that incorporating body shape can enhance swimming efficiency, particularly when interacting with finely tuned surface roughness. This chapter also evaluates the actuated roughness hypothesis proposed by Lang et al. (2008). The findings suggest that at these scales, a fish-scale-like surface texture is most effective in improving swimming efficiency.

- We presented the representation of the viscous stress based on outer flow parameters at *Marine 2021*.
- The initial flow field analysis of the flat plate with generic roughness elements was presented at *UK Fluids 2021* chapter 3.
- The initial findings of chapter 4 were presented at *DisCoVor 2022*.
- chapter 4 has been presented at *APS 2022*.
- We have also submitted an abstract to *DisCoVor 2023* on the work relating to chapter 5.

1.4.1 Publications

The main projects in this thesis have been, or are under preparation for publication in the *Journal of Fluid Mechanics*.

1. chapter 3: Massey, J., Ganapathisubramani, B., & Weymouth, G. (2023). A systematic investigation into the effect of roughness on self-propelled swimming plates. *Journal of Fluid Mechanics*, 971, A39. doi:10.1017/jfm.2023.703
2. chapter 4: Massey, J., Ganapathisubramani, B., & Weymouth, G. (*in preparation*). Time varying roughness for sharkskin inspired control of a self-propelled swimming foil *Journal of Fluid Mechanics*.

1.4.2 Conference talks

1. Mar 2020 Machine learning the skin friction of a circular cylinder - CMNE
2. Sept 2021 Modal decomposition of flow over a rough plate - UK Fluids
3. Apr 2022 Surface roughness optimisation of an undulating plate - DisCoVor
4. Sept 2022 Secondary flows in rough swimming - APS DFD
5. Apr 2023 The interaction between roughness and swimming plates - DisCoVor
6. Jun 2023 Chaotic breakdown of secondary-flow amplification in rough swimmers - Delft Colloquia
7. Sept 2023 Resolvent analysis of a swimming foil - ReCoVor

Chapter 2

Numerical method

This chapter contains work published in the Journal of Fluid Mechanics (Massey et al., 2023).

This chapter outlines the numerical methodology underpinning this thesis, employing an in-house iLES code called Lotus. We adopt the QUICK treatment for convective terms and used an adaptive time-step meeting the CFL condition. Coupling with the body geometry is achieved via the BDIM, which has been validated for its second-order convergence in both time and space. We enforce no-slip and symmetry boundary conditions on the body. For verification and validation, we investigate the flow over a flat plate at an angle of attack $\alpha = 8^\circ$. While the mean lift is captured adequately, limitations arise due to the simulation time required to resolve low-frequency fluctuations. Comparison with experimental data reveals a 20% deviation for the rough plate, which we can attribute to the plate's thin geometry and thus trailing-edge 'singing' as well as limitations in computational resources. Further verification and validation exercises show that our method is stable and accurate. Specifically, we achieve convergence within acceptable error margins for both thrust coefficient and integral x-vorticity. Validation against experimental kinematics shows a deviation within 2%, and confirms our confidence in the numerical method.

2.1 Governing equations of incompressible fluid flow

One can describe fluid flow by a set of partial differential equations that express conservation of mass and momentum called the Navier-Stokes equations

$$\frac{\partial \vec{u}}{\partial t} + (\vec{u} \cdot \vec{\nabla})\vec{u} = -\frac{1}{\rho}\vec{\nabla} p + \nu \nabla^2 \vec{u} \tag{2.1}$$

where $\vec{u}(\vec{x},t) = (u,v,w)$ is the velocity vector, $p(\vec{x},t)$ is the pressure field, t is the time, $\vec{x} = (x,y,z)$ is the spatial vector, ρ is the density, and ν is the kinematic viscosity. From left to right of equation 2.1 we have four distinct terms; the change of velocity in time, the convection term, the pressure term, and the diffusion term. To ensure incompressibility, we also use the continuity equation to constrain the solution, we define this as

$$\vec{\nabla} \cdot \vec{u} = 0. \tag{2.2}$$

The pressure is still unknown, so we define an additional relationship to couple the velocity and pressure by taking the divergence of equation 2.1

$$\vec{\nabla} \cdot \left(\frac{\partial \vec{u}}{\partial t} + (\vec{u} \cdot \vec{\nabla})\vec{u} + \frac{1}{\rho}\vec{\nabla} p - \nu \nabla^2 \vec{u} \right) = 0 \tag{2.3}$$

which we can rearrange to get the pressure-Poisson equation

$$\vec{\nabla}^2 p = -\rho \vec{\nabla} \cdot \left(\frac{\partial \vec{u}}{\partial t} + (\vec{u} \cdot \vec{\nabla})\vec{u} - \nu \nabla^2 \vec{u} \right) \tag{2.4}$$

The system of equations is also bounded by the no-slip condition that defines the velocity on the surface of a body as $\vec{u_b} = \vec{v}(\vec{x},t)$ where $\vec{v}(\vec{x},t)$ is the velocity of the body. Finally, the Reynolds number (Re), which we have made reference to in chapter 1, describes the balance between convective and viscous forces and is defined as

$$Re = \frac{UL}{\nu} \tag{2.5}$$

where U, L are the characteristic velocity and length of the system and the kinematic viscosity $\nu = \frac{\mu}{\rho}$ where μ is the dynamic viscosity of the fluid.

2.2 Numerical methods

2.2.1 Spatial Discretisation

The three main governing equations (2.1, 2.1, 2.1) are discretised onto a rectilinear grid using a finite-volume method. The pressure field is stored on the cell centre, and the velocity on the cell face; 2.1 shows an illustration of the discretisation of the governing equations.

FIGURE 2.1: Illustration of a rectilinear grid. The volume for the pressure is blue and the u velocity component is green.

We calculate the gradients in equation 2.1 using the conservative finite-volume method on the cell face fluxes. To approximate the convection term, we use the QUICK scheme (Leonard (1979)). The quick scheme uses one upstream and two downstream points to fit a quadratic function that interpolates the interest quantity at the cell face.

2.2.2 Temporal discretisation

We use Chorin's projection method (Chorin, 1968) to step forward in time our governing equations. Briefly, Chorin's projection method allows us to decouple the velocity and pressure fields by relaxing the divergence-free condition to give an intermediate velocity field. Mathematically we split equation 2.1 into two parts

$$\frac{\vec{u}^{\star} - \vec{u}^{n}}{\delta t} = \nu \nabla^2 \vec{u}^{n} - (\vec{u}^{n} \cdot \vec{\nabla}) \vec{u}^{n}, \tag{2.6a}$$

$$\frac{\vec{u}^{n+1} - \vec{u}^{\star}}{\delta t} = -\vec{\nabla} p^{n+1} \tag{2.6b}$$

where superscript n refers to the time step level and superscript $\star$ refers to the intermediate velocity field. Splitting equation 2.1 into equation 2.6a and equation 2.6b allows us to compute a divergence free velocity field at $\vec{u}^{n+1}$ by enforcing the continuity equation equation 2.1 on p^{n+1} instead of computing $\vec{u}^{n+1}$ from p^{n} which would not be divergence free at time $n+1$.

We use a predictor-corrector algorithm to calculate $\vec{u}^{n+1}$ with $\vec{\phi}(\vec{u}) = (\vec{u} \cdot \vec{\nabla})\vec{u} - \nu \nabla^2 \vec{u}$ to simplify the notation and $\langle\rangle$ brackets to denote a field that might not be divergence free. The algorithm steps for the predictor corrector steps are

Predictor step :

$$\text{1.} \quad \langle \vec{u}^{\star} \rangle = \vec{u}^{n} + \vec{\phi}^{n} \delta t, \tag{2.7}$$

$$\text{2.} \quad \delta t \, \nabla^2 p^{\star} = \nabla \cdot \langle \vec{u}^{\star} \rangle, \tag{2.8}$$

$$\text{3.} \quad \vec{u}^{\star} = \langle \vec{u}^{\star} \rangle - \delta t \nabla p^{\star}. \tag{2.9}$$

Corrector step :

$$\text{4.} \quad \langle \vec{u}^{n+1} \rangle = \vec{u}^{n} + \frac{1}{2}(\vec{\phi}^{n} + \vec{\phi}^{\star}) \delta t, \tag{2.10}$$

$$\text{5.} \quad \delta t \, \nabla^2 p^{n+1} = \nabla \cdot \langle \vec{u}^{n+1} \rangle, \tag{2.11}$$

$$\text{6.} \quad \vec{u}^{n+1} = \vec{u}^{\star} - \delta t \nabla p^{n+1}. \tag{2.12}$$

First, we use an explicit Euler scheme to *predict* the solution forward one-time step. Next, we determine the pressure correction required to ensure the velocity is divergence-free. Step 4 uses the trapezoid rule to correct the solution to time $n+1$. Finally, we check the divergence-free condition and correct the solution accordingly. The predictor-corrector algorithm can be shown to be second-order accurate and has the stability of the explicit Euler method Ferziger et al. (2019).

For the time step (δt) we use the local Courant ($u \, \delta t / \delta x$) and Péclet number ($\nu \, \delta t / (\delta x)^2$). The combination of these limits δt such that $\delta t < \left[\frac{2\nu}{\min[(\delta x)^2]} + \max\left(\frac{u}{\delta x} \right) \right]^{-1}$.

2.2.3 Solid boundaries

To impose the no-slip condition on the body we use an Immersed Boundary (IB) method. IB methods were first developed by the mathematician Charles Peskin Peskin (1972) for studying flow patterns around heart valves. The main advantage of an IB method is that they don't require a body conforming grid, which removes the computational cost of grid generation. For a static, simple geometry grid generation isn't a problem, but for complex geometries or moving boundaries generating a grid at every time step becomes prohibitively expensive.

We use the Boundary Data Immersion Method (BDIM) from Weymouth and Yue (2011); Maertens and Weymouth (2015). The BDIM convolves the body ($\mathcal{B}$) governing equation defined as

$$\mathcal{B} = \vec{v}(\vec{x}, t) \tag{2.13}$$

with the fluid governing equations ($\mathcal{F}$) defined by the incompressible Navier-Stokes

FIGURE 2.2: An illustration of the smoothing between the fluid and the body domain for a circular cylinder using a smoothing kernel.

(equation 2.1). For equation 2.13, $\vec{V}(\vec{x},t)$ is the body velocity field. The equations are then convolved though a nascent-delta kernel which defines

$$\begin{cases} \vec{u} = \mathcal{B}(\vec{v},t), & \text{for} \vec{x} \in \Omega_{\mathcal{B}} \\ \vec{u} = \mathcal{F}(\vec{u},t), & \text{for} \vec{x} \in \Omega_{\mathcal{F}} \end{cases} \tag{2.14}$$

where the body domain is $(\omega_{\mathcal{B}})$ and the fluid domain is $(\omega_{\mathcal{F}})$. The equations are convolved into a single meta-equation $(\mathcal{M})$ which we define as

$$\vec{u}_{\epsilon}(\vec{x}) = \mu_0^{\epsilon}\mathcal{F} + (1-\mu_0^{\epsilon})\mathcal{B} + \mu_1^{\epsilon}\frac{\partial}{\partial n}(\mathcal{F}-\mathcal{B}) \tag{2.15}$$

The interface between the fluid and body governing equation is smoothed to immerse the body onto the background Cartesian grid without creating large derivatives. We use a convolution kernel $(\mathcal{K}_{\epsilon})$ to smooth the transition from the fluid domain $(\omega_{\mathcal{F}})$ to $(\omega_{\mathcal{B}})$, which is illustrated in Figure 2.2.

The first and second moments of a cosine kernel, μ_0, μ_1, have radial support ϵ and are defined as

$$\mu_0^{\epsilon}(d) = \begin{cases} \frac{1}{2}\left[1 + \frac{d}{\epsilon} + \frac{1}{\pi}\sin\left(\frac{d}{\epsilon}\pi\right)\right] & \text{for } |d| < \epsilon \\ 0 & \text{for} d \leq -\epsilon \\ 1 & \text{for} d \geq \epsilon \end{cases} \tag{2.16a}$$

$$\mu_1^{\epsilon}(d) = \begin{cases} \epsilon\left[\frac{1}{4} - \left(\frac{d}{2\epsilon}\right)^2 - \frac{1}{2\pi}\left(\frac{d}{\epsilon}\sin\left(\frac{d}{\epsilon}\pi\right) + \frac{1}{\pi}\left(1+\cos\left(\frac{d}{\epsilon}\pi\right)\right)\right)\right] & \text{for } |d| < \epsilon \\ 0 & \text{for } |d| \geq \epsilon \end{cases} \tag{2.16b}$$

where $d = |x-y|$ is the euclidean distance from the kernel. For a more detailed explanation refer to Weymouth and Yue (2011); Maertens and Weymouth (2015).

The BDIM has been tested on multiple applications and validated for various use cases, most recently Zurman-Nasution et al. (2020); Lauber et al. (2022). We will also validate our simulations against experimental data to show the validity of the solution method.

2.2.4 Pressure solver

We use a multigrid method for the pressure correction step in the predictor-corrector algorithm equation 2.8 and equation 2.11. We can write the discrete Poisson equation as a linear system of equations:

$$Mp = b, \tag{2.17}$$

where b is the intermediate velocity field divergence, and M contains the discretised Laplacian operator. The multigrid method is an iterative process updating an estimated solution p^n to a new solution p^{n+1} by minimising the residual defined as

$$r^n = Mp - b, \tag{2.18}$$

where r^n is the residual at time n. We then define the error as

$$\eta^n = p - p^n, \tag{2.19}$$

where η^n is the error at time n. We can then write the linear system of equations as

$$M\eta^n = r^n. \tag{2.20}$$

Minimising r^n uses an increasingly coarse grid to increase the speed of the iterations. We use a single Jacobi iteration before downsampling and increasing the grid coarseness. The downsampling is done via

$$\eta_I = \frac{1}{(\eta x)^2}(\eta^n_{i-1} - 2\eta^n_i + \eta^n_{i+1}) = r^n_i, \tag{2.21}$$

where the subscript i denotes the fine grid cell index and I the coarse grid cell index. Once the residual has been downsampled to an arbitrary coarse grid, it is upsampled back to the original fine grid. After each sampling step, we employ a conjugate gradient method to update the solution. This upsampling and downsampling operation is known as a V-cycle. V-Cycles are repeated until the pressure-Poisson equation has converged to a divergence within a limit of 10^{-5}.

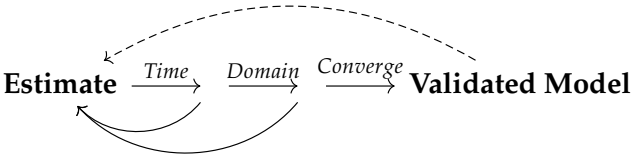

FIGURE 2.3: Schematic of the iterative verification process for numerical simulations

2.2.5 Verification

The verification of computational fluid dynamic (CFD) simulations is an iterative process involving some key steps (figure 2.3). Initially, an estimate of the time needed for statistically converged results is determined. Subsequently, domain sensitivity is assessed to ensure that flow structures can develop without constraints and that altering the domain size does not significantly influence the mean statistics. Grid refinement is then applied to enhance computational efficiency without compromising accuracy. The cycle culminates in a grid convergence study to validate the numerical model. This iterative process continues until the model meets predefined accuracy criteria.

2.3 Flow over a flat plate

In this section, we will show that our numerical method can accurately simulate the flow over a flat plate at $Re = 12,000$ and $\alpha = 8°$. We will first show that the numerical method is stable and converges to a solution. We will then show that the forces are invariant to the domain size and grid resolution. Finally, we make reference to experimental data of a flat plate at $\alpha = 8°$ and $Re = 12,000$ (Vilumbrales-Garcia et al., 2024).

2.3.1 Geometry

We set the geometry by using four planes to define a rectangular plate within our computational domain. Using its signed distance function (SDF), we describe the plane and create a geometric set based on the union of defined normal directions. The set of four planes then makes up the rectangular shape of our flat plate where the flow velocity $\vec{u} = 0$. The roughness elements are added to this set using the SDF of a sphere and a coordinate transform based on a modulo mapping defines the spacing of the roughness elements. The modulo mapping reduces the computational load which is important as computing the body properties of on all the individual roughness elements is expensive. Instead, we update one sphere and transform the properties. We use BDIM to impose the boundary conditions and compute the flow quantities.

We characterise the roughness based using three parameters normalised by the body length, L (figure 2.4). The radius of the bump is defined by r, h defines the bump

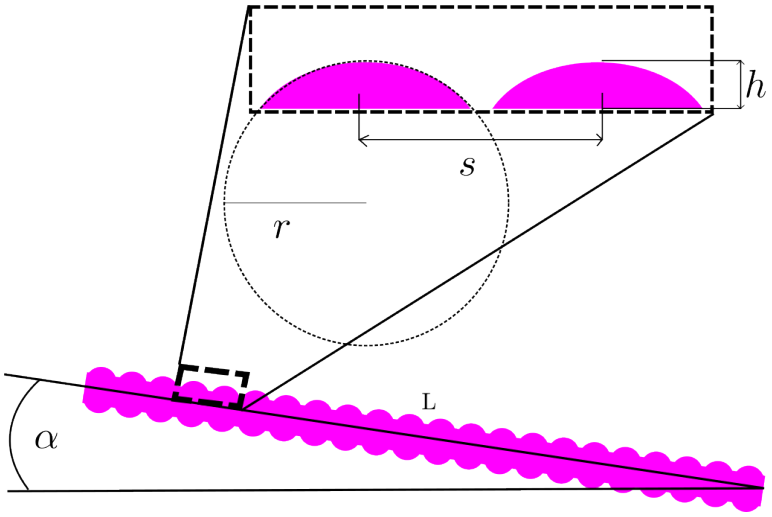

FIGURE 2.4: The parameterisation of the flat plate roughness.

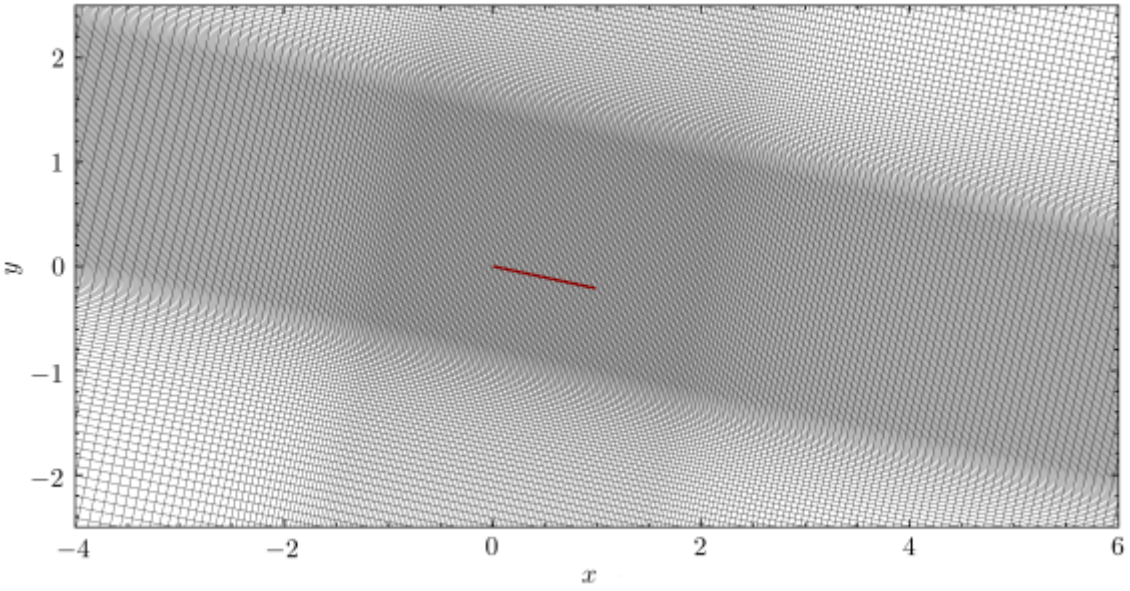

FIGURE 2.5: An example of the computational grid, rotated so that the inflow conditions are equivalent to $U = (1, 0, 0)$. There is a central region where the grid is uniform and rectilinear.

protrusion, and sb defines the spacing. For consistency with experimental results we use $sb/2r = 1$ for a case we refer to as the 70% coverage case. We match the values of the roughness parameters to this experimental counterpart so $sb = 58/960$, $h = 3/320$, and $r = 7/320$.

2.3.2 Grid

We use a rectilinear grid with a uniform region around the body and near wake (figure 2.5), the grid cells are then stretched to the domain boundaries via hyperbolic stretching,

being careful not to distort the flow. The grid is aligned with the body, and the inflow is projected in a direction $\vec{U}(sin(\alpha), cos(\alpha), 0)$, where $\alpha = 8^\circ$ is the angle of attack of the plate. We have Neumann boundary conditions in the x, y directions and symmetry conditions to match the finite domain of the experiments. Continuing the normalisation of all length parameters by the body length, L, the computational domain extends over $x \in [-5, 9]$, $y \in [-3, 3]$, and $z \in [0, 3]$. The uniform region around the body is bound by $x \in [-1, 2]$, $y \in [-0.8, 1]$, and $z \in [0, 3]$ and the domain resolution is specified as $\vec{N} = (768, 768, 384)$, where $\vec{N} = (n_x, n_y, n_z)$. The grid spacings in the uniform region are $\Delta x = 1/96$, $\Delta y = 1/256$, and $\Delta_z = 1/128$; more generally, they can be denoted by the ratio $8 : 3 : 6$.

2.3.3 Time convergence

To assess the convergence we look at the near-wall behaviour by looking at the forces, defined by

$$C_T = \frac{\oint \vec{f}_x ds}{0.5S}, \quad C_L = \frac{\oint \vec{f}_y ds}{0.5S}, \quad C_P = \frac{\oint \vec{f} \cdot \vec{v} ds}{0.5S} \tag{2.22}$$

where $\vec{f} = -p \cdot \hat{n}$ is the normal pressure stress on the body, $\vec{v}$ is the body velocity, and S is the planform area of the plate. Specifically, we use the pressure-based lift as the viscous force is less than 1% of the total force contribution and requires an unworkable grid resolution to fully resolve.

We run a long simulation was run for $t_{total} = 500$ using a down sampled resolution of $\Delta x = 1/64$, $\Delta y = 1/128$, and $\delta_z = 1/96$ so $\vec{N} = (512, 512, 256)$. We can see the time series for the lift pressure in figure 2.6a that it is not immediately clear what the longest repeating timescale is. Subsequently, we instead look at the convergence in frequency spectra by using the long time series simulation and calculating the power spectra using Welch's method with windows of $25t$ and a 50% overlap, we then systematically truncate the spectra until the dominant peaks are captured.

The series truncated at $t_{total} = 125$ does a good job capturing the dominant peaks of the long time series data (figure 2.6b); any further truncated and the noise becomes too much to delineate coherent peaks (see the pink line for $t_{total} = 75$). Figure 2.6b shows that the is large amplitude instability at frequencies below 8 convection cycles, this is likely due to the stochastic nature of separated flows. Further, the spectra exhibits peaks at $f = 0.2$ and $f = 1$ corresponding to different shedding frequencies.

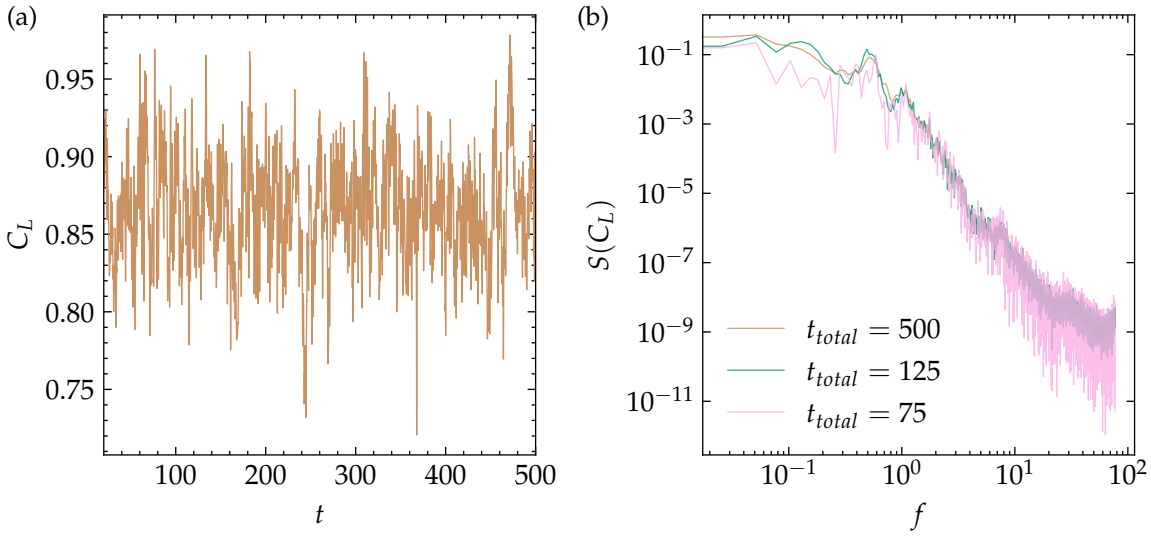

FIGURE 2.6: (a), The time series of the pressure-based lift coefficient for a simulation time of $t_{total} = 500$ convection cycles. (b), The power spectra of the time series with lines denoting a full and truncated time series.

Domain	$\vec{N}$	Mean error	RMS error
$([-3.5, 6], [-2.5, 2.5], [0, 3])$	$(1.438, 1.333, 3.000)$	2.3%	5.8%
$([-5, 9], [-3, 3], [0, 3])$	$(2.000, 1.500, 3.000)$	1.1%	0.4%
$([-8, 16], [-6, 6], [0, 3])$	$(3.250, 2.500, 3.000)$	-	-

TABLE 2.1: Domain size, $\vec{N}$, mean, and RMS error based on the large domain.

2.3.4 Domain test

The size of the domain needs to be sufficiently large so as not to introduce boundary effects that could distort the results or compromise the accuracy of simulations. A too-small domain may fail to capture important physical phenomena or could lead to artificial numerical constraints. To large a domain will add unnecessary bloat to the simulation process. To test the sufficiency of the domain—and continuing to scale all length scales by L—we fix the size of the z direction to 3 to match the domain of the experiments. For the x, y domain, we test the mean and RMS error and the spectra. We use the same downsampled uniform region grid spacing as section 2.3.3, and to avoid distorting the flow, we increase the total number of points in the domain as we increase the domain size.

The results in table 2.1 show that the domain does not significantly affect the results. There is not much computational benefit to using the smallest domain despite being in an acceptable error range.

$\frac{\Delta z}{\Delta x}$	Mean error
2	0.7%
1.5	1.1%
1	0.6%
0.75	0.1%
0.5	-

TABLE 2.2: The error from z grid spacing in $\overline{C_L}$

$\frac{\Delta y}{\Delta x}$	Mean error
1	42.0%
0.75	25.7%
0.5	1.6%
0.375	0.3%
0.25	-

TABLE 2.3: The error from y grid spacing in $\overline{C_L}$

2.3.5 Grid Refinement

The grid is refined in the y-direction to increase the resolution of the boundary layer while minimising computational costs. Grid refinement in y is particularly crucial, as the fluctuation scales in this direction are generally much smaller than those in x and z.

We conducted tests with varying grid spacing, while keeping the grid stretching in the outer domain constant. Constraints on the maximum grid spacing are applied as follows:

$$\Delta x_{\max} \leq 2.5\Delta x, \quad \Delta y_{\max} \leq 8\Delta x \tag{2.23}$$

We also limited the expansion ratio to a maximum value of 6%, which is within the bounds tested in our domain study.

The error due to Δz grid spacing, as shown in table 2.2, is relatively insensitive to changes. We selected $\Delta z = 0.75\Delta x$ due to computational resource constraints.

Grid refinement in the y-direction provides significant gains in computational efficiency. Table 2.3 shows that full convergence is achieved when $\Delta y = 0.375\Delta x$.

$\frac{1}{\Delta x}$	Mean error
48	1.6%
64	1.7%
96	1.6%
128	-

TABLE 2.4: The error in $\overline{C_L}$ from the smooth plate grid convergence study.

$\frac{1}{\Delta x}$	Mean error
48	-37.7%
64	-23.0%
96	-7.1%
128	-

TABLE 2.5: The error in $\overline{C_L}$ from the 70% rough plate grid convergence study.

Coverage	$\overline{C_{L,\text{simulation}}}$	$\overline{C_{L,\text{experiment}}}$
0%	0.848	0.799
70%	0.632	0.761

TABLE 2.6: Comparison of simulation and experimental results for the smooth (0% coverage) and rough (70% coverage) plate.

2.3.6 Resolution Convergence

We complete our verification phase by rigorously establishing grid convergence within acceptable error margins. This confirms a reliable numerical representation of the flat-plate physics. Up to this point, we have focused on the smooth plate, which serves as a simpler foundation and influences global metrics crucial for the setup. We now incorporate the rough plate to evaluate its effects on the simulation. Our primary performance metric remains the time-averaged lift coefficient $\overline{C_L}$.

For the 70% roughness configuration, the results stabilise at $\Delta x = 1/96$, enhancing our confidence in the simulation's accuracy. This rough plate configuration shows better convergence compared to the smooth counterpart. The improvement is attributed to the geometric resolution of the roughness elements significantly affecting $\overline{C_L}$.

2.3.7 Validation

To validate our numerical results, we compare the $\overline{C_L}$ against corresponding experimental data (Vilumbrales-Garcia et al., 2024).

The simulation results show relatively good agreement with experimental data (table 2.6). For the smooth plate, the simulated $\overline{C_L}$ is within 6% of the experimental value. For the rough plate, the discrepancy is slightly larger, within approximately 20%. The differences can be attributed to factors surrounding the experimental and the complexities involved in simulating rough surfaces. These results show the accuracy of our computational model is limited, and further work is needed to confirm their suitability for further studies on the effects of roughness on aquatic locomotion.

2.4 Flat plate with general—undulatory—kinematics

In this section, we extend our verification and validation to a flat plate at $Re = 12,000$ with general—undulatory—kinematics. Employing the base model from section 2.3, we vary the roughness definition to one suited to a systematic investigation. We first establish the stability and convergence of our numerical method for both smooth and rough plates. Subsequently, we demonstrate the forces' invariance to domain size and grid resolution. Lastly, we compare our model with an experiment of a flexible plate with motion.

2.4.1 Geometry

Continuing to normalise all length scales by the plate length L, we use a flat plate with a thickness 0.03 as the base model, which closely resembles the experiment of Wen et al. (2014). For the roughness, we use a sinusoidal roughness, similar to Napoli et al. (2008); Chan et al. (2015); Ma et al. (2020); Ganju et al. (2022), that allows us to vary the roughness topology systematically. Figure 2.7a illustrates the parameters affecting the roughness topology. The topography is defined as

$$y(x,z) = \begin{cases} h \sin\left(\frac{2\pi x}{\lambda}\right) \cos\left(\frac{2\pi z}{\lambda}\right), & \text{for } y \geq 0.015 - h \\ h \sin\left(\frac{2\pi x}{\lambda} - \pi\right) \cos\left(\frac{2\pi z}{\lambda}\right), & \text{for } y \leq -0.015 + h \end{cases} \tag{2.24}$$

where y is the direction normal to the plate and x, z are the tangential direction, and λ is the roughness wavelength.

2.4.2 Kinematics

Continuing to use the swimming speed U to scale velocity and L/U to scale time, we define the excursion of the body from the centre line as

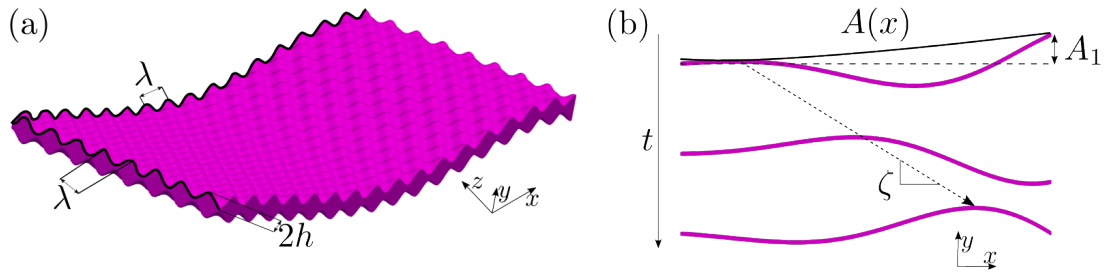

FIGURE 2.7: (a) The geometry used which has two defining parameters: λ, the wavelength of the roughness, and h, the roughness amplitude. (b) A visual representation of the parameters that define the plate motion.

$$y(x) = A(x)\sin\left(2\pi\left[ft - x/\zeta\right]\right) \tag{2.25}$$

where f is the frequency, ζ is the phase speed of the travelling wave, and $A(x)$ is the amplitude envelope, all of which are illustrated in figure 2.7b. The Strouhal number is set to peak propulsive value $St = 0.3$ which determines the scaled frequency as $f = St/2A_1$, where $A_1 = A(x = 1)$ is the trailing edge amplitude and defines the wake width of the system. We modify the recent result from Di Santo et al. (2021) for the envelope

$$A(x) = \frac{A_1(a_2x^2 + a_1x + a_0)}{\sum_{i=0}^{2} a_i} \tag{2.26}$$

using $a_{0,1,2} = (0.05, 0.13, 0.28)$ and $A_1 = 0.1$, as found to be optimal in Saadat et al. (2017). The modification changes a_1 from -0.13 (Di Santo et al., 2021) to 0.13 reducing the amplitude of the leading edge, enabling self-propelled swimming over a wider range of λ.

2.4.3 Grid and domain

Figure 2.8 details the grid and domain set-up. We show the domain invariance of the solution by comparing the cycle average time series of C_T. We compare the working domain (Domain 1) of size $(18, 20)$ and resolution $(1536, 1536)$, to a much larger domain (Domain 2), size $(9, 4)$ and resolution $(3072, 3072)$ (figure 2.9a). Figure 2.9b shows the cycle average time series of C_T for the three Re where $\varphi = 2\pi f \bmod t$. For all three ($Re = 6, 12$, and 24×10^3), C_T is plotted for Domain 1 (solid line), and Domain 2 (dotted line). C_T for both domains collapses, and so the solution is domain invariant. We use a rectilinear-grid over the domain $x \in [-2, 7]$, $y \in [-2, 2]$ and vary the spanwise-direction

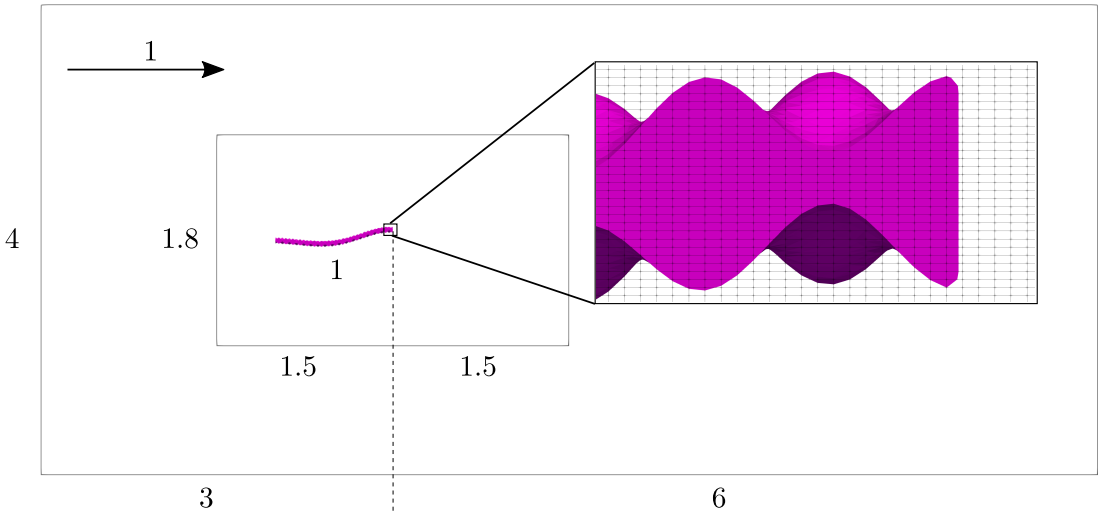

FIGURE 2.8: Schematic for the domain and grid. The inner box shows the region where the grid is uniformly rectilinear; from there, the grid stretches toward the domain extent. This is a representative grid for the xy plane on the geometry where $\lambda = 1/16$. We use a periodic boundary condition and $\max(6\lambda, 0.25)$ to define the repeating spanwise domain size. The insert indicates the grid around the tail of the plate showing that, for $\lambda = 1/16$, we have 16 cells resolving the roughness wavelength, and 5 cells resolving the amplitude of the surface.

so that $z \in [0, \max(6\lambda, 0.25)]$ (figure 2.8). For the area that contains the body motion and the immediate wake, we use a uniform grid and then implement hyperbolic stretching of the grid cells away from this area (figure 2.8). The grid is refined in y such that Δy is half Δx and Δz (figure 2.8 insert). This gives us a total number of grid points of ranging $[67.1, 403] \times 10^6$; which are distributed as $\vec{N} = (1536, 1536, [64, 384])$. Careful consideration of the aspect ratio of the maximum stretched cell meant that it did not exceed five times that of the uniform region to avoid distorting the flow in the wake.

2.4.4 Resolution convergence

We tested resolutions of increasing powers of two for two surfaces where $\lambda = 1/16, 1/52$ (figure 2.10). For figure 2.10a we measured the error against the value at the highest resolution, which contained $2.4 \times 10^9 9$ grid cells. The pressure-based thrust $\overline{C_T}$ oscillates around a zero mean, and so we measure the error in $\overline{C_T^2}$. We converge to below 4% error for both surfaces. Our working resolution is at the lowest limit of $\Delta x = 0.004$ and figure 2.10b shows that the time history of C_T also converges within this.

Figure 2.11 shows the convergence of the integral quantity of the x-vorticity magnitude for the two surfaces where $\lambda = 1/16, 1/52$. We choose the surface where $\lambda = 1/16$ because it is around this value that significant increases in enstrophy were found. We also test the surface where $\lambda = 1/52$ because this represents the lowest limit of our surface resolution; for the proposed working resolution of $\Delta x = 0.004$, 5 grid cells resolve the surface wavelength in the x and in the z direction.

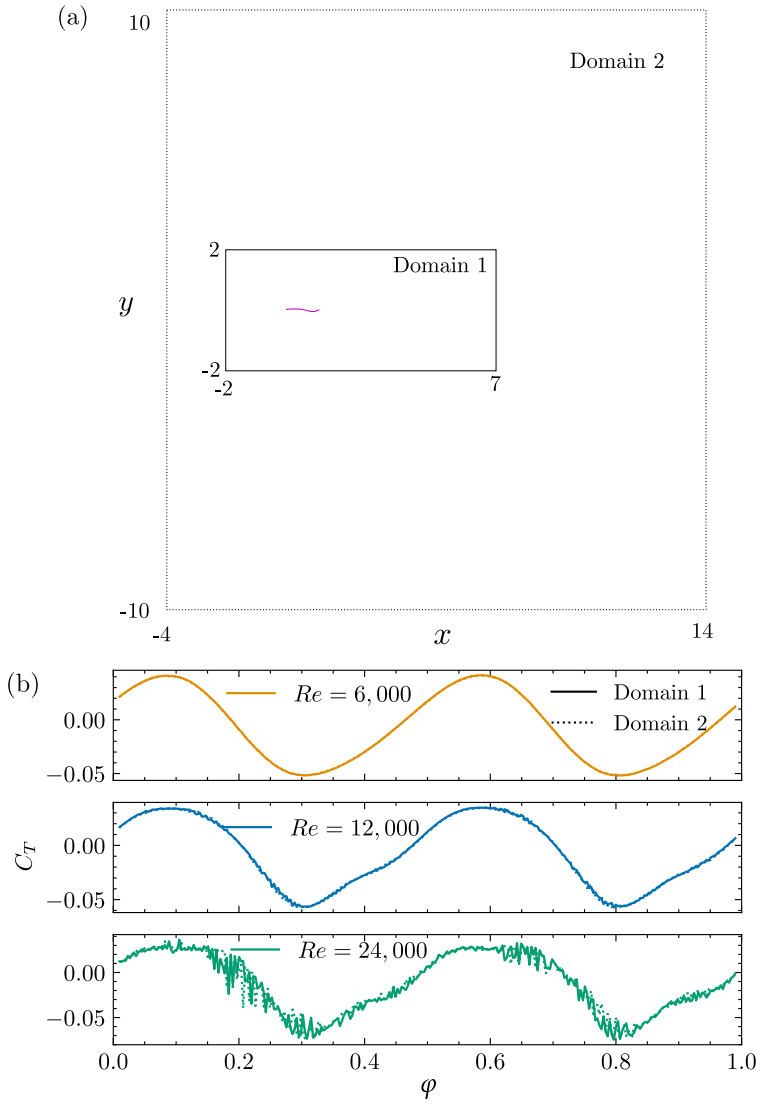

FIGURE 2.9: The domain invariance of C_T. (a) The relative size of the two-dimensional domains. The dotted line marks the extent of Domain 2 where $(x, y) \in ([-4, 14], [-10, 10])$, and the solid line marks Domain 1, where $(x, y) \in ([-2, 7], [-2, 2])$. (b) The thrust coefficient for $\zeta = 1.06$ and $St = 0.3$, the solid line for Domain 1 and the dotted line of Domain 2 are plotted on top of each other.

Furthermore, we measure $\int |\omega_x| dV$ because it is zero for the two-dimensional, smooth cases and, therefore, allows us to quantify the grid-resolution-independence of the topographic contribution to the flow. Again, we converged to within a reasonable limit at our working resolution of $\Delta x = 0.004$.

2.4.5 Experimental validation

First, we show that the method implemented in this study, set out in section 2.4.2, converges to grid-independent solution. We perform simulations at $St = 0.3$, $\zeta = 1.06$ and $Re = 6, 12$, and 24×10^3 with increasing resolution. In figure 2.12, we plot C_T (phase

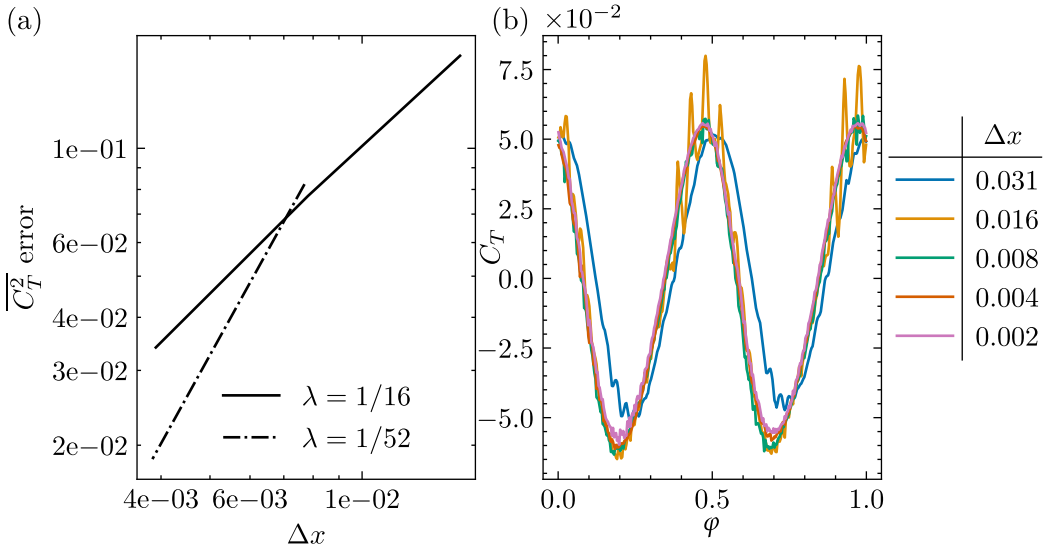

FIGURE 2.10: This figure shows the resolution convergence for the rough, self-propelled swimming plate. (a) The error convergence of $\overline{C_T^2}$. (b) Phase averaged cycle where $\lambda = 1/16$.

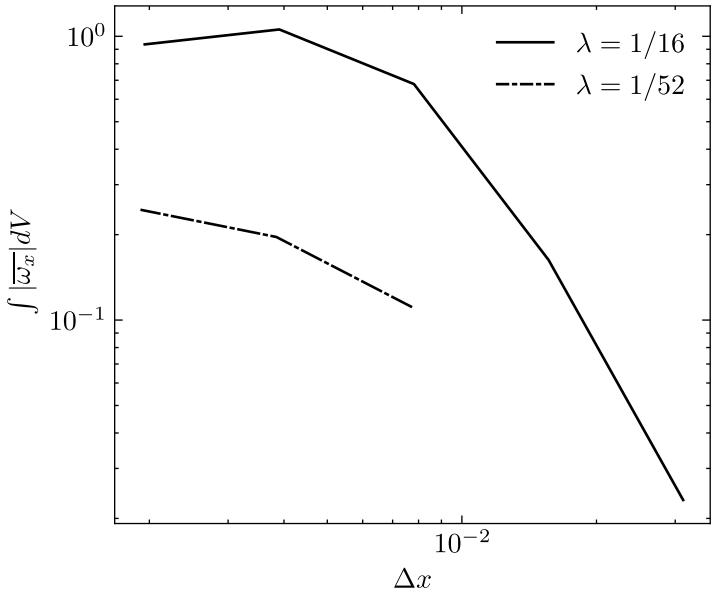

FIGURE 2.11: The convergence of $\int |\overline{\omega_x}| dV$ with simulation fidelity.

averaged over four cycles) and show that the resolution minimally affects the time series to the point where different resolutions are barely distinguishable from each other.

Next, we validate our model by showing consistency with an experimental study (Lucas et al., 2015). We make minor alterations to our model to match the kinematic trajectory, *St* and *Re* of a swimming plate. In Lucas et al. (2015), they test four different plate stiffnesses and assess the swimming performance. Of these four plates one (plate '1_3') had an increasing amplitude envelope and a relatively constant wave speed; which ensures the changes we need to match their conditions are minimal. Although Lucas et al. (2015) test a range of different *St*s and *Re*; for the plate we are matching, they only

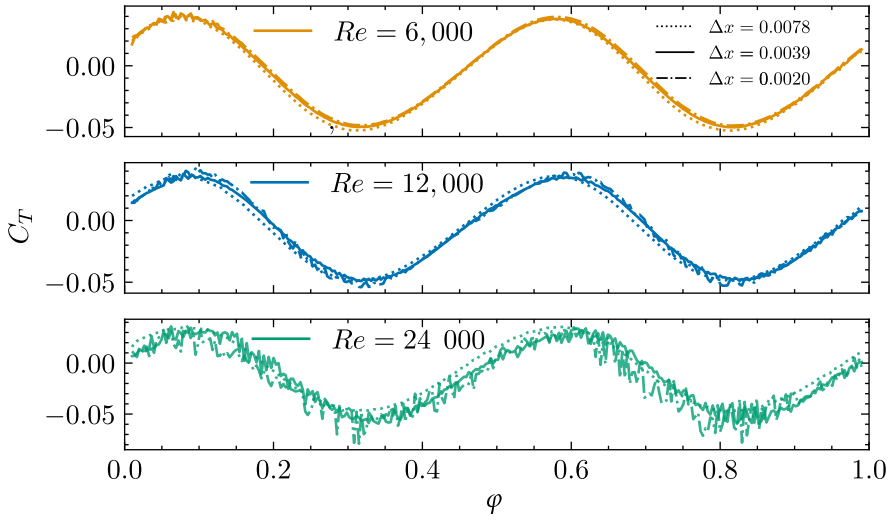

FIGURE 2.12: The numerical convergence for the kinematic trajectory defined by equation 2.26 for $\zeta = 1.06$ and $St = 0.3$.

provide the kinematic trajectory for $Re = 77,000$ and $St = 0.31$. Because of the sensitivity of the kinematic mode shape of a flexible plate to different excitation conditions (Quinn et al., 2014), we can only consider the data point where $Re = 77,000$ and $St = 0.31$.

Figure 2.13 shows a comparison of the raw and matched kinematic trajectories. We match the trajectory by minimising $||y(x,t) - \langle y(x,t)\rangle||_2^2$ where $\langle y(x,t)\rangle$ is the model for the kinematics. We consider the amplitude envelope, $A(x)$ and the wave speed, ζ separately and arrive at the functional form

$$\langle y(x,t)\rangle = a_i x^i \sin\left(2\pi(x/\zeta - ft)\right) \tag{2.27}$$

where $i_{0,1,2} = [0.072, 0.1685, -0.0701]$, and $\zeta = 2.15$. Furthermore, we measured the error in $\langle y(x,t)\rangle$ using

$$\sigma(y(x,t) - \langle y(x,t)\rangle)/\sigma(y(x,t)) = 0.076 \tag{2.28}$$

where $\sigma(x) = \sqrt{\overline{(x-\overline{x})^2}}$ is the operator to compute the standard deviation. The raw data in Lucas et al. (2015) does not perfectly match the idealised model of a swimmer, with slight asymmetry (figure 2.13) introducing the reported error.

We have kept the domain size, grid-refinement and time-step constant to our working model and only altered the kinematic trajectory, St and Re. This allows us to assess the accuracy of the computational setup compared to Lucas et al. (2015). As we increase the resolution, $\overline{C_T}$ converges to within 1.7% of the reported experimental value, table 2.7. This gives us confidence that the computational setup is accurate and that the kinematics

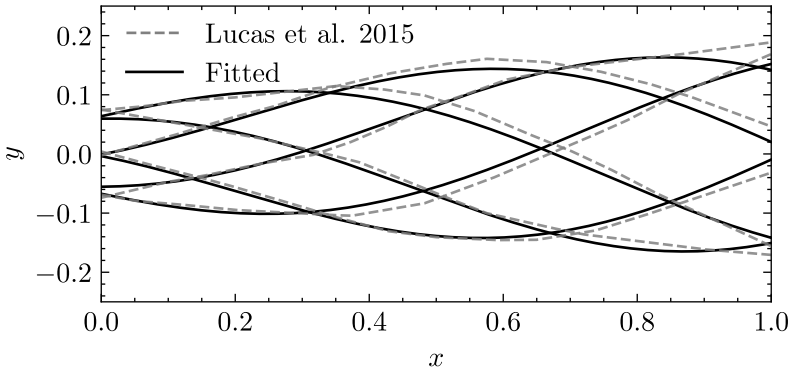

FIGURE 2.13: The difference between the kinematic trajectories reported in Lucas et al. (2015) and the fitted functional form (equation 2.4.5).

Δx	$\overline{C_T}$	error
0.00391	0.183	0.131
0.00195	0.167	0.029
0.00098	0.165	0.017

TABLE 2.7: The convergence of $\overline{C_T}$ to experimental results of Lucas et al. (2015).

are correctly implemented. For more validation of BDIM for swimming simulations, the reader is referred to Maertens et al. (2017) who performs a like-for-like comparison of undulatory locomotion with Dong and Lu (2007).

2.5 Conclusions

This chapter outlined the numerical methodology underpinning this thesis. We used Lotus, an in-house developed finite-volume implicit large eddy simulation (iLES) code. The implicit modelling of iLES derived from a flux-limited, QUICK (quadratic upstream interpolation for convective kinematics), treatment of the convective terms (Hendrickson et al., 2019). We used an adaptive time-step based on the Courant Friedrichs Lewy condition that has been shown to converge with $O(2)$ (Lauber et al., 2022). The body geometry was coupled to these flow equations using the Boundary Data Immersion Method (BDIM) formulated in Weymouth and Yue (2011), further developed for higher Reynolds numbers in Maertens and Weymouth (2015), and thin geometries in Lauber et al. (2022). BDIM enforced the boundary condition on the body by convolving together the fluid and body governing equations on a Cartesian background grid.

We examined the flow over a flat plate with $\alpha = 8°$. The mean lift was captured well, however the long time period required to resolve the low frequency fluctuations limited the reach of the convergence study to coarse meshes. Further, we compared $\overline{C_L}$ to experiments and while the smooth plate results aligned well with experimental data, the

rough plate deviated by 20%. These experiments posed their own difficulties requiring more work before publication. The complications surrounded the rigidity of the plate with such a thin geometry. This resulted in a 'singing' at the trailing edge of the plate warranting further investigation. The comparison to experiments was useful in that both should significant reductions in $\overline{C_L}$ with the addition of roughness, however more work on the validation of the numerical method for our specific case was needed.

As a result, we undertook further verification and validation of the numerical method by simulating a flat plate with general kinematics, for both rough, and smooth plates. We showed that the method converged to acceptable error range for the thrust coefficient and the integral of the x-vorticity, and that the results are domain invariant. We then validated the kinematics by matching the kinematic trajectory to experimental results and showed the thrust coefficient converge to within 2%. The results were in good agreement with the experiment, and we have confidence in the numerical method.

Chapter 3

A systematic investigation into the effect of roughness on self-propelled swimming plates

This chapter contains work published in the Journal of Fluid Mechanics (Massey et al., 2023).

This study examines the effects of surface topography on the flow and performance of a Self-Propelled Swimming (SPS) body. We consider a thin flat plate with an egg-carton roughness texture undergoing prescribed undulatory swimming kinematics at a Strouhal number of 0.3 and tail amplitude to length ratio of 0.1; we use plate Reynolds numbers of $Re = 6, 12$, and 24×10^3, and focus on $12,000$. As the roughness wavelength is decreased, we find that the undulation wave speed must be increased to overcome the additional drag from the roughness and maintain SPS. Correspondingly, the extra wave speed raises the power required to maintain SPS, making the swimmer less efficient. To decouple the roughness and the kinematics, we compare the rough plates to equivalent smooth cases by matching the kinematic conditions. We find that all but the longest roughness wavelengths reduce the required swimming power and the unsteady amplitude of the forces when compared to a smooth plate undergoing identical kinematics. Additionally, roughness can enhance flow enstrophy by up to 116% compared to the smooth cases without a corresponding spike in forces; this suggests that the increased mixing is not due to increased vorticity production at the wall. Instead, the enstrophy is found to peak strongly when the roughness wavelength is approximately twice the boundary-layer thickness over the Re range, indicating the roughness induces large-scale secondary flow structures that extend to the edge of the boundary layer. This study reveals the nonlinear interaction between roughness and kinematics beyond a simple increase or decrease in drag, illustrating that roughness studies on static shapes do not transfer directly to unsteady swimmers.

3.1 Introduction

The complex and multiscale shape of denticles does not lend itself to systematic investigations into the interplay between surface textures and kinematics. Consequently, we look to simplify the surface texture and focus on the first mode effects of roughness. We need to span a relevant physical space and yet ensure that the parameterisation of the surface is suited for the proposed problem. We look for inspiration in the surface textures/geometries that have been explored in previous studies that have focused on developing methods for predicting drag on flow over rough surfaces (Moody and F. (1944); Jiménez (2004); Flack and Schultz (2010, 2014); García-Mayoral et al. (2019); Chung et al. (2021)). Previous studies have indicated that the ratio of the total projected frontal roughness area to the wall-paralleled projected area (solidity, Λ, Schlichting (1936)) and the mean slope of the roughness texture (in the streamwise and spanwise-directions, also known as effective slope, ES, Napoli et al. (2008)) are two geometric parameters of a rough surface known to significantly affect the flow and forces. These two parameters can be easily altered for structured surfaces where the surface geometry has a sinusoidal shape. In fact, previous works have used sinusoidal roughness where the variation of the two roughness properties can be achieved by only altering the wavelength of the sinusoidal shape (Napoli et al. (2008); Chan et al. (2015); Ma et al. (2020); Ganju et al. (2022)). This presents us with a surface that can be used to understand how the primary scales of roughness (parameterised by a single quantity) interacts with kinematics, with the hope that the findings can be generalised to more complex geometries.

In this work, we study the interaction between kinematics and roughness topologies through high-resolution simulations of a rough self-propelled swimming thin plate. We consider three Reynolds numbers ($Re = 6, 12$, and 24×10^3) with a focus on $Re = 12,000$ (based on swimming speed and chord length) to access moderate Reynolds numbers for the types of flows that are in line with previous efforts (Oeffner and Lauder (2012); Wen et al. (2014); Saadat et al. (2017); Domel et al. (2018); Thekkethil et al. (2018)). We also fix the kinematics of the plate to a simple travelling waveform with a fixed Strouhal number, St, that is in the propulsive regime for flapping foils and has been used extensively in previous studies (Dong and Lu (2007); Borazjani and Sotiropoulos (2008); Maertens et al. (2017); Muscutt et al. (2017); Thekkethil et al. (2018); Zurman-Nasution et al. (2020)). As denticle geometries are complex with several potentially important length scales, we focus on a simple roughness texture with a single-length scale to assess how the topology interacts with the kinematics and impacts the hydrodynamic properties of the swimmer. By combining information from two different, but, well-established topics we hope to understand the influence of one on the other. These dynamic simulations with roughness elements are the first of their kind, allowing us to establish a link between surface roughness and kinematics, and then—with comparison to a smooth kinematic counterpart—directly isolate the nonlinear interaction of the roughness and kinematics.

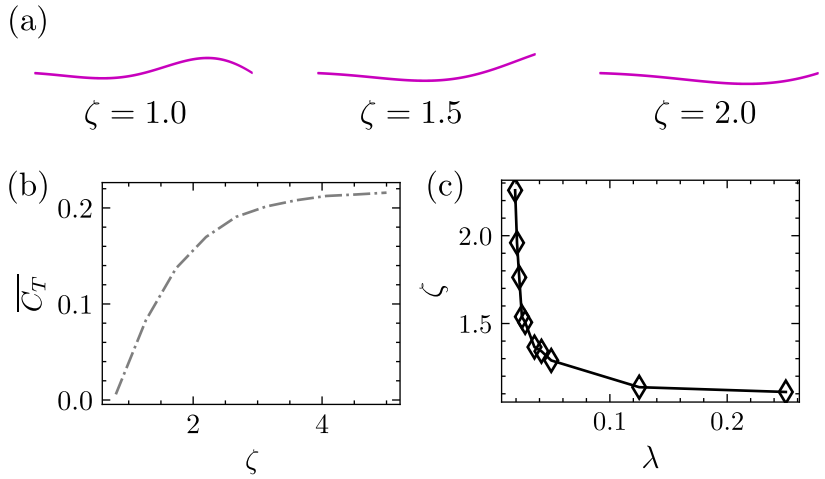

FIGURE 3.1: The impact of ζ on (a) the shape of and (b) the forces on a smooth plate. (c) The required wave speed, ζ, for SPS of a rough plate, given different wavelengths (λ).

3.2 Results

3.2.1 Self-Propelled Swimming

We find the Self-Propelled Swimming (SPS) state by setting the wave speed ζ to zero the mean net thrust $\overline{C_T}$. The wave speed is an effective control parameter to counter roughness adjustments because increasing ζ increases the thrust production, as shown for a smooth plate in figure 3.1b. Figure 3.1a illustrates the change in body shape as the wave speed increases which is a product of fixing the frequency with $St = 0.3$ and letting the wavelength change the wave speed. Changing ζ to achieve SPS allows us to keep Re, St and A_1 constant to test different surface conditions without changing these important swimming parameters identified in the literature. We use Brent's method (Brent, 1971) to find the $\overline{C_T}(\zeta) = 0$ root within a tolerance of 10^{-2} which allows us to balance precision with the number of iterations; the tabulated solutions are presented in table A.2.

Using this approach, we found that a decrease in the roughness wavelength λ requires an increase of ζ to maintain SPS, figure 3.1c. ζ changes with λ like the function $\frac{1}{|\lambda|} + c$ (figure 3.1c). The ζ, λ relationship leads us to restrict λ in the range $(1/4, 1/52)$ as the limits are ill-conditioned. Longer wavelengths asymptote to the smooth SPS ($\zeta = 1.06$) where $\lambda \equiv 1/0$ whilst all $\lambda < 1/52$ are drag-producing for our set-up.

3.2.2 Flow Structures

The structures of the flow provide insight into the workings of the system. Figure 3.2 shows equally spaced time instances making up a whole period of motion for two different swimming modes at $Re = 12,000$. One swimming mode is $\zeta = 1.11$ which

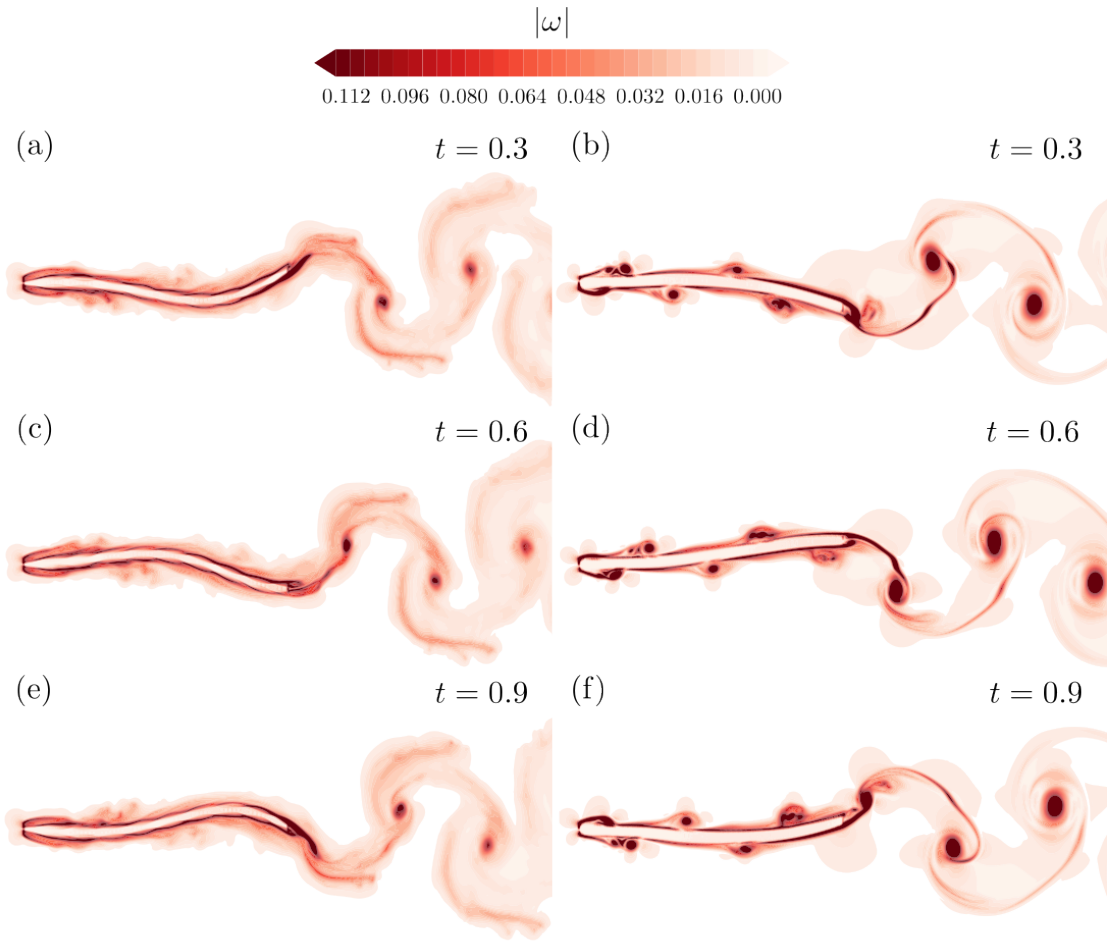

FIGURE 3.2: Sequential snapshots of vorticity magnitude $|\omega|$ for SPS at $Re = 12,000$. The two columns represent different roughness wavelengths. (a,c,d) $\lambda = 1/4$ requiring $\zeta = 1.11$ for SPS. (b,d,e) $\lambda = 1/52$ requiring $\zeta = 2.26$.

is required to achieve self-propelled swimming for a surface of $\lambda = 1/4$, the other is $\zeta = 2.27$ for $\lambda = 1/52$. The high wave speed required to overcome roughness has resulted in strong coherent vortices whilst the lower wave speed has a much more dispersed vorticity field.

As ζ increases, the flow around the plate moves away from those typically associated with swimming. Figure 3.3 shows four snapshots across the range of ζ associated with the surfaces tested. (a) is a smooth comparison and exhibits a two-pair plus two-single ($2P + 2S$) vortex wake structure (Schnipper et al., 2009). For (b), there is an increase in the boundary-layer mixing, and the flow moves back to a more traditional 2P structure. As λ decreases further, the leading edge vortex becomes more defined, with (c) and (d) exhibiting well-defined vortices along the length of their body which is generally associated with a heaving instead of a swimming plate

Figure 3.4 shows the flow structure visualised by isosurfaces of the Q-Criterion (Hunt et al., 1988). For a direct comparison, the contour of the isosurface remains the same between the figures. The flow exhibits a distinguishable transition as ζ increases. For

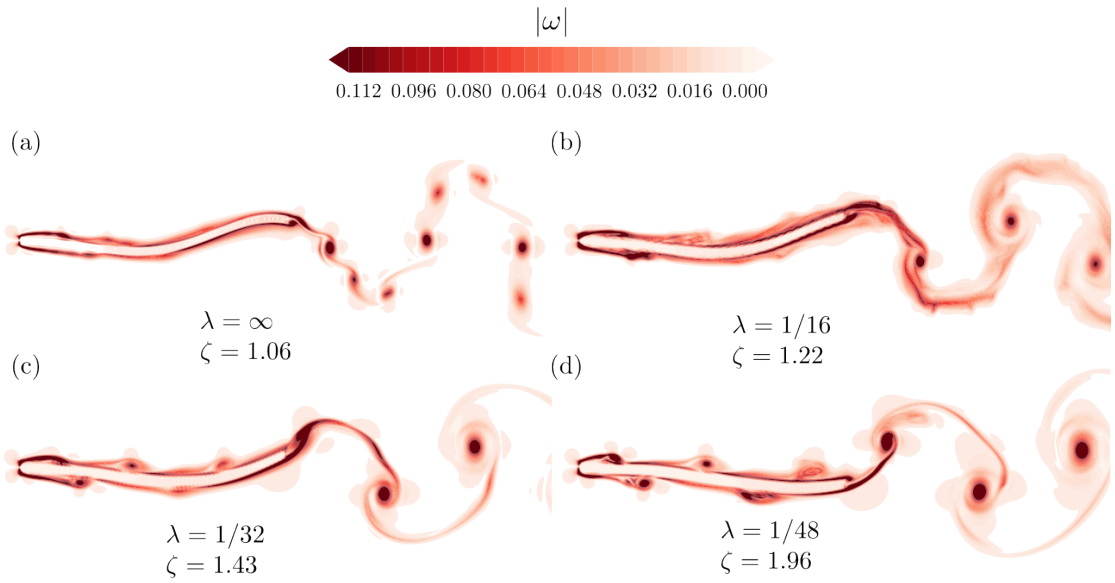

FIGURE 3.3: The change in vorticity magnitude with roughness wavelength. All instances are taken at the same cycle time ($\varphi = 0.1$) and show the spanwise-averaged vorticity magnitude. (a) A smooth plate and (b-d) rough plates defined by decreasing λ.

low ζ the bumps dominate the flow structure, and we see distinct horseshoe vortices shed from each element. These vortices persist downstream into counter-rotating streaks that compose the near wake. The flow structures get smaller as ζ increases and the horseshoe vortex around each element becomes less distinct. From the middle left figure onwards, we can see the near wake collects into a wavy vortex tube similar to those that categorise a two-dimensional flow driven by kinematics Zurman-Nasution et al. (2020).

Next, we study the influence of Re on the self-propelled swimming flow by extending the range to $Re = 6, 12$ and 24×10^3, figure 3.5. The large-scale flow structures such as the leading edge vortex and wake vortices remain similar, but increasing Re is seen to greatly increase the production of small-scale vortices - both on the surface and in the wake. This is because the large-scale structures are driven by the kinematics and the surface topology and the reduced viscosity causes the structures to break down quickly.

3.2.3 Forces

We find that increasing ζ increases the power to maintain self-propelled swimming (figure 3.6a) despite the strong two-dimensionality of the flow structures which are normally associated with efficient power transfer (Zurman-Nasution et al., 2020) as no energy is lost to three-dimensional effects. This means low ζ corresponding to the longer wavelength roughness and associated three-dimensional flow structures are more efficient.

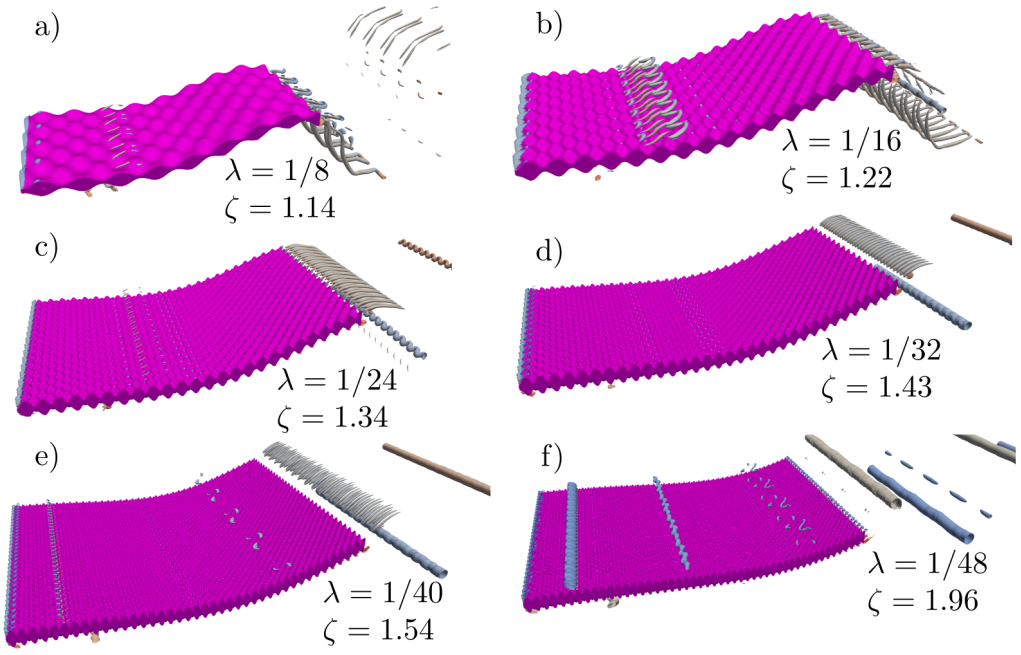

FIGURE 3.4: The Q-Criterion of the flow around a flat plate with a decreasing roughness wavelength. For longer wavelength roughness, the shedding off of the bumps dominate the structures. As the wavelength decreases, the flow transitions to a predominantly two-dimensional state as the influence of the bump perturbations gives way to dominant kinematically-driven structures.

Figure 3.6b show that as ζ increases, as does $RMS(C_L)$. This signals ineffective swimming as the side forces are balanced by the mass $\times$ acceleration of the body's motion so larger side forces on an equally massive body cause the body to accelerate side to side more, decreasing the smoothness. Similarly, increasing ζ also increases $RMS(C_T)$ (figure 3.6d) leading to more of a surging motion, further decreasing the smoothness of the swimming. These signs of ineffective swimming are reflected in the stated increase in $\overline{C_P}$.

To decouple the roughness and wave speed effects, we run a smooth simulation with the same kinematics properties as each rough case. This smooth kinematic counterpart gives a base flow to compare against the rough simulations, and the cycled average power and forces are shown in Figure 3.6. Figure 3.6c illustrates that increasing ζ for the smooth case increases $\overline{C_T}$, making the smooth-plate counterparts slightly thrust producing. The power, $\overline{C_P}$ is reduced by adding roughness to the surface of the plate, Figure 3.6a, for the shorter wavelength roughness tested. Shorter wavelength roughness also reduces $RMS(C_L)$ (figure 3.6b) and $RMS(C_T)$ (figure 3.6d), making the swimming more effective compared to a smooth, kinematic counterpart.

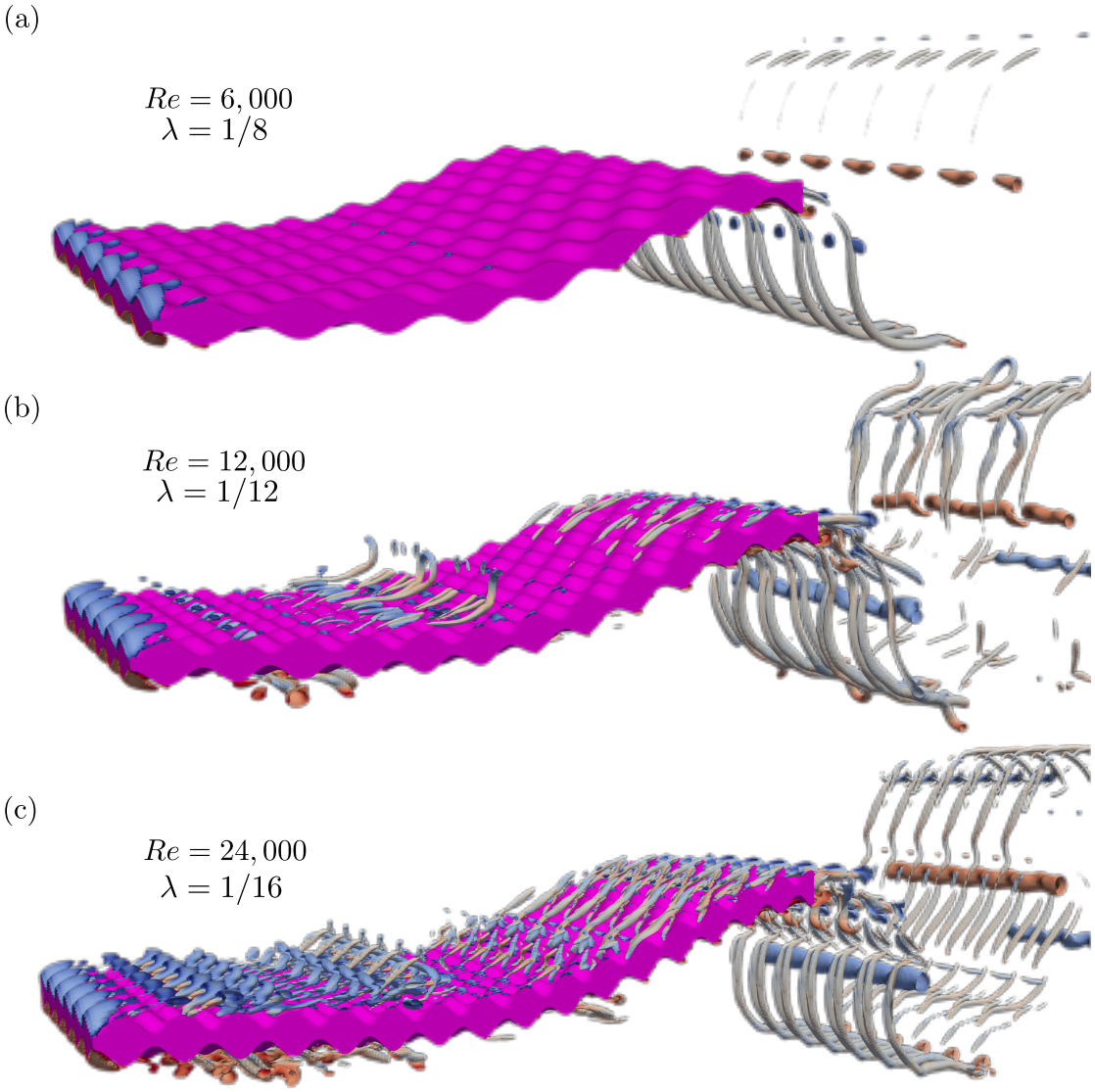

FIGURE 3.5: Flow structures of plates at $Re = 6, 12$, and 24×10^3 visualised by the same q-criterion. The surface topographies, defined by $\lambda = 1/8, 1/12, 1/16$, correspond to the enstrophy peaks discussed in section 3.2.4. An animation of each of these subfigures is available in the supplementary material.

3.2.4 Enstrophy

So far, we have shown surface roughness increases the drag on a surface, leading to inefficient swimming, and have identified variations in the flow structures for different textures and kinematics. To identify the separate fluid dynamic contribution of ζ and λ we look at scaled enstrophy of the rough surface and its smooth kinematic counterpart. We define the scaled enstrophy as

$$E = \frac{\int 0.5|\omega|^2 dV}{SA_1} \tag{3.1}$$

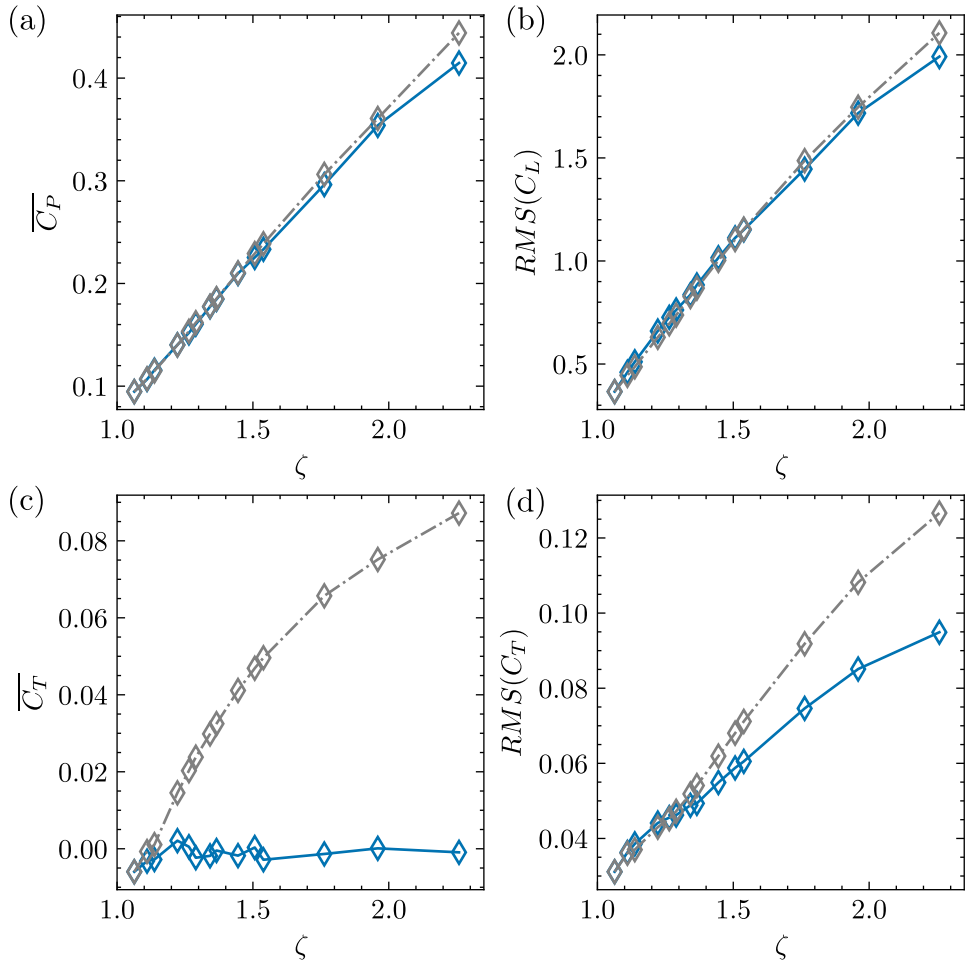

FIGURE 3.6: The key swimming performance and force characteristics of the plate at $Re = 12,000$. (a) The power required to maintain self-propelled swimming. (b) The side force RMS. (c) The time-averaged and (d) RMS thrust. The points making up the solid line are the rough simulations, and the dash-dot line is a kinematically equivalent smooth simulation which matches ζ to the rough case.

where the scaling factor is the planform area times the motion amplitude to define an appropriate reduced volume over which to evaluate the mixing. We use the subscript (r, s) to identify the rough and smooth cases respectively.

In general, the enstrophy increases with Re because of the presence of smaller scale structures (figure 3.5). We show this in figure 3.7a,b, which reports the results of E against ζ for three Re. Figure 3.7a are the results of the rough plate undergoing self-propelled swimming and figure 3.7b are the enstrophy for the smooth, kinematic counterparts. Both the smooth and rough plates have an approximately linear increase that scales with $\log Re$.

The positive gradient of both the smooth and rough enstrophy shows enstrophy increases with ζ, and the offset between the smooth and the rough line indicates that adding roughness also increases enstrophy. As we increase ζ, the enstrophy increases for both

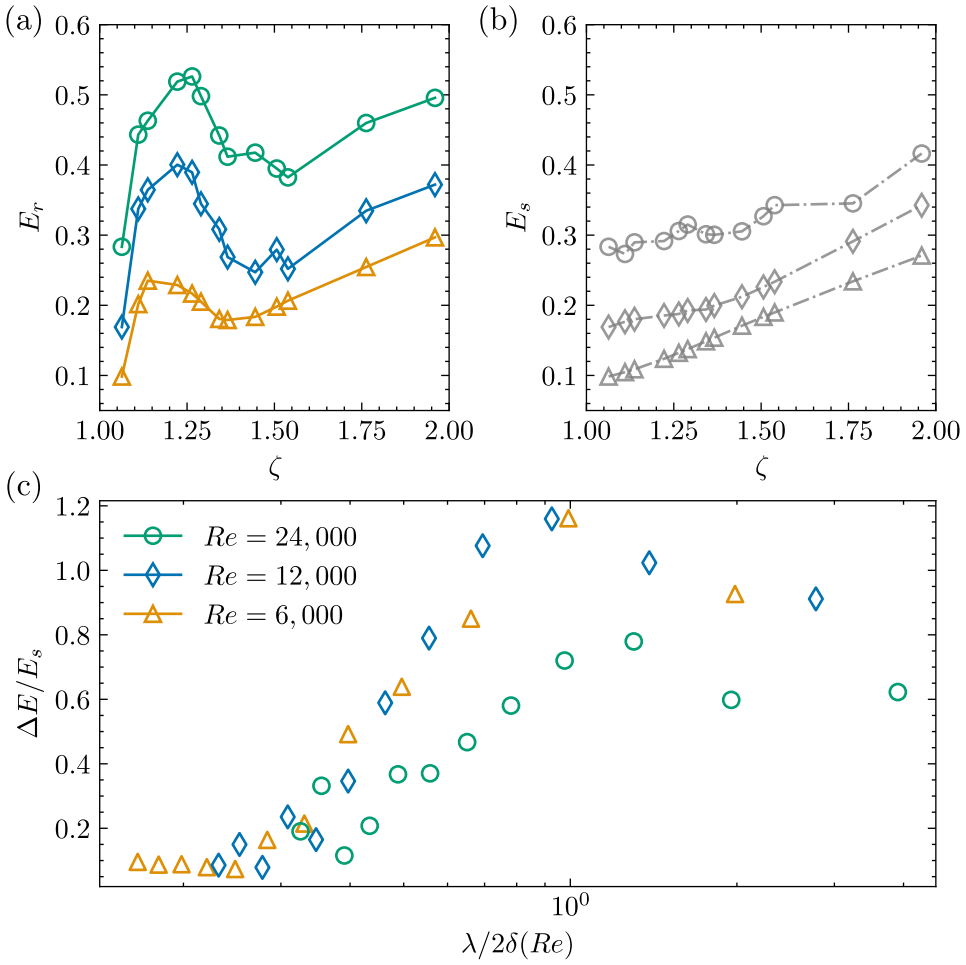

FIGURE 3.7: (a) The ζ-dependant enstrophy for the rough, self-propelled swimming plates (E_r) where higher ζ corresponds to lower λ. The circle, diamond and triangle markers correspond to $Re = 6, 12$ and 24×10^3 respectively. (b) The enstrophy for the kinematically identical smooth plate E_s where the dash-dot line identifies the data as smooth and the markers relating to the Re correspond as before. (c) The difference between the smooth and the rough enstrophies, ΔE with respect to $\lambda/2\delta(Re)$. We take $\delta(Re)$ as the approximation of a laminar boundary-layer thickness on a smooth, flat plate. The same markers are used to distinguish Re, and the colours orange, blue and green (online) correspond to $Re = 6, 12$ and 24×10^3 to aid in the distinction.

the smooth and the rough cases. At the upper limit of ζ, the smooth and the rough lines start converging as the rough flow, like the smooth, becomes two-dimensional (figure 3.4).

One prominent feature of figure 3.7a are the peaks in enstrophy found between $\zeta = 1.1 - 1.3$. The peak in enstrophy coincides with the superposition of the flow features associated with both the roughness and kinematics (figure 3.5). This is evident as surfaces with shorter λ are increasingly dominated by the two-dimensional vortex tubes associated with the kinematic flow as the structures shed off the roughness elements decrease in size (figure 3.4b-f), and surfaces with longer λ are dominated by the flow off the roughness elements (figure 3.4a,b).

The mechanisms driving the peak in enstrophy are analogous to an amplification of flow structures found in Prandtl's Secondary Motions of the Second Kind (Johann Nikuradse, 1926; Ludwig Prandtl, 1926); where secondary currents were induced when the surface texture has features that scale with the outer length-scale of the flow. In fact, Hinze (1967, 1973) found secondary-currents form when surface roughness has dominant scales comparable to the boundary-layer thickness (or pipe/channel height). These secondary currents manifest as low and high-momentum pathways in the flow (Barros and Christensen, 2014) that are further sustained by spatial gradients (Anderson et al., 2015). Vanderwel and Ganapathisubramani (2015) identified that the spatial gradients and the strength of these secondary currents are maximised when the spanwise-spacing between successive roughness features are approximately equal to the boundary-layer thickness. When the spacing is small, the flow behaves more like a homogeneous rough surface. When the spacing is much larger than the secondary motions, the currents are spatially confined (and small) to the location of the roughness. The analogy to the case presented in this manuscript is not a direct comparison to Prandtl's Secondary Motions of the Second Kind as the flow is merely unsteady, although, the system studied herein meet certain criteria. Specifically, large-scale streamwise vortical structures (figures 3.4 and 3.5) driven from torque associated with anisotropy of the velocity fluctuations (Perkins, 1970; Bottaro et al., 2006).

The increasing Re shifts the peak enstrophy in figure 3.7a towards higher ζ (lower λ) resulting in flow fields shown in figure 3.5. The enstrophy peaks occur at $\lambda = 1/8, 1/12$ and $1/16$ for $Re = 6, 12$ and 24×10^3 respectively. In fact, estimating the value of $\delta(Re)$ by assuming a laminar boundary-layer correlation ($\delta(Re) \approx 4.91 Re^{-0.5}$), and leveraging an approximate scaling $\lambda/2\delta \approx 1$ yields results where $\lambda(Re) = 1/7.9, 1/11.5$, and $1/15.8$ for $Re = 6, 12$, and 24×10^3. These estimations are remarkably close to the true, enstrophy peaking wavelengths, so future studies can use this estimation to assess the importance of their dominant roughness length scales. The laminar boundary-layer value of δ is taken since it is difficult to estimate a value of δ for the swimming plate. At these Reynolds numbers, δ could also be estimated using a turbulent boundary-layer correlation ($\delta \propto Re^{0.2}$) since there is very little difference between the laminar and turbulent values.

Further, we can delineate the relationship between λ and and the boundary-layer thickness by plotting the normalised difference in enstrophy between the smooth and the rough plate ($\Delta E = (E_r - E_s)$) against $\lambda/2\delta(Re)$ (figure 3.7c). Figure 3.7c shows a strong collapse of the $\Delta E/E_s$ curves when plotted against $\lambda/2\delta(Re)$ for $Re = 6$ and 12×10^3. The scaled maximum of both curves is 1.16 at $\lambda/2\delta(Re)$ just less than 1. The collapse breaks down at the highest $Re = 24 \times 10^3$ because the flow on the smooth plate experiences a jump in E_s at this Reynolds number, affecting the enstrophy differences.

Finally, in our study, the power increases almost linearly until $\zeta \approx 1.8$ (figure 3.6a) and our enstrophy peak lies within this regime. This means that the accentuation of these

secondary flows is truly a boundary-layer scaling, and not a result of increased vorticity production at the wall, which would result in an increased force on the body. Therefore, we can relate the system's increase in mixing to scaling arguments previously defined in turbulent wall-flows.

3.2.5 Boundary-layer-scale breakdown

The breakdown of the δ-scaling coincides with the disorganisation of the flow at high Re. To correlate the breakdown, we run extra simulations of a smooth SPS plate at $Re = 3, 9, 18, 36$ and 48×10^3. The phase-portraits of E (figure 3.8) show that for $Re < 18,000$, the cases remain largely periodic. At $Re > 18,000$, the periodicity of the enstrophy breaks down which corresponds to the scaling observations in figure 3.7c.

To quantify the periodicity of the flat plate base flow we look at the autocorrelation defined as

$$\mathcal{A}_E = \frac{\Sigma E(\varphi) E(\varphi + \Delta t)}{\sqrt{\Sigma E(\varphi)^2 \Sigma E(\varphi + 1)^2}} \tag{3.2}$$

where $E(\varphi)$ is the enstrophy at $\varphi = 2\pi f t$. The autocorrelation is a measure of the periodicity of the flow, where $\mathcal{A} = 1$ is a perfectly periodic flow and $\mathcal{A} = 0$ is a completely random flow. Figure 3.9 shows the autocorrelation of the enstrophy for the smooth plate at different Re. The autocorrelation shows periodic flow at $Re < 18,000$ and becomes random from $Re > 18,000$. This is consistent with the phase portraits in figure 3.8 and the breakdown of the δ-scaling in figure 3.7c. The breakdown of the δ-scaling is a result of the breakdown of the periodicity of the flow.

3.3 Conclusion

In this chapter, we examined the effect of an egg carton-type rough surface on a Self Propelled Swimming Body. We varied the wavelength of the surface to understand how different surface topologies change the flow and performance of the swimmer. We found a decrease in the roughness wavelength requires a greater wave speed to maintain self-propelled swimming. The greater wave speed changed the vortex structures and consolidated the vorticity into two-dimensional packets with a distinct leading edge vortex propagating down the body. The long wavelength rough surfaces were dominated by the shedding of horseshoe vortices from individual roughness elements that persisted in the wake. The thrust of the plate increased with wave speed, which was needed to overcome the drag induced by the roughness. The increased wave speed also increased the required power and the amplitude of the non-propulsive lift

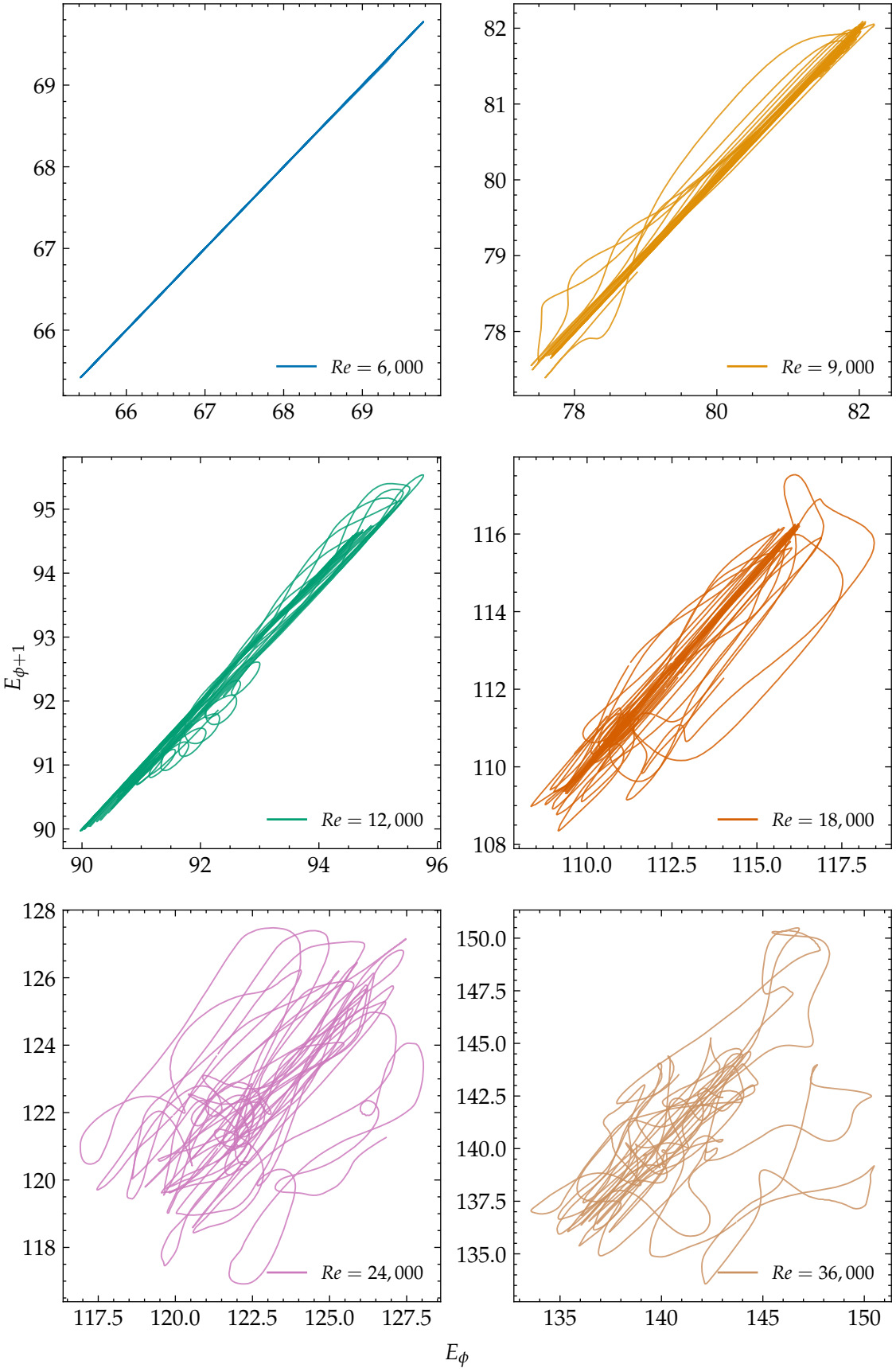

FIGURE 3.8: Phase portraits of E for smooth SPS plates at different Re

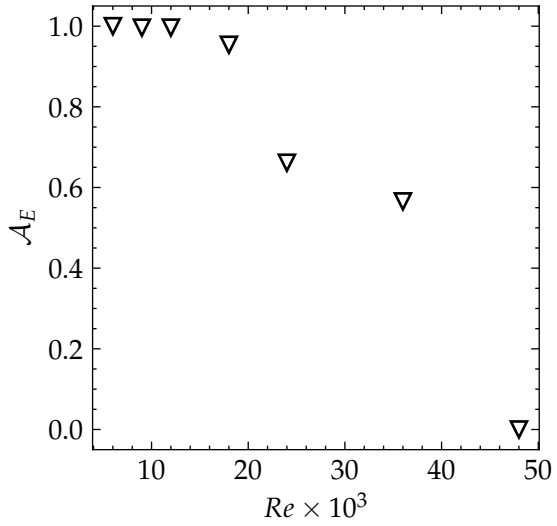

FIGURE 3.9: The autocorrelation of the enstrophy for the smooth plate at different *Re*.

force. These increases implied the plate was less efficient, less effective, and less steady in its swimming. To decouple the effects of roughness and kinematics we compared the forces and enstrophy to a smooth swimmer with identical kinematics. We saw that, compared to the smooth cases, the roughness reduced the power required, as well as the amplitude of the lift and drag forces. There was a peak in enstrophy which coincided with a superposition of two flow modes, one dominated by three-dimensional structures and the other by the two-dimensional vortex tubes. The peak in enstrophy persisted over all three Reynolds numbers, and collapsed when the roughness wavelength is proportional to the boundary-layer thickness. This spike in enstrophy is not a result of increased vorticity production at the wall because we do not have a corresponding increase in body force. Further, this boundary-layer relationship is analogous to scaling arguments defined for turbulent wall-flows (Vanderwel and Ganapathisubramani 2015).

These results show that you cannot ignore kinematics when assessing the performance of a swimmer with surface texture. Oeffner and Lauder (2012) and Wen et al. (2014) reported an increase in speed and efficiency for their experiments, but we have shown a change in wave speed dominates the thrust production of the plate. Adding a coating to a surface could increase the stiffness and thus increase the wave speed, causing the plate to swim faster. Another factor to consider is the structural resonance, which significantly affects the performance of flexible plates undergoing swimming (Quinn et al. 2014). Any study attributing performance changes to surface textures must show the independence of their test cases to the kinematics.

We have identified non-linear interactions between the roughness and kinematics that amplify this mixing without a nonlinear force or power increase. Other studies (Lang et al. 2008; Afroz et al. 2016; Santos et al. 2021) have identified the bristling of shark skin and conjectured that the increased mixing helps keep flow attached in the flank region.

This work is significant in understanding the hydrodynamic effect of surface textures on the flow and forces around a swimmer, it is the first study to look at surface textures on undulating surfaces with realistic and well-defined kinematics. However, it is limited in that the roughness elements are a hundred times larger than actual denticles, and Re is only representative of a small, slow-swimming shark.

Chapter 4

Resolvent analysis of a swimming foil

This chapter is in preparation for submission to Journal of Fluid Mechanics.

This study investigates the boundary-layer dynamics of a swimming foil by using data-driven resolvent analysis (Herrmann et al., 2021) and a body-coordinate transform. We demonstrate that the foil's boundary-layer is sensitive to a spectrum of harmonics, mainly phase-locked, differing significantly from a stationary foil. This indicates a substantial impact of swimming motion on boundary-layer stability. The analysis reveals varied high and low-wavenumber structures in the swimming foil's forcing modes, while its response modes show frequency invariance. The resolvent mode spectra uncover dominant spatial structures near the boundary layer, with forcing modes displaying diverse wavenumbers and response modes consistent. Finally, this study shows that the most sensitive region of the flow is right next to the body, exhibiting large fluctuations, at a range of distinct spatial wavenumbers. These findings emphasise the impact of swimming motion on boundary-layer stability and suggest the potential of flow control through properly tuned surface roughness.

4.1 Introduction

In chapter 3, we examined the effects of surface topography on the flow and performance of a Self-Propelled Swimming (SPS) body. We showed that the enstrophy of the flow followed an outer-scaling that reached a peak at $\lambda/2\delta(Re) = 1$. This scaling breaks down when the aperiodicity of the base flow increases. The study highlights a non-linear relationship between roughness and kinematics beyond a simple increase in drag. However, the study was limited to a flat plate, and so the effects of roughness on a body with shape and a flow at a higher Re remain unknown.

Stability analysis of fluid flows helps to understand and predict the behaviour of the system. Canonical stability analysis comes from analysing the Orr-Somerfield equation (Orr, 1907; Sommerfield, 1908; Orszag, 1971), which is an eigenvalue equation describing linear, two-dimensional modes of disturbance to a viscous parallel flow. However, Trefethen et al. (1993) showed that the non-normality of linear operators that arise from all but a few specific solutions to the Navier-Stokes–especially when extensions are made to three-dimensions–can potentially lead to psuedoresonance, transient growth, and destabilising perturbations. They laid the groundwork for what is now called resolvent analysis by studying the response of systems to deterministic disturbances. Jovanović and Bamieh (2005) further developed this theory, emphasising an input-output viewpoint crucial for understanding localised disturbances in multi-physics systems. Resolvent analysis in its modern form stems from the work of McKeon and Sharma (2010), and relies on the concept of the resolvent operator, which treats the non-linearity in the fluctuating part of the Navier-Stokes equations as an unknown harmonic forcing. This approach offers a low-rank approximation of forcing-response dynamics, immensely useful for modelling, controlling, and comprehending fluid flow physics.

The practical application of resolvent analysis faces challenges due to the need for high-fidelity solvers for the linearised governing equations and the significant computational demands of handling large operators. These challenges are being addressed through randomised numerical linear algebra methods (Ribeiro et al., 2020), reducing computational expense and memory requirements. Additionally, there's a growing interest in adopting data-driven approaches for obtaining the resolvent operator, bypassing the need for governing equation access and potentially reducing computational burdens (Herrmann et al., 2021).

Herrmann et al. (2021) proposes a unique methodology that uses the link between the Dynamic Mode Decomposition (DMD) and koopman eigenfunctions (Williams et al., 2015) to construct the linear basis to analyse. DMD, introduced by Schmid (2010), is enables the extraction of spatio-temporal patterns from time-resolved data. The availability of well maintained, and optimised codes, such as Demo et al. (2018) reduces the barrier for resolvent analysis, surpassing the need to set up operators $O(9N^2)$.

The challenge for a moving and deformable body is that the domain position containing the fluid and the body depend on time. Goza and Colonius (2018) successfully coupled the fluid and body domains to identify the driving mechanisms for the onset of chaotic flapping however, their body was an infinitesimally thin membrane. Menon and Mittal (2020) looked at the pitching and plunging of an airfoil by rotating and translating the reference frame, so the body remained centred within the reference frame. This is limited in that it deals with a rigid body.

i	1	2	3	4	5	6	7	8	9	10
a_i	0.6	-0.5	-28.1	222.5	-846.5	1883.7	-2567.4	2111.0	-962.2	186.8

TABLE 4.1: Values for the coefficients from equation 4.2.1

In this chapter, we investigate the stability of a swimming foil using resolvent analysis. We use a modified NACA foil shape to represent a fish-like body, and a generalised SPS motion to represent the kinematics. We propose a coordinate transform to study the boundary layer of a swimming foil in body coordinates. This approach allows us to use readily available DMD codes, and the same methodology as Herrmann et al. (2021) to perform resolvent analysis on the boundary layer of a swimming foil. To our knowledge, this is the first study of its kind to use both DMD on deformable bodies with non-zero thickness, and subsequent resolvent analysis. Further, it enables the study of the boundary-layer dynamics of a swimming foil at realistic swimming *Re*.

4.2 Methodology

4.2.1 Geometry

We use a NACA0012 profile with a modified leading edge to represent a fish-like body. The details for the modification of the foil are set out in Appendix C.4, and the equation for a half section is given by

$$y(x) = a_i x^i + a_{(i+1)} i x^{(i+1)} ... + a_n x^n \tag{4.1}$$

where $n = 10$ and the coefficients are defined in table 4.1.

4.2.2 Kinematics

We employ the same kinematic equation as in chapter 3 (equation 2.25), where the foil undergoes a generalised SPS motion. In contrast to chapter 3, where we modified the coefficients in equation 2.26 to extend SPS across a broader range of λ, such adjustments are unnecessary for the foil shape. Therefore, we adopt $a_{0,1,2} = (0.05, -0.13, 0.28)$, as detailed by Di Santo et al. (2021).

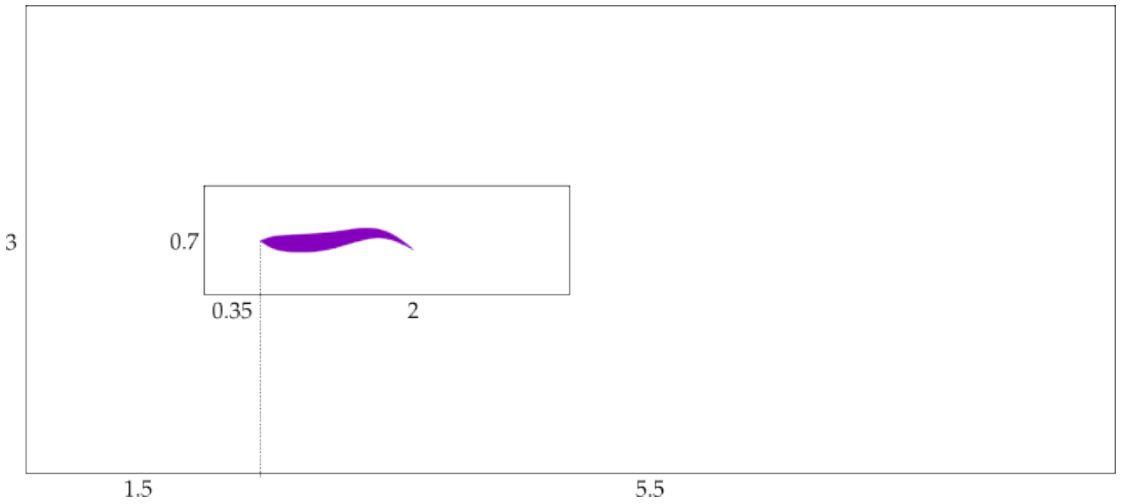

FIGURE 4.1: Illustration of the computational domain size. The insert shows the rectilinear, inner-domain.

4.2.3 Numerical method

We use the same numerical method as in chapters 2 & 3. The computational space is illustrated in figure 4.1; we use a domain size of $x \in [-1.5, 5.5], y \in [-1.5, 1.5]$, and $z \in [0, 1/16]$. The inner domain is defined $x \in [-0.35, 2], y \in [-0.35, 0.35]$, and extends throughout of z. The grid is uniform and rectilinear in the inner domain, with a refinement ratio of $4:1:4$ for $\Delta x, \Delta y$, andΔz, it is then stretched in the outer domain using hyperbolic stretching. The total number of grid cells is $N = (4096, 4096, 64)$ totalling $N = 1.7 \times 10^9$ grid cells. We show the domain and grid resolution are sufficient in Appendix C.4. We save 800 snapshots over 4 cycles, with a time-step of $\Delta t = 0.0033$ for the swimming case, and 3400 snapshots over 17 convective cycles for the stationary case, giving a time-step of $\Delta t = 0.005$.

4.2.4 Unmapping the flow

For a body with non-zero thickness and not stationary in time, DMD produces inaccurate modes around the body motion (Menon and Mittal, 2020). This would restrict analysis to the wake, and miss valuable insights into the boundary-layer dynamics. To overcome this, we transform the flow into the body coordinates. We do this by taking velocity profiles normal to the body, which are interpolated from the original solution to give a uniform grid in body coordinates.

4.2.5 Resolvent analysis

We use the methodology from Herrmann et al. (2021) to form the resolvent analysis. Accordingly, we use Dynamic Mode Decomposition (DMD) to approximate the eigenvalues

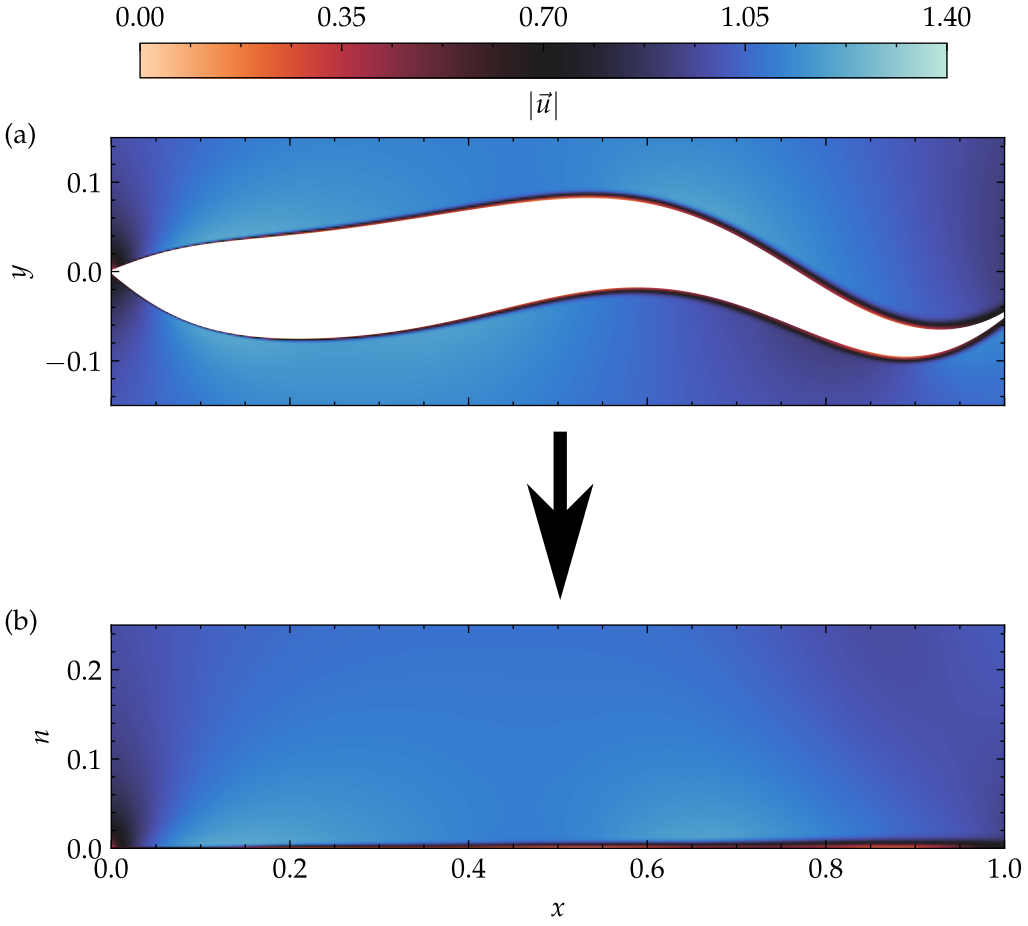

FIGURE 4.2: Schematic of the coordinate transform from the computational domain (a) to the body coordinates (b).

and eigenvectors of the dynamical system. We adopt the forward-backward DMD approach by (Dawson et al., 2016) for this analysis as this yields the best results for our case. Our dynamical system's evolution is described by

$$x_{k+1} = \exp(A\Delta t)x_k \,, \tag{4.2}$$

where x_k is the state at time $t_k = k\Delta t$. We use the u and v components of the velocity field as our state vector and assemble data matrices X and Y, from state snapshots. Next, we implement the fbDMD algorithm (Appendix B, Dawson et al. (2016)) with mode truncation $m = 40$. This yields the matrices $D_m, V_{m,F}, W_{m,F}$, where $D_m = diag(\varsigma_1, \varsigma_1, \ldots, \varsigma_1)$ are the eigenvalues and $V_{m,F}, W_{m,F}$ are direct and adjoint eigenvectors respectively. These are related to the operator A by $\Lambda_j = \log(\varsigma_1)/\Delta t$, fulfilling $AV = V\Lambda$ and $A^+W = W\Lambda^*$, where A^+ is the adjoint of A.

For the resolvent analysis, we approximate the resolvent operator using Λ_m, V_m, and W_m by considering a forced system. As such, we expand x and f in eigenvectors:

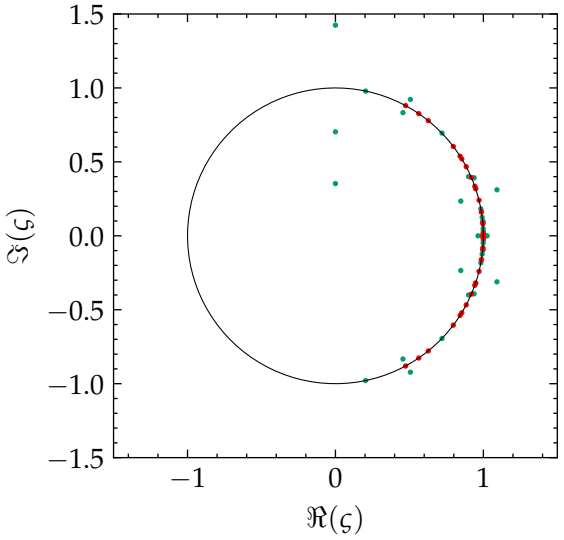

FIGURE 4.3: The real and imaginary eigenvalues for the DMD, plotted in relation to a unit circle. The red dots correspond to the eigenvalues of the stationary foil, and the green to the swimming foil.

$x(t) = V_m a(t)$ and $f(t) = V_m b(t)$, with a, b being expansion coefficients. The inner product with W_m transforms the system into

$$\dot{a} = \Lambda_m a + b \,. \tag{4.3}$$

To maintain the 2-norm's physical meaning, we adjust the inner product via a weighting matrix defined from the Cholesky factorisation of $V_m^* V_m = \widetilde{F}^* \widetilde{F}$. The resolvent analysis then proceeds with the SVD of the resolvent operator

$$\widetilde{F}(-i\omega I - \Lambda_m)^{-1}\widetilde{F}^{-1} = \Psi_{\widetilde{F}} \Sigma(\omega) \Phi_{\widetilde{F}}^* \,, \tag{4.4}$$

synthesising resolvent modes into physical coordinates, $\Phi = V_m \widetilde{F}^{-1} \Phi_{\widetilde{F}}$ and $\Psi = V_m \widetilde{F}^{-1} \Psi_{\widetilde{F}}$ are the forcing and response modes respectively.

The validation of the resolvent analysis methodology, and our implementation is presented in Appendix C.4. We simulate the flow around a stationary foil at $Re = 10,250$ and $\alpha = 0°$, and compare the results to the numerical, and data-assimilated experimental data of Symon et al. (2019). We find that the results are in good agreement.

4.2.6 DMD basis

The DMD of the flow field forms the basis for the resolvent analysis. The eigenvalue spectrum obtained from DMD reveals stable modes that lie around the unit circle (figure 4.3). These modes are well captured by the DMD algorithm and thus form a good basis for the linear operator. Figure 4.3a shows the eigenvalues for the stationary foil

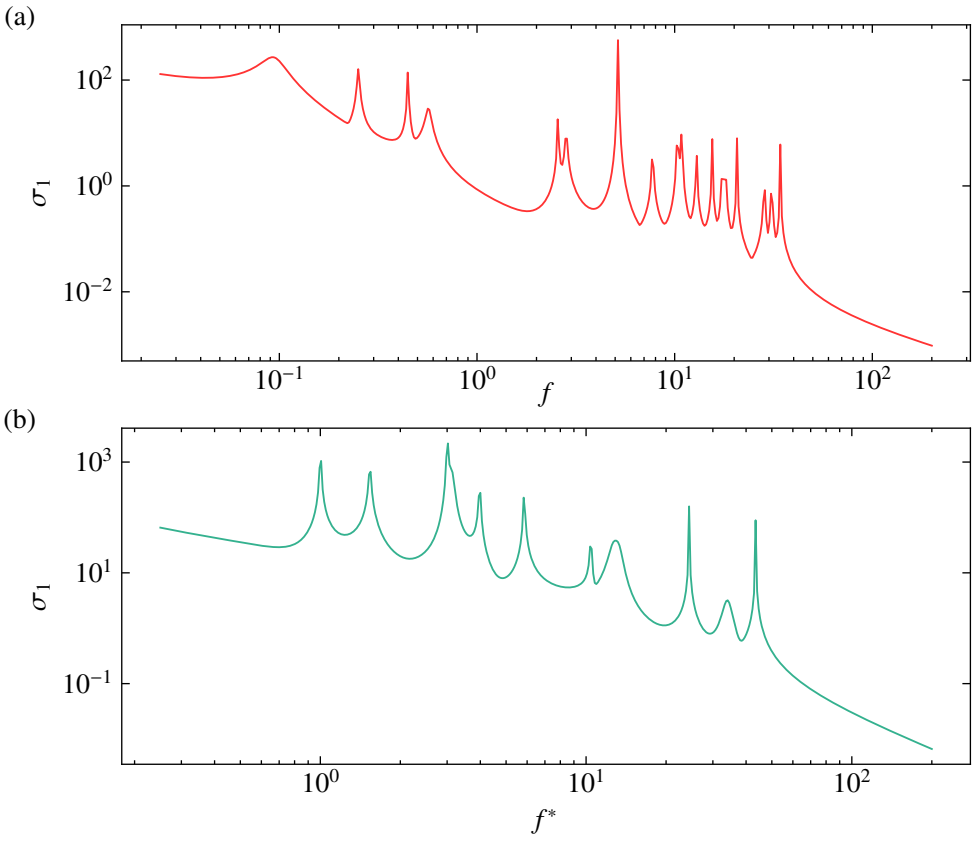

FIGURE 4.4: The maximum gain of the resolvent operator for the stationary foil at $Re = 10,250$ (a), and the swimming foil at $Re = 100,000$ (b).

lie perfectly on the unit circle, indicating that the basis is periodic. The eigenvalues for the swimming foil (figure 4.3b) lie mainly on the unit circle, with a few spurious exceptions. This is likely due to the higher Re and the complexities involved in adding the swimming motion. These results show that the DMD basis is a good approximation for the linear operator.

4.3 Results

4.3.1 Maximum gain

The maximum gain of the first mode of the resolvent operator exhibits distinct peaks across various frequencies. Figure 4.4 displays this gain for both the stationary (a) and swimming (b) foils. A peak of the gain for the stationary, validation case occurs at $f = 3$, closely aligning with the most unstable mode identified in the unmapped flow of the validation case ($f \approx 3$). This correspondence suggests that the resolvent analysis on the coordinate transformed flow effectively captures dynamics similar to those of the global system. Notably, the number of peaks in figure 4.4 correlates with, but does not exactly

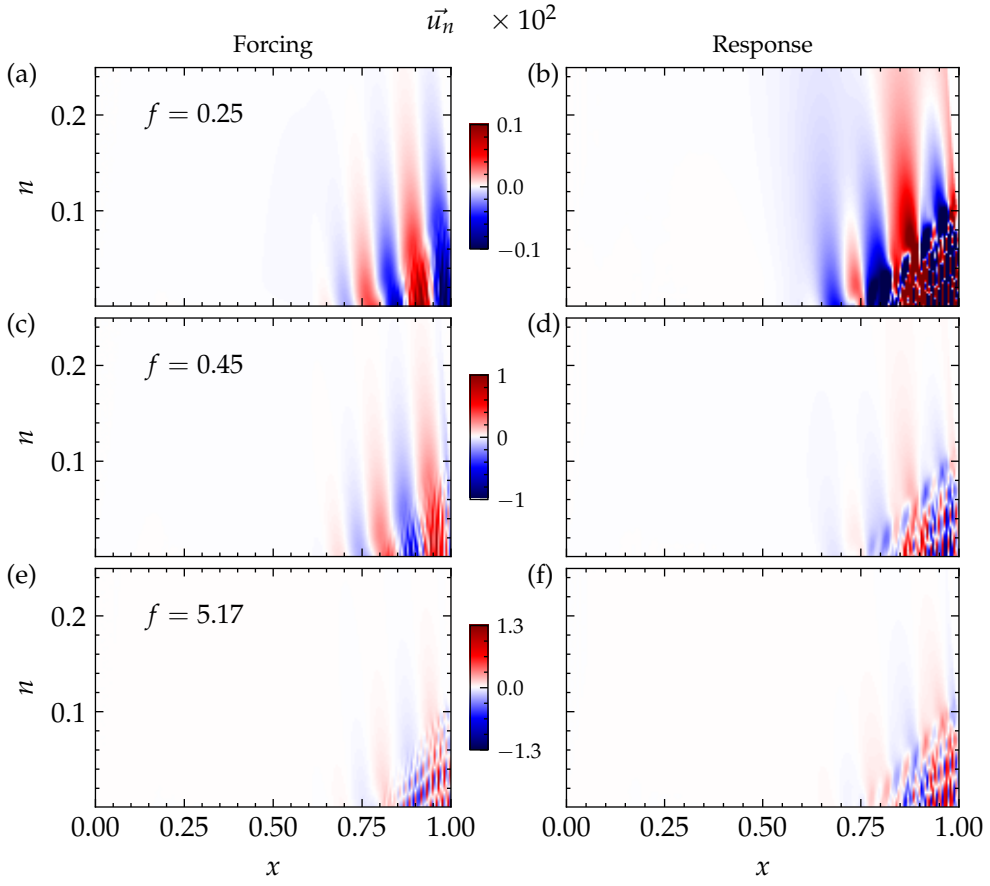

FIGURE 4.5: The forcing (a, c, e) and response (b, d, f) modes of the body normal velocity component $\vec{u_n}$ for the stationary foil.

match, the number of modes in the Dynamic Mode Decomposition (DMD) basis; there are 10 peaks in figure 4.4(b), yet the DMD basis comprises 40 modes.

For the swimming foil, the maximum gain follows a trend akin to that of the stationary foil, marked by multiple peaks at varying frequencies. These peaks often occur at integer values of f^*, where $f^* = 2Af/St$, suggesting that the sensitive frequencies are phase-locked. The maximum gain for the swimming foil is noted at $f^* = 3$.

4.3.2 Resolvent modes

Stationary foil

The resolvent modes of the stationary foil (figure 4.5) exhibit instabilities around the tail, where flow separation commences. The forcing modes present two distinct regions, characterised by low and high wavenumber structures. Forcing modes driven by low frequency perturbations are predominantly influenced by large wavenumber structures (figure 4.5a,b), while those driven by high frequency perturbations are governed by low wavenumber structures(figure 4.5b,c. The response mode to low frequency perturbations

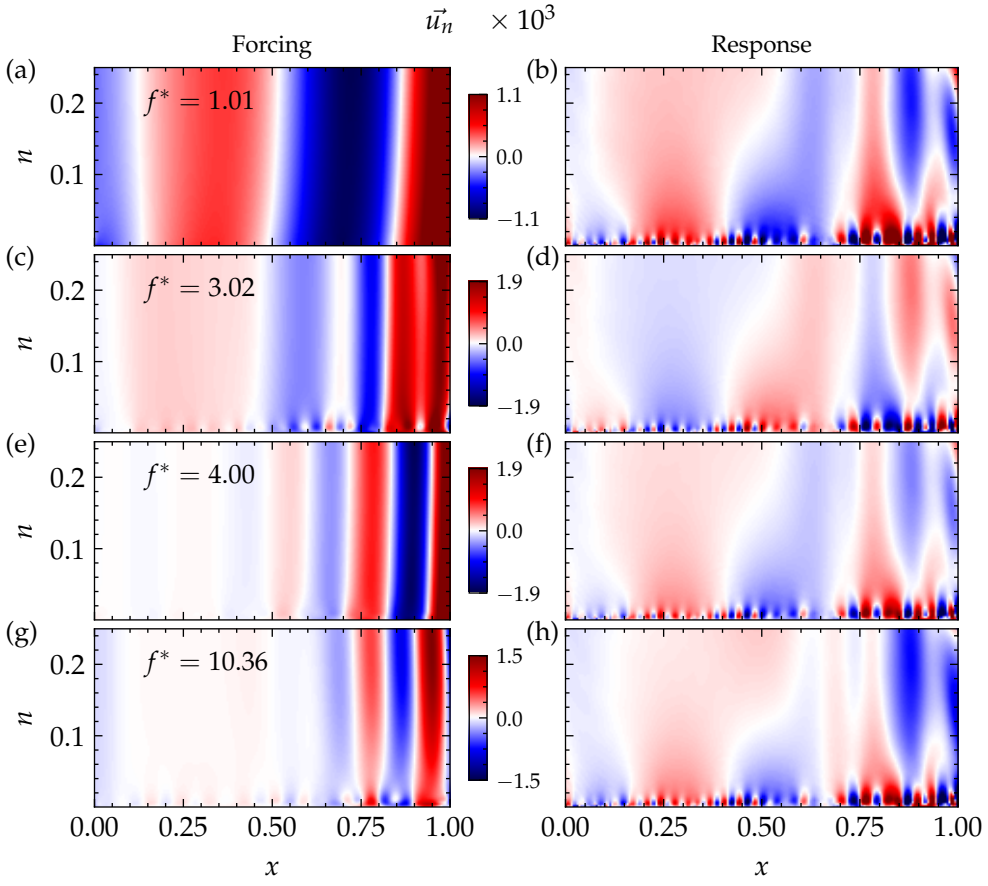

FIGURE 4.6: The forcing (a, c, e, g) and response (b, d, f, h) modes for the body normal velocity component $\vec{u}_n$.

mirrors the structure of the forcing mode, but includes a greater presence of low wavenumber structures (figure 4.5b). In contrast, the response mode to high frequency perturbations, although similar in structure to the forcing modes (figure 4.5d,f), exhibits a downward reaction in spatial scales, with high wavenumber structures gaining magnitude.

Swimming foil

The forcing and response modes of the swimming foil, as depicted in figure 4.6, differ qualitatively from those of a stationary foil. The forcing modes display structures primarily characterised by low-wavenumber scales in the outer-flow (figure 4.6a). The low-wavenumber structures, oriented perpendicularly to the body boundary, vary with the excitation frequency, with a visible reduction in k_x going from figure 4.6a to figure 4.6g.

In contrast, the response modes exhibit a largely consistent structure across various perturbation frequencies, with only minor variations in magnitude (figures 4.6b, d, f,

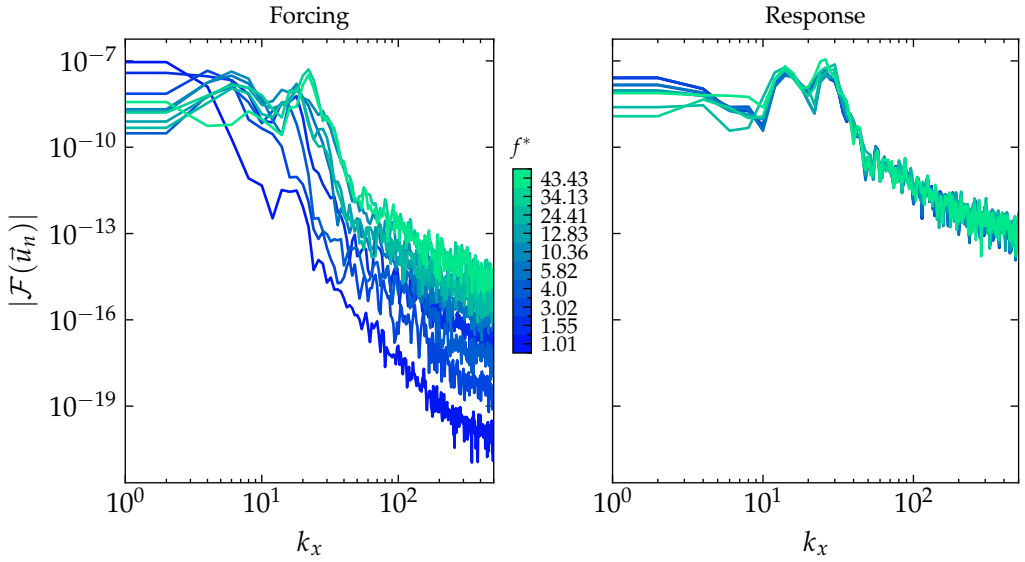

FIGURE 4.7: The spatial wavenumber of the forcing (a), and response (b) modes at a distance of $n = 0.005$. Each line corresponds to a peak in figure 4.4. The fft's are taken using Welch's method with 2 bins.

h). This consistency suggests a robust boundary-layer response mechanism, relatively unaffected by the excitation mode.

Except for the lowest frequency forcing mode (figure 4.6a), distinct spatial structures across the entire length of the foil are present in the boundary layer of the resolvent modes of the swimming foil. These structures aren't present in the stationary foil, and is likely due to the swimming motion.

4.3.3 Spatial wavenumber

The spatial wavenumber of the forcing modes for the resolvent peaks (figure 4.4b) vary depending on the excitation frequency, whereas the response wavenumbers are largely similar. Figure 4.7 shows the spatial wavenumber of the forcing and response modes at a distance of $n = 0.005$ from the body boundary, where each line corresponds to a peak in the gain (figure 4.4b). In figure 4.7, we can see that the forcing modes exhibits a range of dominant wavenumbers in the spectra of the forcing modes, with the dominant wavenumbers lying at peaks of $k_x \approx 5$ and $k_x \approx 20$. The wavenumber where $k_x \approx 20$ corresponds to the up and down welling structures we might associate with roughness. The response modes, however, exhibit two consistent wavenumbers of $k_x \approx 14$ and $k_x \approx 30$. The consistency of the response modes suggests that the boundary-layer response is insensitive to the perturbation frequency.

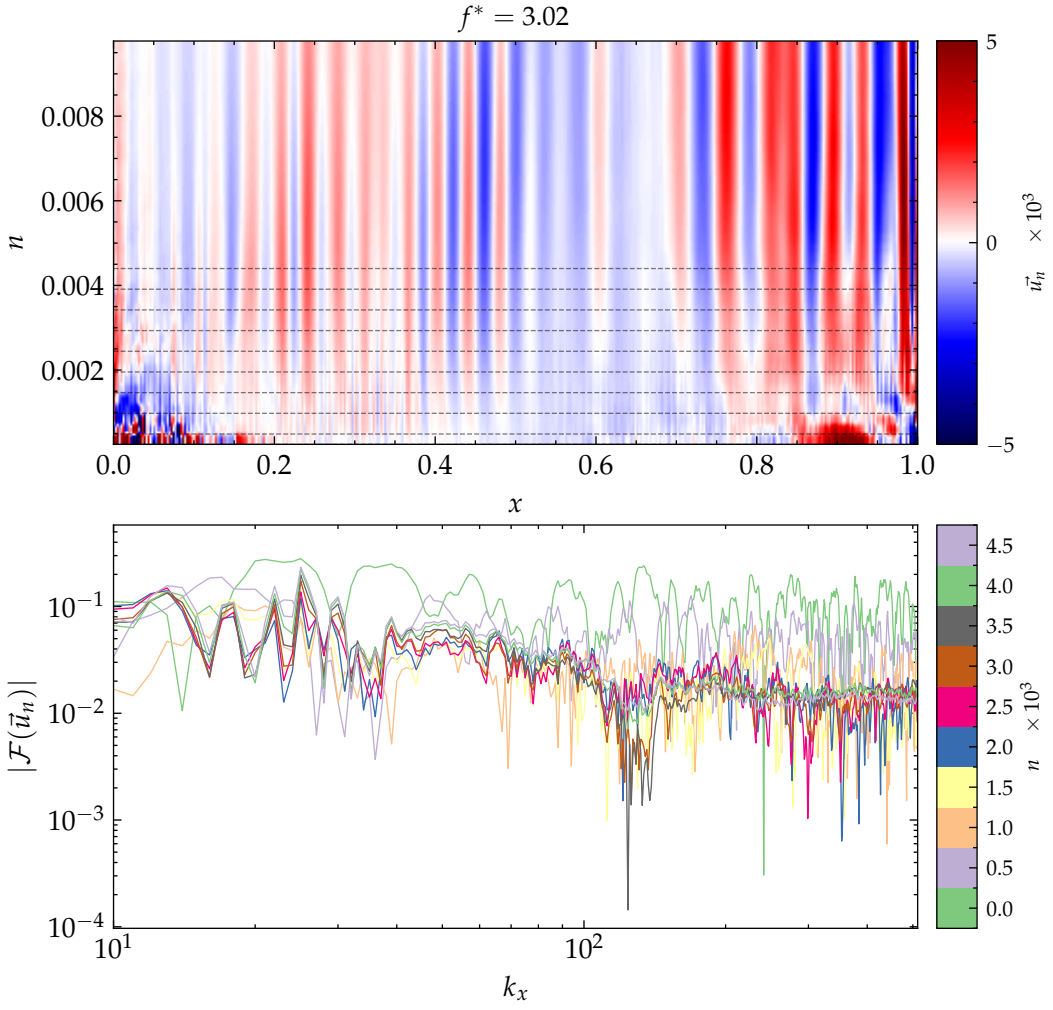

FIGURE 4.8: A zoomed in view of the response mode (a), for the case $f^* = 3$, corresponding the maximum gain (figure 4.4). Power spectra of the response mode at a range of distances (b).

4.3.4 Control

Recent advancements in resolvent analysis have led to significant progress in flow control strategies across various fluid dynamics applications (Luhar et al., 2014; Yeh and Taira, 2019; Jafari et al., 2023). Luhar et al. (2014) extends McKeon and Sharma (2010) resolvent analysis to flow control techniques, particularly focusing on opposition control. This approach decomposes the turbulent pipe flow into highly amplified response modes, assessing the impact of opposition control (Choi et al., 1994) on these modes' amplification characteristics and wall-normal structures. The research finds that slower, wall-attached modes are effectively suppressed, while faster, detached modes are amplified, highlighting a critical balance between mode detection and suppression efficacy. Yeh and Taira (2019) employs resolvent analysis for designing active control techniques in separated flows over airfoils under post-stall conditions. By introducing unsteady thermal actuation, this study pinpoints the optimal frequency and

wavenumber for actuation to maximise energy amplification. Jafari et al. (2023) explores the potential of frequency-tuned surfaces as a passive control strategy, utilising resolvent analysis to investigate surfaces with specific impedances that allow transpiration and/or slip in response to wall dynamics. These surfaces are shown to suppress significant turbulent structures, such as near-wall cycles and large-scale motions, across a wide spectral range. The study reveals that materials designed for near-wall mode suppression and surfaces with shear-driven impedance can lead to overall drag reduction, emphasising the non-unique nature of drag-reducing impedance and the potential for targeting specific frequency bandwidths with periodic material design. Together, these studies underscore the versatility and efficacy of resolvent analysis in developing both active and passive flow control strategies, suitable for various flow conditions and objectives.

One way of controlling the boundary-layer could be to provide opposition control to the wall-normal fluctuations (Luhar et al., 2014). Figure 4.8a shows a zoomed in view of the response mode for the case $f^* = 3$, corresponding the maximum gain (figure 4.4). We can see that the response mode exhibits distinct, periodic spatial structures up until the very inner boundary. Right at the inner boundary, we start to see much higher wavenumber fluctuations as well as high $\vec{u}_n$ regions near the nose and tail.

Figure 4.8b shows the power spectra of the response mode at a range of distances from the body boundary–illustrated by the grey lines in figure 4.8a. For all cut distances there is a clear peak at $k_x = 26$, but as the distance from the body boundary decreases, this low wavenumber peak becomes less distinct from the high wavenumber peaks. At the limit of $n = 0$ the spectra exhibits peaks across the frequency spectra. The peaks at $n = 0$ also fluctuate at the highest amplitude. This suggests that opposition control could be used to suppress response structures near the boundary layer.

It is well documented that surface roughness increases wall-normal fluctuations in turbulent boundary-layers (Grass, 1971). This is due to the roughness elements creating high and low-pressure regions at the peaks and crests of the roughness elements, respectively. Based on the results of this study, we suggest that opposition control through the addition of roughness could be used to suppress the low, or high wavenumber fluctuations, and reduce the unstable response modes, potentially reducing drag. This is a promising avenue for future research.

4.4 Conclusions

We have performed resolvent analysis on the boundary layer of a swimming foil, employing the data-driven technique described by Herrmann et al. (2021) and a coordinate transformation to body coordinates. Our analysis reveals that the swimming foil is sensitive to a range of harmonics, predominantly phase-locked. Moreover, we demonstrate that the resolvent analysis results for the swimming foil differ qualitatively

from those for a stationary foil, indicating that swimming motion significantly influences boundary-layer stability. The forcing modes of the swimming foil display a variety of distinct high- and low-wavenumber structures, while the response modes remain largely invariant to the forcing. Further, our analysis at a distance of $n = 0.005$ from the wall uncovers dominant spatial structures near the boundary layer. Here, the forcing modes exhibit a range of wavenumbers, whereas the response modes consistently show two wavenumbers at $k_x \approx 14$ and $k_x \approx 30$. We also observe that the spatial wavenumbers in the most amplified response mode vary with wall-normal directions, with the highest fluctuations occurring right at the wall and spanning a range of distinct spatial wavenumbers.

The boundary-layer stability's sensitivity to swimming motion and the distinct spatial wavenumbers of the resolvent modes within the boundary layer are significant findings. These suggest that studies investigating roughness with the aim of applying insights to swimming bodies must consider the swimming motion. Furthermore, our research indicates that effective flow control mechanisms could be achieved by actuating the swimmer right at the wall, potentially through the addition of properly tuned surface roughness.

Chapter 5

Surface roughness for increased swimming performance

The content of this chapter contributes to a paper in preparation for submission to the Journal of Fluid Mechanics.

This study investigates the effects of surface roughness on the hydrodynamics of a self-propelled swimming foil, at $Re = 100,000$, focusing on different roughness wavelengths. It reveals that longer wavelengths cause unsteady vortex shedding and a mixed wake, while shorter wavelengths create coherent vortex tubes. Boundary-layer thickness is affected by roughness, particularly towards the tail, with separation dominant at long roughness wavelengths. Roughness also impacts power requirements, with certain roughness scales slightly reducing the required power by affecting vorticity production at the wall. A variable roughness function inspired by sharkskin was tested, showing minimal impact on power compared to a smooth surface, with some regions of improvement. The research indicates that roughness influences are complex and highly dependent on calibration, with smaller scales offering efficiency gains in certain conditions. However, these benefits are not uniform across the swimming cycle and a variable roughness function, inspired by shark skin mechanics could, potentially–given the proper tuning–outperform fixed small-scale roughness. Overall, the study underscores the complex interaction between surface roughness and unsteady fluid dynamics, raising questions about the mechanisms swimmers use to control flow through their skin.

5.1 Introduction

The diversity of inter and intra-species fish scale diversity makes it difficult to pose a universal theory for the hydrodynamic significance of fish scales (Lauder et al., 2016).

Investigating bluegill sunfish (Lepomis macrochirus), Wainwright and Lauder (2016) analysed scale morphology, showing the scales on the gill cover (opercle) are smooth-edged (cycloid), while the scales on the rest of the body have tiny teeth-like projections (ctenoid). As you move towards the underside of the fish, the area covered by these toothed scales (ctenii) gets larger. Near the front spiny part of the dorsal fin and on the gill cover, the scales are smaller, length, and thickness compared to scales found on other parts of the body. Subsequent studies (Wainwright et al., 2017) identify yet more diversity among a wider range of fish species.

Experiments on grass carp (Ctenopharyngodon idellus) scales replicated as bionic surfaces suggested a 3% drag reduction, attributed to a water-trapping mechanism causing flow separation behind the scales, although detailed flow structure analysis was lacking (Wu et al., 2018). Notably, these studies treated scales as isolated units rather than in their natural overlapping arrangement. Muthuramalingam et al. (2019) adopted more realistic, overlapping scales of a European bass (Dicentrarchus labrax), and focused on how the homogenous scale pattern and overlap along the body affect hydrodynamics. They found that the scale array produces regular rows of alternating, streamwise low-speed and high-speed streaks inside the boundary layer close to the surface, with maximum velocity difference of approximately 9%. Low velocity streaks are formed in the central region of the scales whereas the high velocity streaks originated in the overlapping region between the scales. This phenomenon is indicative of the significant influence the arrangement and size of the overlapping scales have on the flow patterns. When the scale height is relatively small compared to the boundary-layer thickness, specifically less than 10%, a total drag reduction is observed. This was corroborated by flow simulations and surface oil-flow visualizations on a physical model of the biomimetic surface in a flow channel, demonstrating a striking correlation in the size and layout of the streaky structures. Given these observations, and in light of recent studies on the impact of micro-roughness in laminar boundary-layer flows, they hypothesised that fish scales could potentially delay the transition to turbulence, thereby further reducing drag. They use $Re = 33,000$, although the bass has a swimming speed that puts it in the range of $Re \approx 4 \times 10^5$.

Muthuramalingam et al. (2020) examines how fish scales affect the transition from laminar to turbulent flow in water. By placing biomimetic scales in overlapping patterns on a flat plate in a laminar water channel, the scales delayed the onset of turbulence by 55% compared to a non-scaled surface. This effect, attributed to the scales generating streamwise streaks, theoretically reduces drag by about 27%. The study suggests potential for using fish scale-inspired designs in laminar flow control to reduce friction drag.

Elasmobranch fishes, such as sharks, skates, and rays, feature a unique skin covered with minute placoid scales or dermal denticles. Embedded in the stratum compactum, a deeper collagenous layer of the skin, these scales vary in size and shape across different

body parts and species (Reif, 1985; Bechert et al., 2000b,c; Ankhelyi et al., 2018). The skins are covered in tiny, tooth-like scales called dermal denticles. Research suggests these denticles play a role in controlling water flow and potentially reducing drag. Initial theories proposed the denticle ridges act as riblets to reduce skin friction. However, experiments found only modest 3% friction reduction with an interlocking shark skin model(Bechert et al., 2000b,c), and 44-50% drag increase when they don't interlock (Boomsma and Sotiropoulos, 2016). Previous research has observed the moveability of these scales, suggesting potential scale bristling at high speeds (Bechert et al., 1985; Lang et al., 2008). The stratum compactum in sharks consists of helically wound collagen fibres, providing structural support and enabling elastic energy storage during swimming (Motta, 1977; Wainwright et al., 1978; Hebrank, 1980). The erectile nature of these scales, believed to be anchored by elastic connective tissue, may be influenced by skin tension changes at higher speeds (Bechert et al., 1985). This alteration in subcutaneous pressure leads to scale erection, particularly in regions with concave curvature during swimming (Wainwright et al., 1978; Lang et al., 2008). Scale bristling could reduce drag on a shark through possible boundary-layer control mechanisms, such as separation control by acting as vortex generators to delay flow separation and reduce pressure drag (Bechert et al., 1985, 2000c,b; Lang et al., 2008). However, these mechanisms remain untested, and the flow structures around the scales are unknown.

In chapter 3, we examined the effects of surface topography on the flow and performance of a Self-Propelled Swimming (SPS) body. We showed that the enstrophy of the flow followed an outer-scaling that reached a peak at $\lambda/2\delta(Re) = 1$. This scaling breaks down when the aperiodicity of the base flow increases. The study highlights a non-linear relationship between roughness and kinematics beyond a simple increase in drag. However, the study was limited to a flat plate, and so the effects of roughness on a body with shape and a flow at a higher Re remain unknown. In chapter 4 we performed stability analysis on a swimming foil and found distinct spatial wave numbers in the response modes. This result suggests that effective opposition control strategies might be found to stabilise the boundary-layer of a swimming foil. However, this study only tells us what the most unstable features are, it does not necessarily translate that these are the most effective actuation modes to increase swimming performance.

In this study, we explore the impact of roughness wavelength on a realistic swimming model. A NACA0012 foil, modified at the leading edge, serves as a proxy for a fish-like body. We examine a range of roughness wavelengths, to assess their influence on the flow structures, boundary-layer development, and power requirements. Furthermore, we introduce a variable roughness function contingent on body curvature, investigating how the bristling of denticles might influence the power demands of a swimming body. This approach aims to elucidate the intricate interplay between surface texture and hydrodynamic efficiency in aquatic locomotion.

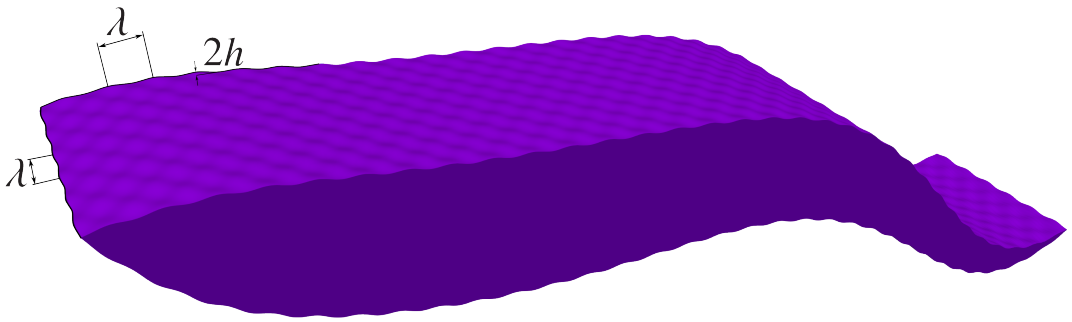

FIGURE 5.1: Parameterisation of the geometry of the NACA foil with egg carton roughness defined by $\lambda = 1/32$.

5.2 Methodology

5.2.1 Geometry

We use the same foil shape employed in section 4 but with the egg-carton roughness function of chapter 3 with amplitude $h = 0.001$. The resulting shape is visualised in figure 5.1, where we show the surface defined by $\lambda = 1/32$. The bump amplitude, and the viscous scales corresponding to $Re = 100,000$ are chosen to mimic a realistic fish of $L \approx 0.1m$ swimming at $U \approx 1ms^{-1}$.

5.2.2 Numerical method

We use the same numerical method, and grid as in chapters 4 & 3. The computational space is illustrated in figure 4.1; we use a spanwise-domain size of $z \in [0, [1/16, 1/4]]$, where the variability in z depends on λ of the foil surface and ensures a minimum distance of 4λ. The total number of grid cells is $N = (4096, 4096, [64, 256])$ totalling $N = 1.7 - 4.3 \times 10^9$ grid cells. We show the domain and grid resolution are sufficient in Appendix C.4.

5.2.3 Kinematics

Figure 5.2.3a illustrates the phase map of the body velocity. Additionally, Figure 5.2.3b depicts the body curvature ($\kappa = \partial^2 y/\partial x^2$), where a positive κ indicates a trough shape

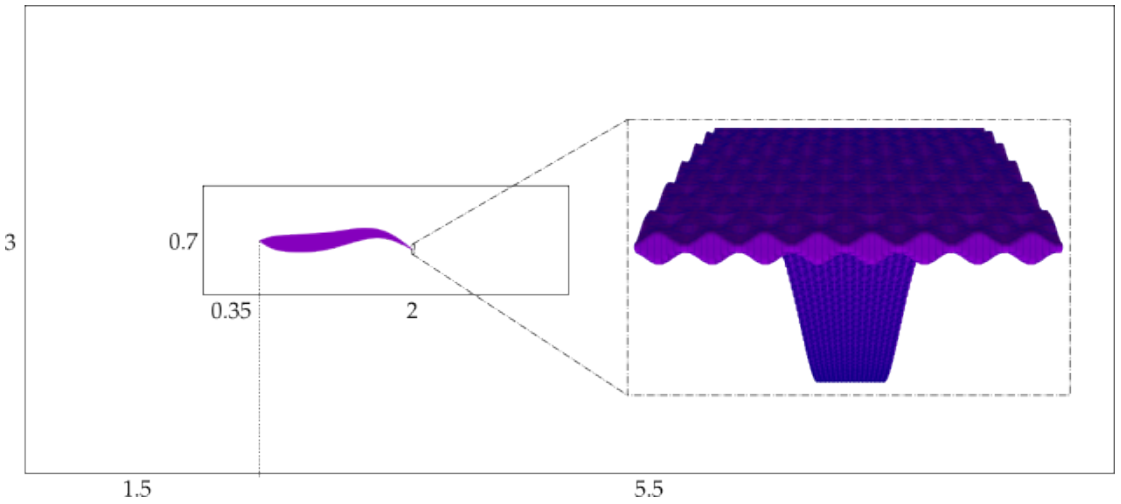

FIGURE 5.2: Illustration of the domain size. The insert shows the grid around the tail.

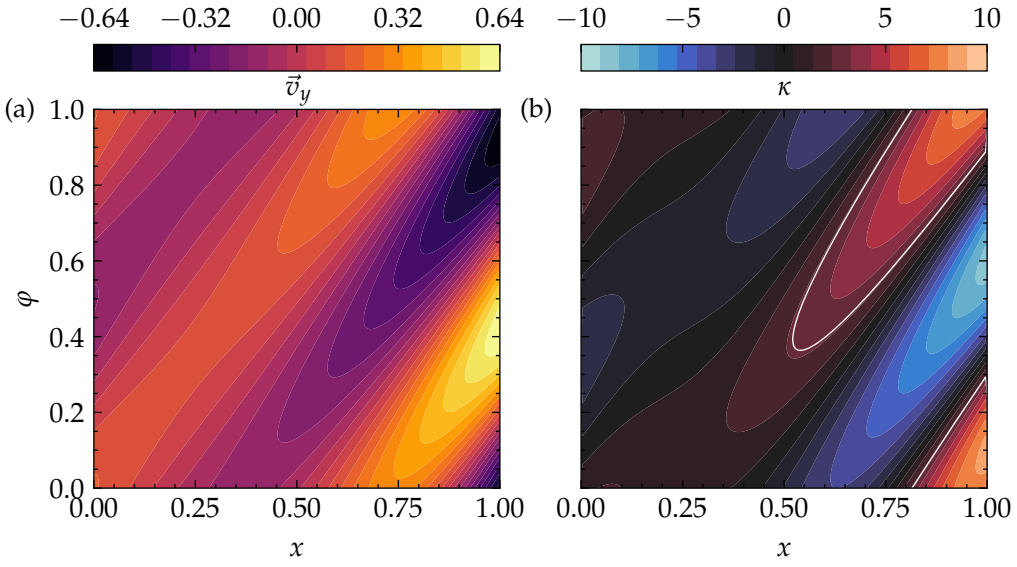

FIGURE 5.3: Some kinematic characteristics. (a) shows the phase map of the body velocity, (b) shows the curvature (κ) of the body. A white line illustrates the contour where $\kappa = 2.5$.

and a negative κ a peak shape in the x, y reference frame. The body velocity and the curvature exhibit strong similarities. They both vary over one period, and increase towards the tail. κ has a phase shift of -0.65π, and so the body reaches its maximum curvature 0.325 before the maximum velocity.

We remain in the self-propelled swimming regime, be fixing $\zeta = 1.42$. Unlike the results of chapter 3 we do not vary ζ with λ. This is because the reduced roughness amplitude means that the foil stays in the SPS regime for all λ tested.

5.3 Results

5.3.1 Flow structures

In the case of the smooth foil, the flow predominantly remains two-dimensional along the body, extending from the nose to the tail as shown in figure 5.4a. This two-dimensionality largely persists in the smooth foil's wake, characterised by vortex tubes forming the wake. However, in the far wake, small, spanwise-perpendicular streaks begin to emerge around some vortices, suggesting instability. Conversely, the flow around the rough foil is more three-dimensional. The flow structures in these scenarios show similarities to those in figure 3.4. Specifically, with long λ roughness, roughness element shedding dominates the flow, leading to unsteady horseshoe vortex generation and a heavily mixed wake. As λ decreases, coherent two-dimensional tubes become more evident in the wake, resembling the flow of the smooth foil. Notably, at $\lambda = 1/128$, the flow primarily features two-dimensional vortex tubes, aligned with and perpendicular to the z-axis. Additionally, this regime shows a significant reduction in unstructured mixing within the wake. These streamwise streaks are reminiscent of the streaks observed in Fransson et al. (2006).

5.3.2 Boundary-layer

In this chapter, we adopt the definition of the boundary-layer thickness (δ) using the $-y\Omega_z$ threshold, following the approach outlined by Uzun and Malik (2021). The phase portraits of δ are then identified by marking the instantaneous profiles in figure 5.5.

The boundary-layer thickness is shown in figure 5.5 for each of the roughness wavelengths. The results show that the profiles on the foils remain consistent across all cases in the range ($0 < x < 0.8$). In the range $0.1 < x < 0.4$, δ increases steadily and the temporal variation of the profiles is minimal, with tight phase portraits. From $0.4 < x < 0.8$, the phase portraits open out, indicating a more significant variation in δ with time. For the cases where $\lambda = 1/0$ and $\lambda = 1/128$, the phase portraits maintain a consistent orbit in the rear region ($0.8 < x < 1$), but for the other cases, areas of separation cause chaotic behaviour in the phase portraits.

The profiles show that the boundary-layer only separates right at the tail of the $\lambda = 1/0$ and $\lambda = 1/128$ cases. The profiles show that the flow remains attached for $0 < x < 0.6$ with no regions of flow reversal. For $\lambda = 1/0$ and $\lambda = 1/128$, the flow remains attached until right at the very tail, where the boundary layer separates, at $x \approx 1$ for $\lambda = 1/0$ and at $x > 0.9$ for $\lambda = 1/128$. For $\lambda = 1/32$, the boundary-layer profiles show regions of inflection at $x = 0.6$, implying that the boundary layer is unsteady; although there is no flow reversal at the boundary, and so it is still attached. This is observed at $x = 0.9$ for $\lambda = 1/16$, and $x = 0.8$ for $\lambda = 1/64$.

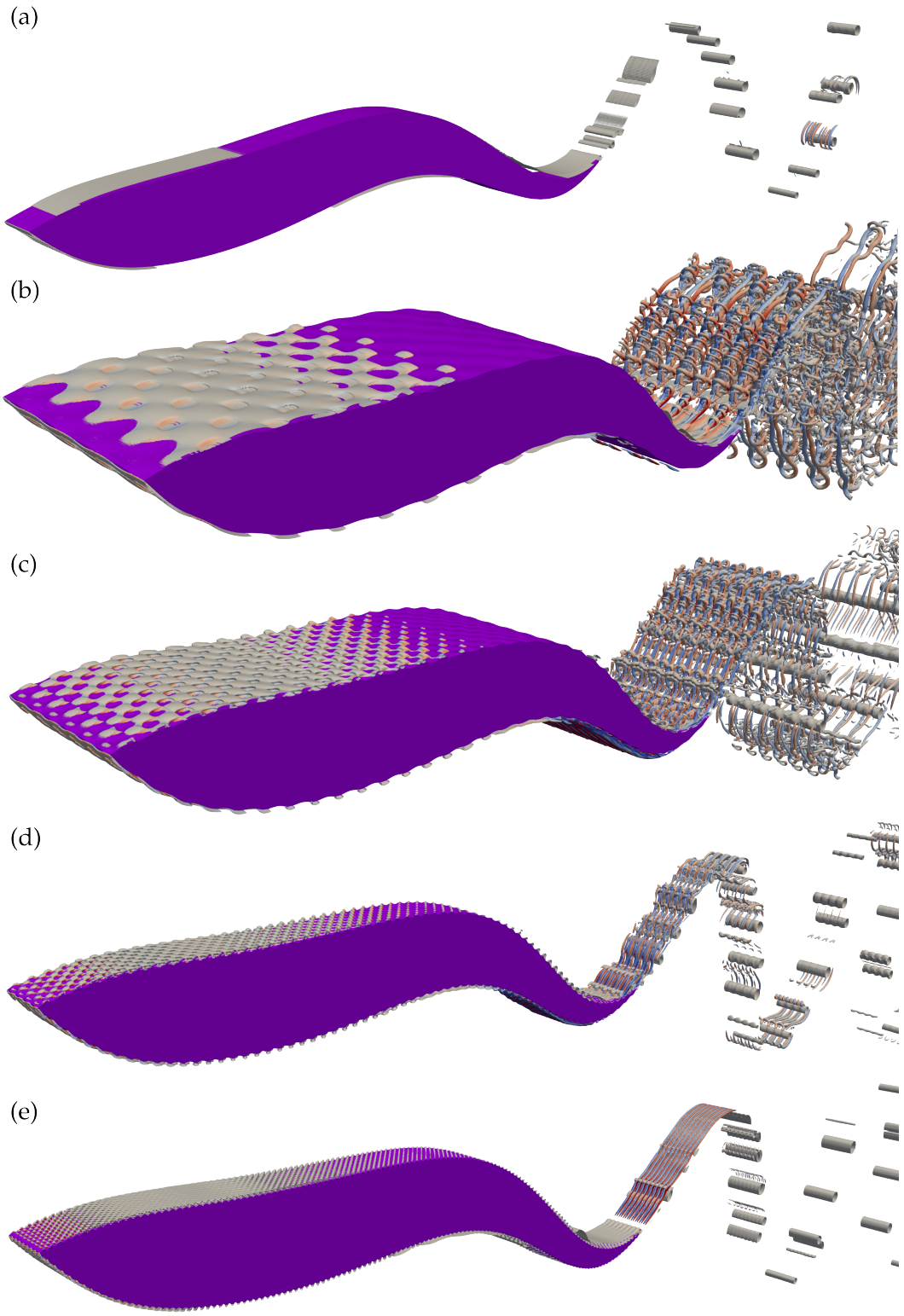

FIGURE 5.4: Flow structures for cases where $\lambda = 1/0, 1/16, 1/32, 1/64$, and $1/128$ (a, b, c, d, e) visualised with a Q-contour of $Q = 1 \times 10^{-5}$. All plots are coloured by $\omega_y \in [-0.025, 0.025]$.

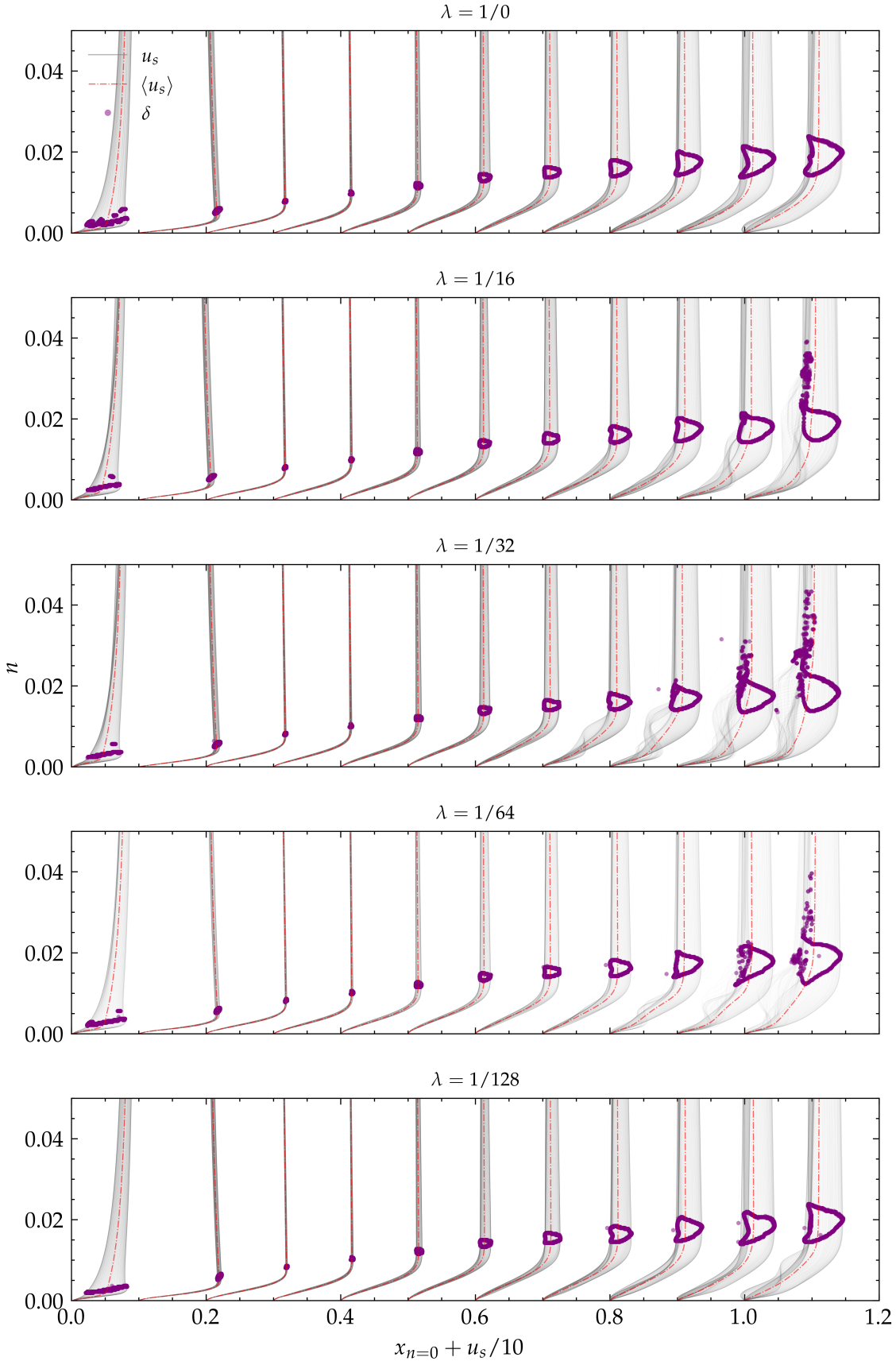

FIGURE 5.5: The boundary-layer profiles, and identified boundary-layer thickness (δ) for cases where $\lambda = 1/0, \lambda = 1/16, 1/32, 1/64$, and $1/128$. The grey lines indicate the profile instances, the dashed red line indicates the mean profile, and the purple markers represents the identification of δ using the $-y\Omega_z$ threshold method.

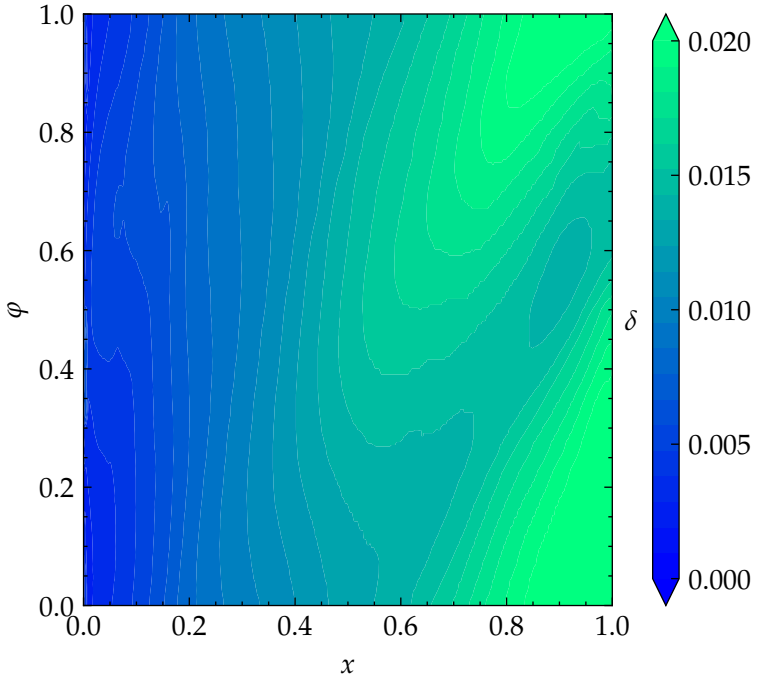

FIGURE 5.6: Phase map for the boundary-layer thickness of the smooth foil.

The thickness of the boundary layer, denoted as δ, for the base flow is depicted in figure 5.6. For the range of $0.1 < x < 0.5$, the variation in δ is minimal across different cycle times. In contrast, for $x > 0.5$, we observe a significant variation in δ with cycle time. Notably, this variation in δ for $x > 0.5$ aligns closely with the phase times of κ, albeit with a minor phase shift of -0.135π.

We plot the difference between the smooth and rough boundary layers in figure 5.7. The regions in purple show where the roughness increases the boundary-layer thickness, while the regions in orange show where the roughness has decreased δ. For $0.15 < x < 0.5$, δ is offset by a relatively constant value. This offset depends on λ, with the average being $0.17h, 0.25h, 0.36h$, and $0.49h$. For $x > 0.5$, the boundary-layer dynamics are dominated by separation for $\lambda = 1/16, 1/32$, and $1/64$. However, for $\lambda = 1/128$, the boundary layer remains attached throughout the cycle.

5.3.3 Enstrophy

Figure 5.8 shows the enstrophy for the smooth and rough cases. The enstrophy for the $1/16$ and the $1/64$ cases are close in value, however the RMS is larger for $1/16$ case, and they are out of phase, supporting the discussion in section 5.3.1; which pointed out the qualitative flow structures between the cases. The enstrophy is highest for the case where $\lambda = 1/32$. This is in line with findings from chapter 4, which found that one of the most sensitive spatial wavenumbers was $k_x \approx 30$, which corresponds to upwelling and downwelling effects in the response modes at this frequency. The case where $\lambda = 1/128$

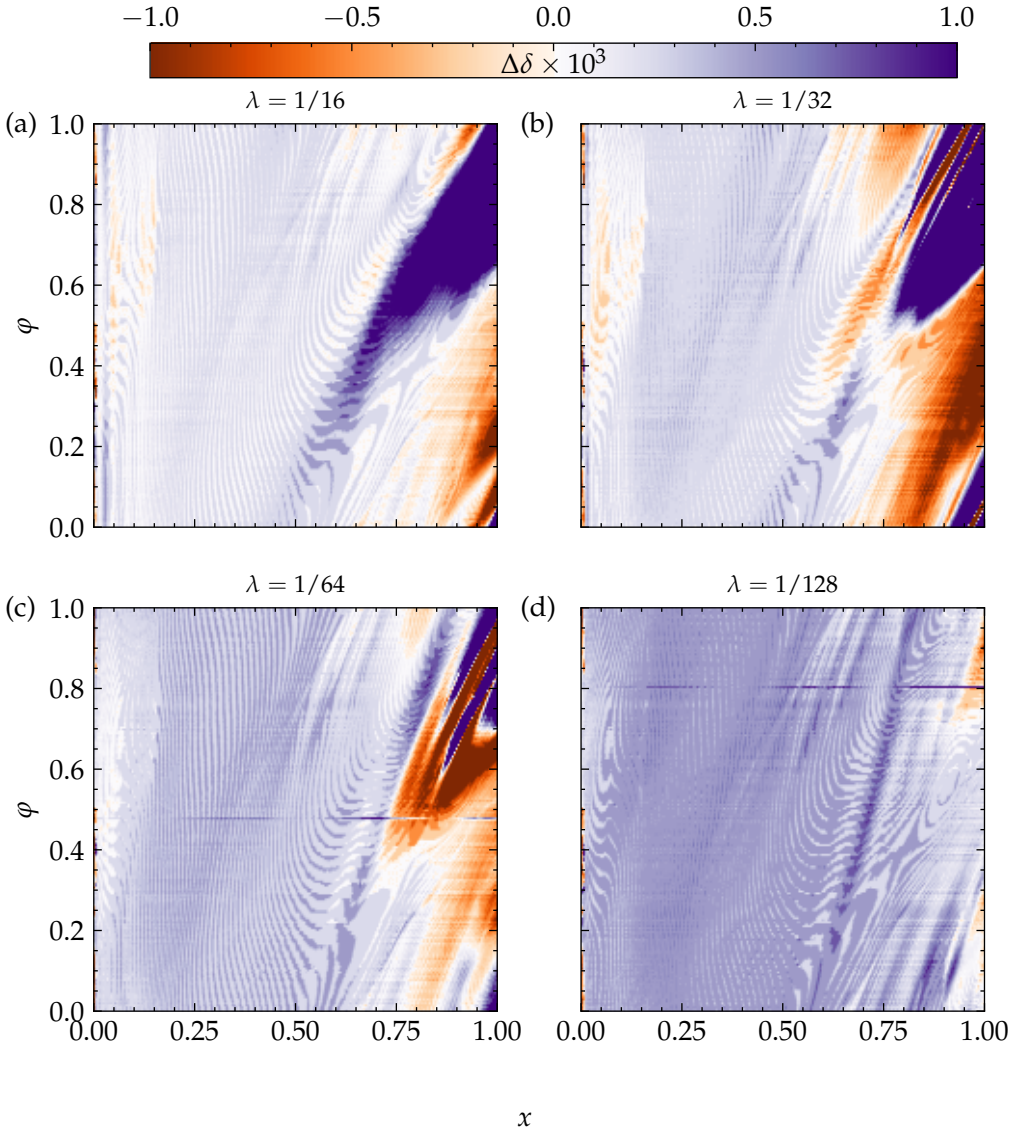

FIGURE 5.7: Boundary-layer difference between the smooth and the rough cases for $\lambda = 1/16$ (a), $1/32$ (b), $1/64$ (c), and $1/128$ (d).

has the lowest enstrophy, comparable to the smooth foil. $\lambda = 1/128$ also has a lower minimum than the smooth case, suggesting that the roughness has a stabilising effect on the flow.

5.3.4 Power

During SPS, the power (C_P) requirement directly measures the swimmer's efficiency, as efficiency becomes incalculable when $C_T = 0$. We compare this to the smooth surface to ascertain whether roughness impacts the swimmer positively or negatively. The cases with $\lambda = 1/16$ and $1/32$ show a consistent increase in required power, especially around the power recovery phase.

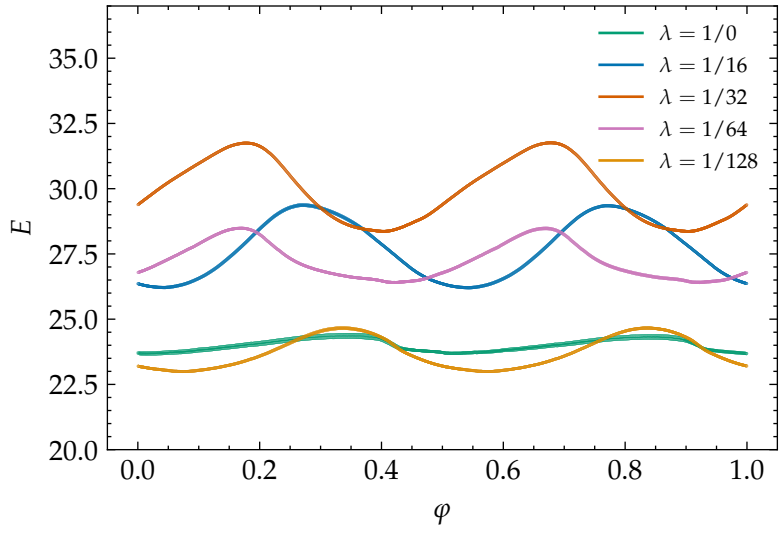

FIGURE 5.8: Enstrophy for cases where $\lambda = 1/0, 1/16, 1/32, 1/64$, and $1/128$.

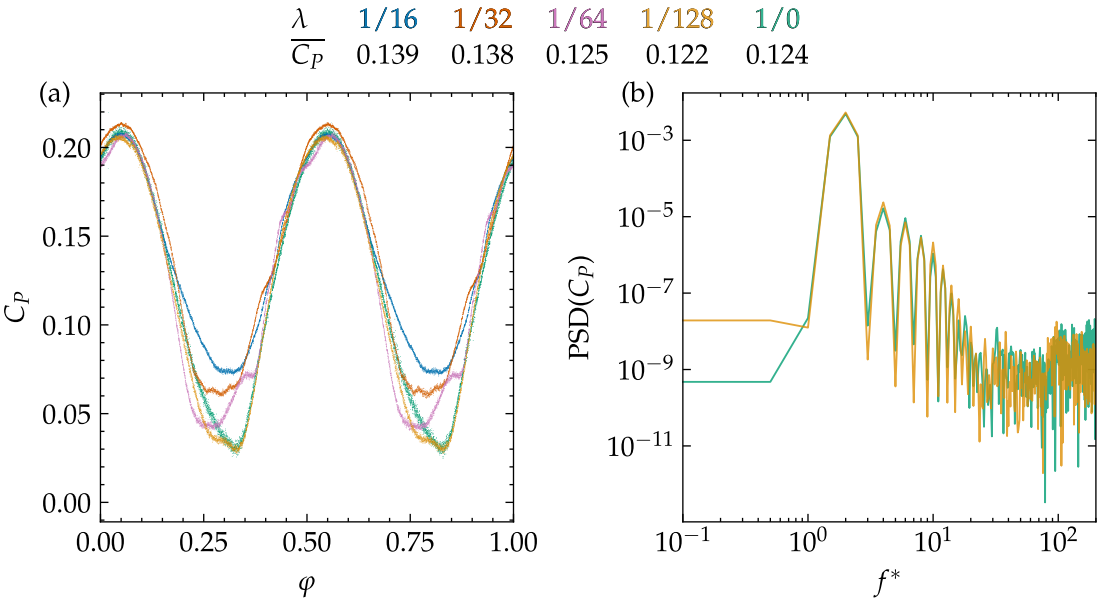

FIGURE 5.9: Power (a) and PSD (b) for cases where $\lambda = 1/16, 1/128$, and $1/0$. The PSD is calculated using Welch's method with a Hanning window and 50% overlap. The legend and mean C_P values are shown in the title.

The rough surfaces, defined by $\lambda = 1/64$ and $1/128$, show instances where less power is consistently required, as compared to the smooth swimmer. Specifically, the $\lambda = 1/128$ case reduces the total power requirement by 2%, although this is within modelling error. Figure 5.9 illustrates C_P varying with φ over four cycles, with data points plotted as small markers to indicate minimal cycle-to-cycle variability across six cycles. In the $\lambda = 1/64$ scenario, there's a steeper decrease in power during the ramp down to the power recovery trough compared to the smooth case. However, its minimum is not as low as the smooth case, and the power recovery period is shorter, leading to a marginally higher $\overline{C_P}$. In contrast, the $\lambda = 1/128$ scenario follows a similar trend to the $\lambda = 1/64$

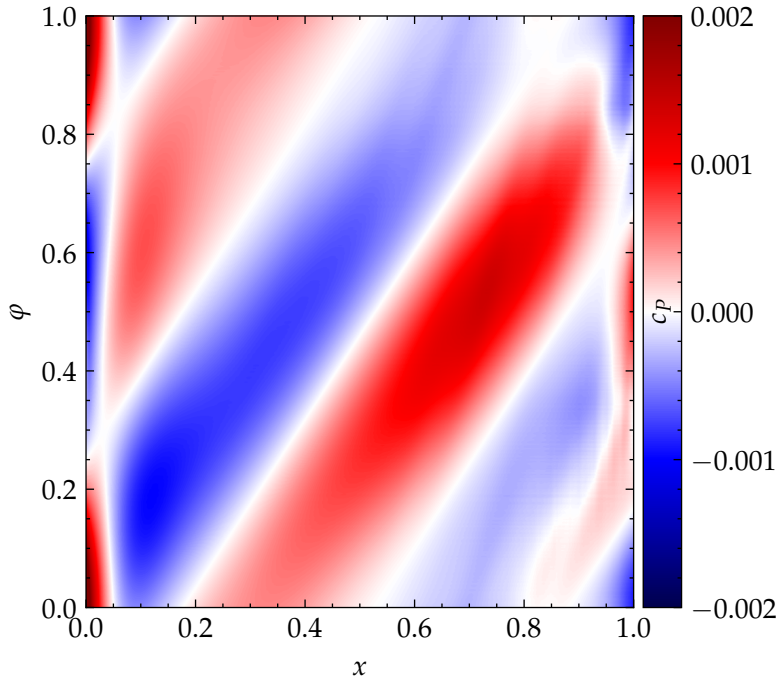

FIGURE 5.10: The contributions to C_P for the top half of the smooth foil.

case but with an extended, lower power recovery phase, matching the smooth case at the minima, resulting in the reduction in $\overline{C_P}$ by 2%. The FFT in Figure 5.9b shows that the spectral composition of the signals from the smooth and $\lambda = 1/128$ cases are largely identical, with strongly phase-locked dynamics. The primary differences appear at higher frequencies, though distinguishing the spectra is challenging due to significant noise at these frequencies.

We can decompose the integral by assessing c_P's temporal and spatial locality. Figure 5.10 displays the phase map of spanwise-averaged c_P on the foil's upper half. We can divide the c_P distribution into regions closely correlating with the prescribed kinematics illustrated in figure 5.2.3. The positive (red) and negative (blue) power contributions propagate along the foil, following the gradient that corresponds to the wavespeed of locomotion (ζ). The power recovery stroke comprises two phase regions, $0.2 < \varphi < 0.45$ and $0.7 < \varphi < 0.95$. The first region aligns with a downward motion in the mid-body and an upward motion at the tail, while the second region represents the inverse.

We plot the difference in power between the rough and smooth cases ($\Delta c_P = c_{P,rough} - c_{P,smooth}$) to discern where the rough surface is beneficial. Figure 5.11 shows Δc_P for the top half of the foil, where green regions indicate the rough surface's higher efficiency compared to the smooth, and red regions highlight where the smooth surface is more efficient. The insets display the integrals in both x and φ directions with the black dotted line denoting the average over 4 cycles. We refer to the integral in the x direction as C_P, and in the φ direction as $\overline{c_P}$.

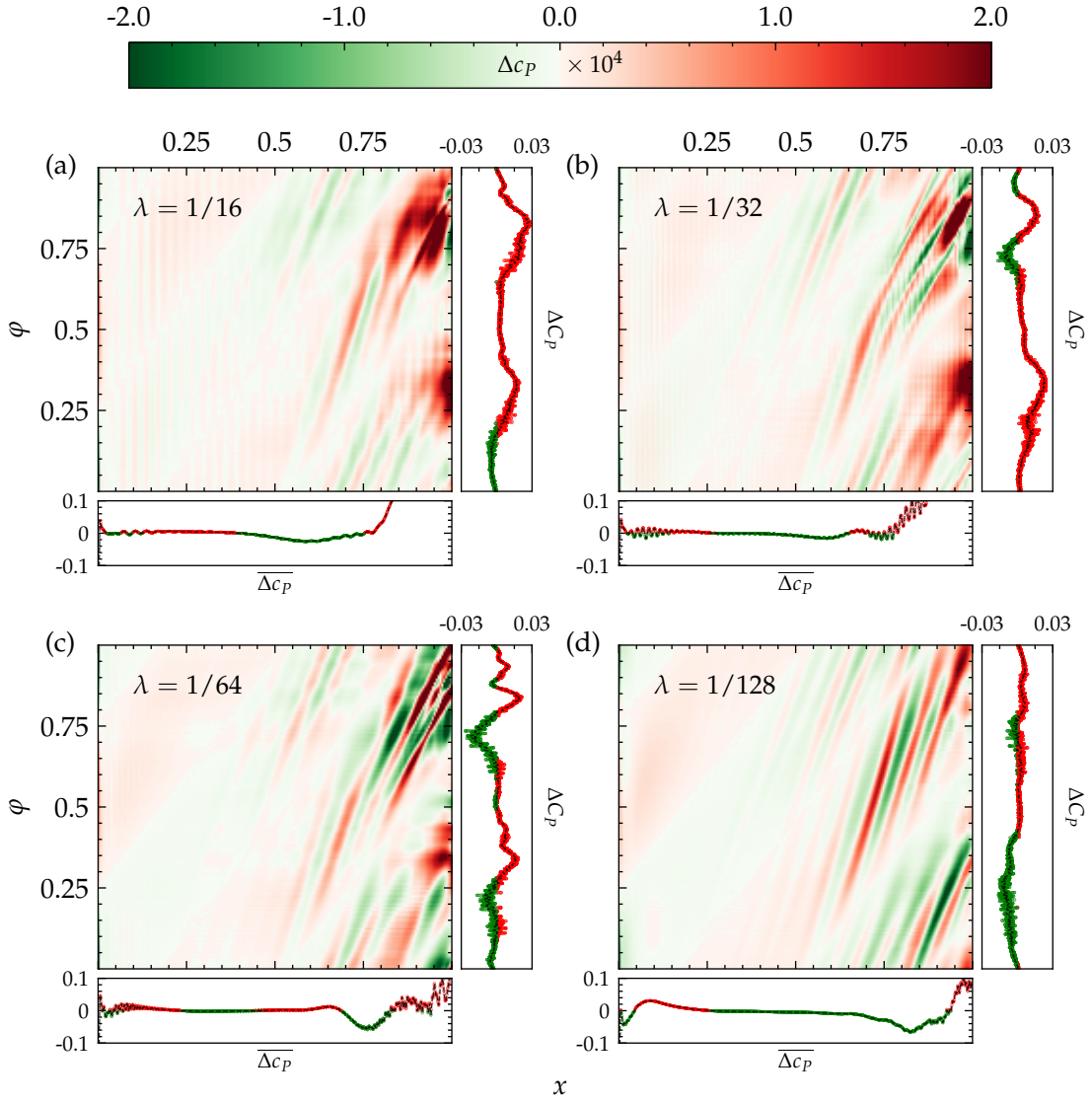

FIGURE 5.11: Smooth-rough difference in c_P depending on body position and cycle time, averaged over eight cycles, for the top half of the foil, where (a), (b), (c), and (d) are for $\lambda = 1/16$, 32, $1/64$, and $1/128$. The horizontal and vertical axis are the averages in the φ and x directions, respectively.

For $\lambda = 1/16$ and $1/32$, the roughness impacts the power of the first two-thirds of the foil minimally. However, at half the roughness wavelength, we observe fluctuations. These are small for $\lambda = 1/16$ but become more pronounced for $\lambda = 1/32$ and $\lambda = 1/64$. Specifically, for $\lambda = 1/16$ figure 5.11a shows that roughness leads to a reduction in $\overline{\Delta c_P}$ in the region where $0.4 < x < 0.75$. This reduction mainly occurs during cycle times $0.75 < \varphi < 1$. Referring to figure 5.2.3, this region correlates with negative curvature and an increasing body velocity from zero. Furthermore, for $\lambda = 1/16$, another significant reduction in ΔC_P appears for $0 < \varphi 0.15 <$. This reduction primarily affects the region where $0.7 < x < 1$. The structure of this reduction, with $k_x \approx 16$, might suggest a correlation with the roughness wavelength.

Similarly to the situation with $\lambda = 1/16$, a region with reduced $\overline{c_P}$ is noted for $\lambda = 1/32$, though this region extends from $0.25 < x < 0.65$. For $\lambda = 1/64$, this region of reduced $\overline{c_P}$ is also present but covers a more limited range, specifically $0.25 < x < 0.45$. Such observations suggest a scaling behaviour of the boundary layer, which is linearly varying within these ranges, as illustrated in figure 5.6.

The surface characterised by $\lambda = 1/128$ shows consistent regions of power reduction (figure 5.11d). For $0.25 < x < 0.9$, both $\overline{c_P}$ and C_P in the temporal region of $0 < \varphi < 0.4$ are lower compared to the smooth case. A notable fluctuation in the difference is observed at $k_x \approx 20$ within the $0 < \varphi < 0.4$ range. Although this fluctuation also occurs in the other cases, it is less pronounced there.

5.3.5 Inner boundary layer

To elucidate the structures influencing the power difference, we examine snapshots of the vorticity field during the power recovery stroke, as depicted in figure 5.12. We employ the spanwise and normal body coordinates (s, n) to represent the flow fields. This approach enables us to establish a stationary reference frame, accommodating the movement of the foil. Utilising this framework, we can closely observe the boundary layer and discern the flow structures with greater detail. Across different cases, the flow structures exhibit similarities, characterised by a distinct low-vorticity region followed by a high-vorticity region that traverses the foil over time. We have selected $\varphi = 0.2, 0.24, 0.3$, and 0.35 for closer inspection, as these phases manifest marked differences in both figure 5.11 and figure 5.11.

The rough surfaces reduce the power by offsetting the vorticity production at the wall, restricting it to the top of the roughness elements. For $\lambda = 1/64$, the region where $0.7 < x < 1$ and $\varphi = 0.2$ significantly reduces the power compared to the smooth case (figure 5.11c). Correlating this with the flow structures in figure 5.12 reveals that the mechanism stems from a combination of the reduced vorticity production at the surface in $0.6 < x < 0.8$ as well as a reduction and a vertical offset of the high vorticity region at $0.85 < x < 0.95$. This mechanism is similar for $\lambda = 1/128$, however, the reduction in vorticity production is more pronounced, and the offset of the high vorticity region is more significant and is supplemented with the bifurcation of the high vorticity region. This is consistent with the more pronounced reduction in power for $\lambda = 1/128$ for $0.875 < x < 0.9$ at $\varphi = 0.2$ (figure 5.11d).

As φ increases, the low and high vorticity regions progress down the body. For $\varphi = 0.25$, figure 5.9a shows that $\lambda = 1/64$ reaches its lowest C_P, while the smooth, and $\lambda = 1/128$ cases are still on a downward trajectory. This is consistent with the flow structures, as the high vorticity region has increased in size, and shifted closer to the body for $\lambda = 1/64$, but not for $\lambda = 1/128$. For $\varphi = 0.3$ and 0.35, the smooth and $\lambda = 1/128$ cases converge

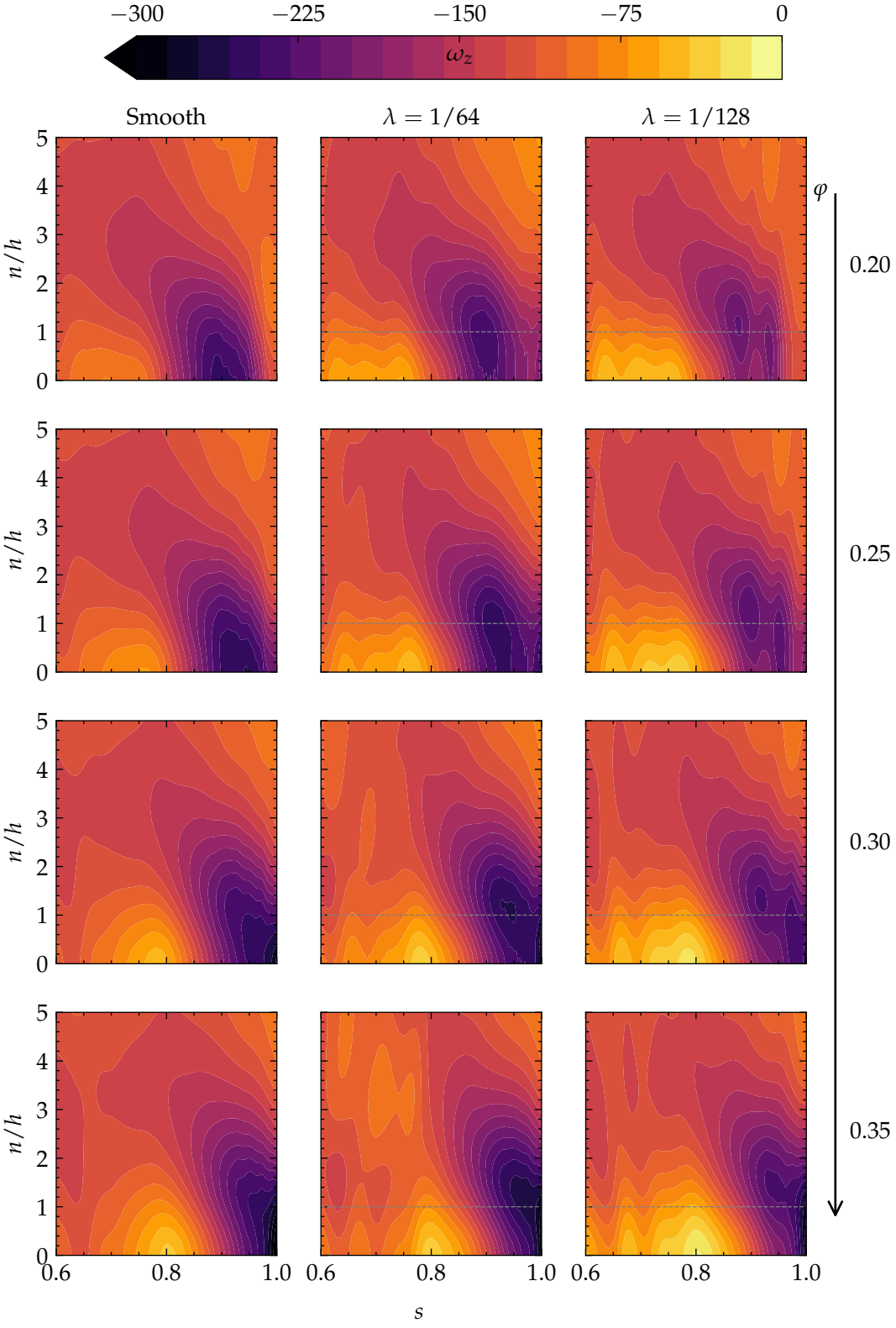

FIGURE 5.12: Vorticity on the tail in terms of body coordinates (n, s) at cycle times $\varphi = 0.2, 0.25, 0.3$, and 0.35. The grey dashed line represents the top of the rough surface.

at the power recovery minimum in figure 5.9a, and figure 5.11d suggests this results from a balance between beneficial shifts in some regions but not in others.

By comparison to the smooth, the addition of $\lambda = 1/64$ roughness in the $\varphi = 0.3$ and 0.35 range confirms its detrimental effect on power as the vorticity structure is equivalent; the rough surface significantly increases the power on the surface (figures 5.9a, and 5.11c). This is most evident for $\varphi = 0.35$, where the smooth and $\lambda = 1/64$ cases have almost identical vorticity contours (figure 5.12), yet figure 5.11c shows a significant increase in the power on the surface. Conversely, there is a slight reduction when $\varphi = 0.3$ and $x = 0.775$, consistent with the further reduced vorticity in the low vorticity region.

The bifurcation of the high vorticity region in $\lambda = 1/128$ leads to further displacement of the vortex cores. This displacement aligns with the δ shift observed in figure 5.7d, highlighting the intricate relationship between surface roughness, vorticity distribution, and power generation. This correlation underscores the complexity of flow dynamics over textured surfaces, where subtle modifications in surface characteristics can significantly alter the flow behaviour and energy efficiency.

5.3.6 Variable-height roughness function

We have established that the roughness provides benefit for the foil when $\lambda = 1/128$, at various points on the body, and in the cycle. Lang et al. (2008) found that the denticles of a shark erect when there is subcutaneous pressure. Thus, this bristling actuates at concave regions on the shark (Wainwright et al., 1978; Lang et al., 2008). To test whether this bristling could be beneficial for the swimming performance, we introduce a variable roughness function, where the amplitude of the roughness is dependent on the curvature of the body. We define the function as

$$h_{variable}(x, \varphi) = h \min\left(2.5, \max(0, \kappa)\right) / 2.5 \tag{5.1}$$

where the value 2.5 is chosen as it represents a contour where $h_{variable} = h$ at the mid-body, so as not to disproportionally target the tail of the foil. We plot a white contour on figure 5.2.3b to illustrate the contour where the roughness function is clipped so that $h_{variable} = h$. Thus, we replace h in equation 2.24 with $h_{variable}$.

Figure 5.3.6 illustrates the difference in pressure coefficients, $\Delta c_{P,\text{variable}} = c_{P,\text{static}} - c_{P,\text{variable}}$, where $c_{P,\text{static}}$ represents the smooth ($\lambda = 1/0$) or the 1/128 surface, as specified. The variable roughness function minimally influences the power relative to the smooth case, exhibiting regions of both slight improvement and deterioration (see figure 5.3.6a). Notably, the variable roughness function shares similar characteristics

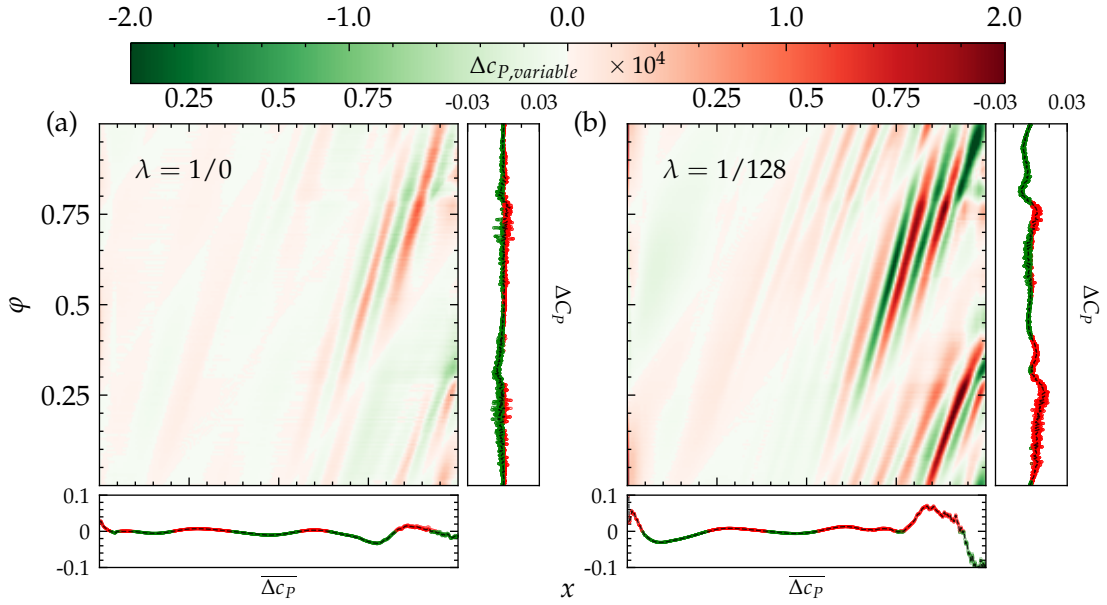

FIGURE 5.13: Difference in c_P between, (a), the variable roughness function and the smooth foil, and, (b), the variable roughness function and the $\lambda = 1/128$ roughness function.

with $\lambda = 1/128$, as shown in figure 5.11d, with fluctuating streaks between $0.5 < x < 1$, aligned with the outer flow velocity.

Overall, the variable roughness function generally underperforms compared to the $\lambda = 1/128$ case, though it does achieve local power reductions, particularly in the range $0.775 < \varphi < 1$. The difference between the variable roughness and $\lambda = 1/128$ functions is evident(figure 5.3.6b). The more pronounced fluctuating streaks between $0.5 < x < 1$–oriented with the outer flow–suggest a phase shift favouring the variable roughness function. This phase shift is advantageous in the $0.775 < \varphi < 1$ region, where the variable roughness function surpasses the $\lambda = 1/128$ performance. Conversely, in the $0 < \varphi < 0.4$ region, the $\lambda = 1/128$ function significantly outperforms the variable roughness function. These observations imply that while the variable roughness function is not an adequate substitute for the $\lambda = 1/128$ function, potential improvements through fine-tuning, possibly analogous to 100 million years of evolutionary adaptation, could substantially reduce drag in a swimming body.

5.4 Conclusion

This chapter has methodically explored the impact of surface roughness on a self-propelled swimming foil, examining a range of roughness wavelengths and their effects on flow structures, boundary-layer evolution, and power demands. We found that the flow structures are highly dependent on the roughness wavelength, with longer wavelengths leading to unsteady vortex shedding and a heavily mixed wake.

Conversely, shorter wavelengths produce two coherent vortex tubes modes; one aligned with the kinematic wake–rotating around the z-direction and similar to the smooth foil–and one perpendicular. The boundary-layer thickness is offset by a constant value for $0.15 < x < 0.5$, with the offset increasing with λ. For $x > 0.5$, the boundary-layer dynamics are dominated by separation for $\lambda = 1/16, 1/32$, and $1/64$. However, for $\lambda = 1/128$, the boundary layer remains attached throughout the cycle. The roughness reduces the power requirement by offsetting the vorticity production at the wall, restricting it to the top of the roughness elements. For $\lambda = 1/64$, the region where $0.7 < x < 1$ and $\varphi = 0.2$ significantly reduces the power compared to the smooth case. Correlating this with the flow structures reveals that the mechanism stems from a combination of the reduced vorticity production under the surface in $0.6 < x < 0.8$ as well as a reduction and a vertical offset of the high vorticity region at $0.85 < x < 0.95$. This mechanism is similar for $\lambda = 1/128$, however, the reduction in vorticity production is more pronounced, and the offset of the high vorticity region is more significant and is supplemented with the bifurcation of the high vorticity region. This displacement aligns with the δ shift observed in figure 5.7d, highlighting the intricate relationship between surface roughness, vorticity distribution, and power generation. This correlation underscores the complexity of flow dynamics over textured surfaces, where subtle modifications in surface characteristics can significantly alter the flow behaviour and energy efficiency.

Further, we have tested a variable roughness function, meant to mimic the bristling effect of sharkskin (Lang et al., 2008). We found that our function minimally influences the power relative to the smooth case, exhibiting regions of both slight improvement and deterioration. Notably, the variable roughness function shares similar characteristics with $\lambda = 1/128$, as shown in figure 5.11d, with fluctuating streaks between $0.5 < x < 1$, aligned with the outer flow velocity. Overall, the variable roughness function generally underperforms compared to the $\lambda = 1/128$ case, though it does achieve local power reductions, particularly in the range $0.775 < \varphi < 1$. The more pronounced fluctuating streaks between $0.5 < x < 1$–oriented with the outer flow–suggest a phase shift favouring the variable roughness function.

The findings indicate that the influence of roughness is nuanced and highly dependent on precise calibration. Longer roughness wavelengths tend to enhance three-dimensionality and the generation of horseshoe vortices, leading to increased surface pressure. Conversely, small-scale roughness, when optimally tuned, offers modest efficiency gains. This is primarily due to the confinement of vortex production to the roughness crests, which shifts vorticity away from the surface and reduces power requirements in certain areas.

However, these benefits are not consistent throughout the entire swimming cycle, with negative impacts observed during other phases. An attempt to implement variable roughness modulated by body curvature, inspired by the hypothesised shark skin mechanics suggested by Lang et al. (2008), did not yield efficiency gains compared to

fixed small-scale roughness. This finding underscores the complex spatial and temporal interplay between surface textures and unsteady flows.

In summary, the results of this research highlight the hydrodynamic complexities inherent in surface roughness on self-propelled swimming bodies. While modest improvements are achievable with precise roughness tuning, even small deviations from optimal conditions can significantly impair performance. This underscores the inherent challenges in translating bioinspired designs from static simulations to dynamic applications.

Chapter 6

Conclusions

This thesis has explored the complex interplay between surface roughness and self-propelled aquatic locomotion. Through methodical numerical simulations, we have examined the influence of roughness on the evolution of flow structures, boundary-layer dynamics, and power requirements of swimming bodies.

Our methodology centred on an in-house large eddy simulation code validated for flows over rough, moving boundaries. This enabled us to simulate a range of test cases with egg-carton roughness of varying roughness wavelengths, different Re, and two different body shapes. The results were analysed using a range of novel techniques, including resolvent analysis. The combination of simulations and analysis techniques has enabled us to explore the complex interactions between surface roughness and self-propelled swimming with specific insights from the following studies:

6.1 A systematic investigation into the effect of roughness on self-propelled swimming plates

As the roughness wavelength is decreased, the undulation wave speed must be increased to overcome the additional drag from the roughness and maintain SPS. The extra wave speed raises the power required to maintain SPS, making the swimmer less efficient. We find that all but the longest roughness wavelengths reduce the required swimming power and the unsteady amplitude of the forces when compared to a smooth plate undergoing identical kinematics. Additionally, roughness can enhance flow enstrophy compared to the smooth cases without a corresponding spike in forces; this suggests that the increased mixing is not due to increased vorticity production at the wall. Instead, the enstrophy is found to peak when the roughness wavelength is approximately twice

the boundary-layer thickness over the *Re* range, indicating the roughness induces large-scale secondary flow structures. This study reveals the nonlinear interaction between roughness and kinematics beyond a simple increase or decrease in drag.

6.2 Resolvent analysis of a swimming foil

The swimming foil's boundary layer is sensitive to a spectrum of harmonics, mainly phase-locked, differing significantly from a stationary foil. The analysis reveals varied high and low-wavenumber structures in the swimming foil's forcing modes, while its response modes show frequency invariance. The resolvent mode spectra uncover dominant spatial structures near the boundary layer, with forcing modes displaying diverse wavenumbers and response modes consistent. Finally, this study shows that the most sensitive region of the flow is right next to the body, exhibiting large fluctuations, at a range of distinct spatial wavenumbers. These findings emphasise the impact of swimming motion on boundary-layer stability and suggest the potential of opposition flow control, to damp the coherent response modes through properly tuned surface roughness.

6.3 Surface roughness for increased swimming performance

On the swimming foil, longer wavelengths cause unsteady vortex shedding and a mixed wake, while shorter wavelengths create two, coherent, perpendicular vortex tube structures. Boundary-layer thickness is affected by roughness, particularly towards the tail, with separation dominant at long roughness wavelengths. Roughness also impacts power requirements, with certain roughness scales minimally reducing the required power by affecting vorticity production at the wall. A variable roughness function inspired by sharkskin was tested, showing minimal impact on power compared to a smooth surface, but with some regions of improvement. The research indicates that roughness influences are complex and highly dependent on calibration, with smaller scales offering efficiency gains in certain conditions. However, these benefits are not uniform across the swimming cycle and a variable roughness function, inspired by shark skin mechanics could, potentially–given the proper tuning–outperform fixed small-scale roughness. Overall, the study underscores the complex interaction between surface roughness and unsteady fluid dynamics, raising questions about the mechanisms swimmers use to control flow through their surface.

6.4 General remarks

This thesis provides insights into the complex and nonlinear interaction between roughness and kinematics in self-propelled swimmers, revealing that both roughness wavelength and kinematics significantly influence the flow structures and power requirements. Our findings indicate that the stability of the boundary layer is fundamentally affected by the swimming motion, particularly in the region closest to the body. Moreover, while surface roughness is shown to enhance swimming performance, the benefits are not uniformly distributed across the swimming cycle. This suggests the potential for using a variable roughness function to optimise performance, though further research is necessary to fine-tune this approach for maximal effectiveness.

Appendix A

Flat plate forces

Table A.1, A.2, and A.3 show $\zeta, \overline{C_T}, \overline{C_P}$ for the rough, and kinematically equivalent smooth simulations. Figure 3.6 is the graphical representation but, for ease of comparison, we have also tabulated the data.

λ	ζ	$\overline{C_T}$	$\overline{C_{Ts}}$	$\overline{C_P}$	$\overline{C_{Ps}}$
1/0	1.06	−0.007	−0.007	0.088	0.088
1/4	1.11	−0.003	−0.000	0.103	0.102
1/8	1.14	−0.003	0.004	0.111	0.110
1/12	1.22	0.002	0.015	0.135	0.135
1/16	1.26	0.000	0.020	0.148	0.148
1/20	1.29	−0.003	0.023	0.156	0.156
1/24	1.34	−0.002	0.029	0.172	0.173
1/28	1.37	−0.002	0.031	0.179	0.180
1/32	1.45	−0.003	0.039	0.204	0.205
1/36	1.51	−0.000	0.045	0.221	0.224
1/40	1.54	−0.004	0.048	0.229	0.234
1/44	1.76	−0.001	0.064	0.287	0.299
1/48	1.96	0.000	0.074	0.340	0.355
1/52	2.26	−0.003	0.084	0.396	0.417

TABLE A.1: Tabulated data of simulations at $Re = 6,000$ with the input roughness defined by λ and corresponding ζ that results in self-propelled swimming. The table also reports the values for $\overline{C_T}, \overline{C_P}$ where the subscript $(\cdot)_s$ refers to a smooth plate for comparison.

λ	ζ	$\overline{C_T}$	$\overline{C_{Ts}}$	$\overline{C_P}$	$\overline{C_{Ps}}$
1/0	1.06	−0.006	−0.006	0.095	0.095
1/4	1.11	−0.003	−0.001	0.107	0.107
1/8	1.14	−0.003	0.001	0.116	0.115
1/12	1.22	0.002	0.015	0.140	0.140
1/16	1.26	0.001	0.020	0.152	0.153
1/20	1.29	−0.002	0.024	0.160	0.162
1/24	1.34	−0.002	0.030	0.177	0.178
1/28	1.37	−0.000	0.033	0.185	0.185
1/32	1.45	−0.002	0.041	0.210	0.210
1/36	1.51	0.000	0.047	0.225	0.229
1/40	1.54	−0.003	0.050	0.233	0.239
1/44	1.76	−0.001	0.066	0.296	0.306
1/48	1.96	0.000	0.075	0.354	0.361
1/52	2.26	−0.001	0.087	0.415	0.444

TABLE A.2: Tabulated data of simulations at $Re = 12,000$ with the input roughness defined by λ and corresponding ζ that results in self-propelled swimming. The table also reports the values for $\overline{C_T}, \overline{C_P}$ where the subscript $(\cdot)_s$ refers to a smooth plate for comparison.

λ	ζ	$\overline{C_T}$	$\overline{C_{Ts}}$	$\overline{C_P}$	$\overline{C_{Ps}}$
1/0	1.06	−0.011	−0.011	0.097	0.097
1/4	1.11	−0.003	−0.001	0.109	0.111
1/8	1.14	−0.002	0.000	0.117	0.119
1/12	1.22	0.002	0.015	0.141	0.147
1/16	1.26	0.000	0.019	0.153	0.161
1/20	1.29	−0.004	0.021	0.161	0.169
1/24	1.34	−0.004	0.026	0.176	0.183
1/28	1.37	−0.003	0.030	0.184	0.191
1/32	1.45	−0.005	0.040	0.212	0.217
1/36	1.51	−0.000	0.046	0.229	0.236
1/40	1.54	−0.004	0.049	0.238	0.246
1/44	1.76	−0.001	0.067	0.302	0.310
1/48	1.96	0.002	0.077	0.361	0.365
1/52	2.26	0.001	0.088	0.420	0.451

TABLE A.3: Tabulated data of simulations at $Re = 24,000$ with the input roughness defined by λ and corresponding ζ that results in self-propelled swimming. The table also reports the values for $\overline{C_T}, \overline{C_P}$ where the subscript $(\cdot)_s$ refers to a smooth plate for comparison.

Appendix B

Forward-backward DMD

In general, DMD determines the spectral quantity of the best fit linear operator (A) that relates two snapshot matrices in time

$$Y = AX\,, \tag{B.1}$$

where X and Y are measurements of the system at time t and $t + \Delta t$. Mathematically we can solve A such that

$$A = YX^{\dagger}\,, \tag{B.2}$$

where the superscript $()^{\dagger}$ refers to the pseudo inverse. Because A is an approximation of the Koopman operator, we are interested in the eigenvectors, Φ, and eigenvalues, Λ,of the system

$$A\Phi = \Phi\Lambda\,. \tag{B.3}$$

This is intractable for our system as A is $O(n^2)$ which would require $3TB$ of memory; so we make use of the fbDMD algorithm developed by Dawson et al. (2016).

First we take the singular value decomposition

$$X \approx U\Sigma V^{*}\,, \tag{B.4}$$

where U, V are the left and right singular vectors, and Σ is a diagonal matrix containing the singular values, and $()^{*}$ is the conjugate transpose. These are truncated to m values to make up a percentage variance of the system. We can then reconstruct an approximation of A, denoted by $\tilde{A}$ using our truncated singular vectors such that

$$\tilde{A}_{forwards} = U_m^* Y V_m \Sigma_m^{-1} \,. \tag{B.5}$$

The novelty of the fbDMD algorithm is that we also compute the backward operator, $\tilde{A}_{backwards}$, which is the best fit linear operator that relates the snapshots in reverse time

$$\tilde{A}_{backwards} = U_m^* X V_m \Sigma_m^{-1} \,, \tag{B.6}$$

and then we combine the two operators to form a single operator

$$\tilde{A} = (\tilde{A}_{forwards} \tilde{A}^{-1}_{backwards})^{\frac{1}{2}} \,. \tag{B.7}$$

To reconstruct the DMD modes we solve the eigenvalue problem

$$\tilde{A} W = W \mu \,, \tag{B.8}$$

which we can use to reconstruct the high dimensional DMD modes

$$\Phi = Y V_r \Sigma_r^{-1} W \,. \tag{B.9}$$

We can now take the spectral decomposition of μ as

$$\Lambda = \ln \mu / \Delta t \,, \tag{B.10}$$

which allows us to express the whole system state as a spectral decomposition

$$x_k = \Phi \Lambda^{k-1} b \,, \tag{B.11}$$

where b are the mode-amplitudes ($b = \Phi^{\dagger} x_1$) computed, efficiently as

$$b = (W\Lambda)^{-1} \tilde{x}_1 \,, \tag{B.12}$$

where $\tilde{x}_1$ is the first mode projection of the POD.

Appendix C

Foil resolvent analysis comparison

C.1 Case

To validate the resolvent analysis results, we compare the modified NACA profile described in 4.2.1 to the NACA0012 profile used in Symon et al. (2019). Figure C.1 shows the v component of the velocity field for the resolvent analysis of the NACA0012 foil at $Re = 10,250$ and $\alpha = 0°$ for the case of Symon et al. (2019) for the experimental (a), and the data assimilated (b) cases, as well as our case (c). The flow field for our case is very similar to Symon et al. (2019) for both the experimental and data assimilated cases.

C.2 SPOD comparison

Figure C.2 shows the SPOD modes for the resolvent analysis of the NACA0012 foil at $Re = 10,250$ and $\alpha = 0°$ for the case of Symon et al. (2019) (a), as well as our case

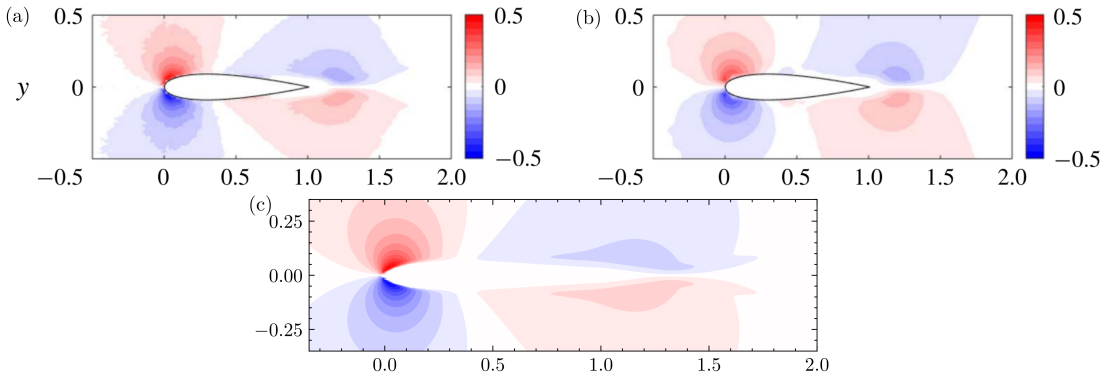

FIGURE C.1: The v component of the velocity field for the resolvent analysis of the NACA0012 foil at $Re = 10,250$ and $\alpha = 0°$ for the case of Symon et al. (2019) for the experimental (a), and the data assimilated (b) cases, as well as our case (c).

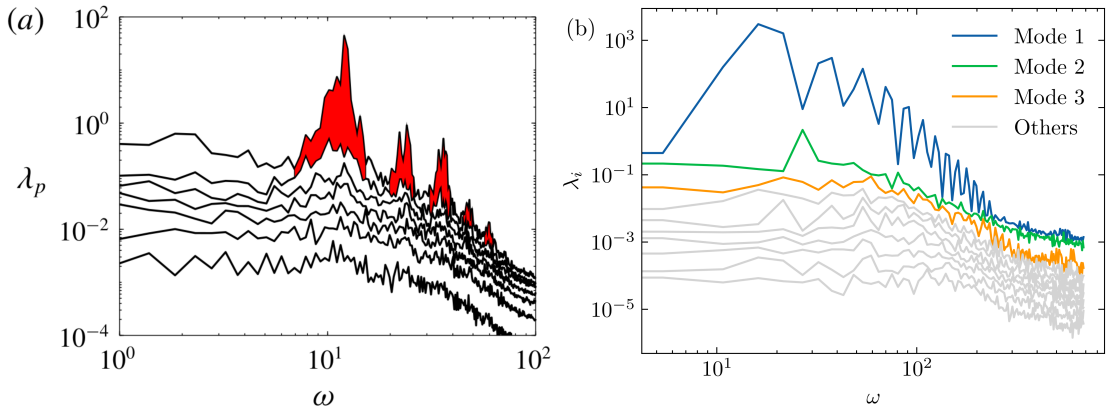

FIGURE C.2: The SPOD modes for the resolvent analysis of the NACA0012 foil at $Re = 10,250$ and $\alpha = 0°$ for the case of Symon et al. (2019) (a) and our case (b).

(b). The SPOD modes for our case are very similar to Symon et al. (2019) for both the experimental and data assimilated cases. This makes it a valid test case for our resolvent analysis.

C.3 Resolvent formulation

For Symon et al. (2019) the resolvent forulation follows a more traditional methodology. We adopt the bold notation for a vector in this derivation to avoid confusion. Consider dynamical system

$$\dot{\mathbf{q}} = \mathcal{L}_{\overline{\mathbf{q}}}\mathbf{q} + \mathbf{f}\,, \tag{C.1}$$

where the state q represents the deviations from the steady state laminar flow, or the fluctuations around a temporal mean such that $\mathbf{q} = \mathbf{Q} - \overline{\mathbf{q}}$ and $\mathbf{f}$ is the non-linear part of the Reynold's decomposition of the system. The choice of $\mathcal{L}_{\overline{\mathbf{q}}}$ depends on the specifics of the system.

The system is governed by the non-dimensional Navier-Stokes equations and the continuity equation

$$\frac{\partial \mathbf{u_i}}{\partial t} + \mathbf{u_j}\frac{\partial \mathbf{u_i}}{\partial \mathbf{x_j}} = -\frac{\partial p_i}{\partial \mathbf{x_i}} + \frac{1}{Re}\frac{\partial^2 \mathbf{u_i}}{\partial {\mathbf{x_i}}^2}\,, \tag{C.2a}$$

$$\frac{\partial \mathbf{u_i}}{\partial \mathbf{x_i}} = 0\,. \tag{C.2b}$$

If we isolate the fluctuations around a temporally stationary mean $\mathbf{q} = \overline{\mathbf{q}} + \mathbf{q}'$ we can

represent the governing equations of the disturbance as

$$\frac{\partial \mathbf{u_i'}}{\partial t} + \mathbf{u_j'}\frac{\partial \overline{\mathbf{u_i}}}{\partial \mathbf{x_j}} + \overline{\mathbf{u_j}}\frac{\partial \mathbf{u_i'}}{\partial \mathbf{x_j}} + \frac{\partial}{\partial \mathbf{x_j}}(\mathbf{u_i'u_j\prime} - \overline{\mathbf{u_i'u_j\prime}}) = -\frac{\partial p_i'}{\partial \mathbf{x_i}} + \frac{1}{Re}\frac{\partial^2 \mathbf{u_i'}}{\partial \mathbf{x_i}^2}\,, \tag{C.3a}$$

$$\frac{\partial \mathbf{u_i'}}{\partial \mathbf{x_i}} = 0\,. \tag{C.3b}$$

By collecting the linear and non-linear terms in $\mathbf{u_i}$

$$\frac{\partial \mathbf{u_i'}}{\partial t} + \mathbf{u_j'}\frac{\partial \overline{\mathbf{u_i}}}{\partial \mathbf{x_j}} + \overline{\mathbf{u_j}}\frac{\partial \mathbf{u_i'}}{\partial \mathbf{x_j}} + \frac{\partial p_i'}{\partial \mathbf{x_i}} - \frac{1}{Re}\frac{\partial^2 \mathbf{u_i'}}{\partial \mathbf{x_i}^2} = \frac{\partial}{\partial \mathbf{x_j}}(\mathbf{u_i'u_j\prime} - \overline{\mathbf{u_i'u_j\prime}})\,, \tag{C.4a}$$

$$\frac{\partial \mathbf{u_i'}}{\partial t} + \mathbf{u_j'}\frac{\partial \overline{\mathbf{u_i}}}{\partial \mathbf{x_j}} + \overline{\mathbf{u_j}}\frac{\partial \mathbf{u_i'}}{\partial \mathbf{x_j}} + \frac{\partial p_i'}{\partial \mathbf{x_i}} - \frac{1}{Re}\frac{\partial^2 \mathbf{u_i'}}{\partial \mathbf{x_i}^2} = \mathbf{f'} \tag{C.4b}$$

$$\mathcal{L}_{\overline{\mathbf{q}}}(\mathbf{q'}) = \mathbf{f'}\,, \tag{C.4c}$$

where $\mathbf{q'} = (\mathbf{u'}, p')$ as the sum of its Fourier modes

$$[\mathbf{u'}, p'](\mathbf{x}, t) = \int_{-\infty}^{\infty} [\mathcal{F}_{\mathbf{u}}, \hat{p}](x) e^{-i\omega t} d\omega\,. \tag{C.5}$$

For the homogenous part,

$$\frac{\partial \mathcal{F}_{\mathbf{u_i}} e^{-i\omega t} d\omega}{\partial t} = -\Big(\mathcal{F}_{\mathbf{u_j}}\frac{\partial \overline{\mathbf{u_i}}}{\partial \mathbf{x_j}} + \overline{\mathbf{u_j}}\frac{\partial \mathcal{F}_{\mathbf{u_i}}}{\partial \mathbf{x_j}} + \frac{\partial \hat{p}_i}{\partial \mathbf{x_i}} - \frac{1}{Re}\frac{\partial^2 \mathcal{F}_{\mathbf{u_i}}}{\partial \mathbf{x_i}^2}\Big) e^{-i\omega t} d\omega \tag{C.6}$$

restrict to velocity subspace

$$-i\omega \mathcal{F}_{\mathbf{u_i}} = -\Big(\mathcal{F}_{\mathbf{u_j}}\frac{\partial \overline{\mathbf{u_i}}}{\partial \mathbf{x_j}} + \overline{\mathbf{u_j}}\frac{\partial \mathcal{F}_{\mathbf{u_i}}}{\partial \mathbf{x_j}} - \frac{1}{Re}\frac{\partial^2 \mathcal{F}_{\mathbf{u_i}}}{\partial \mathbf{x_i}^2}\Big) \tag{C.7}$$

This forms the eigenvalue problem

$$-i\omega \mathcal{F}_{\mathbf{u}} = -\Big(()\frac{\partial \overline{\mathbf{u_i}}}{\partial \mathbf{x_j}} + \overline{\mathbf{u_j}}\frac{\partial ()}{\partial \mathbf{x_j}} - \frac{1}{Re}\frac{\partial^2 ()}{\partial \mathbf{x_i}^2}\Big)\mathcal{F}_{\mathbf{u}} \tag{C.8}$$

$$-i\omega \mathcal{F}_{\mathbf{u}} = \mathcal{L}_{\overline{\mathbf{u}}}\mathcal{F}_{\mathbf{u}}\,, \tag{C.9}$$

which is transformed to the Fourier space, such that

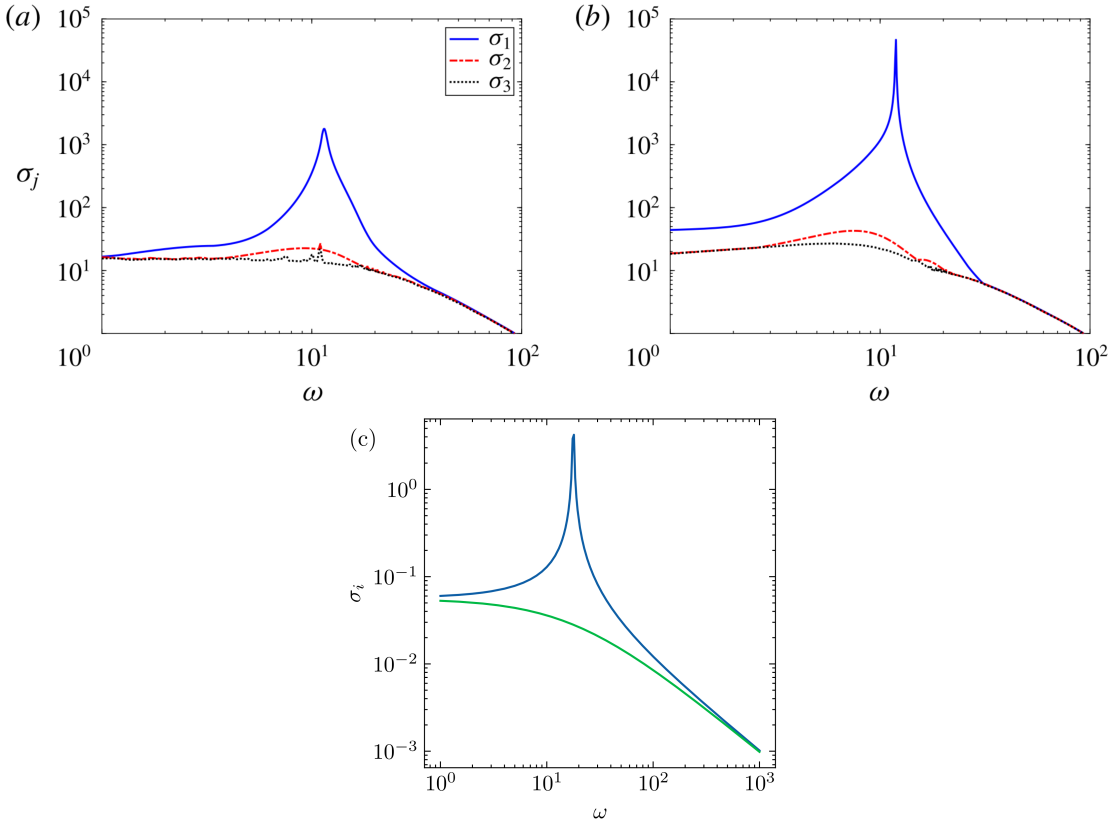

FIGURE C.3: The gain for the resolvent analysis of the NACA0012 foil at $Re = 10,250$ and $\alpha = 0^\circ$ for the case of Symon et al. (2019) for the experimental (a), and the data assimilated (b) cases, as well as our case (c).

$$-i\omega\hat{\mathbf{q}} = \mathcal{L}_{\bar{\mathbf{q}}}\hat{\mathbf{q}} + \hat{\mathbf{f}} \tag{C.10}$$

so

$$\hat{\mathbf{q}} = \mathbf{H}(\omega)^{-1}\hat{\mathbf{f}} \tag{C.11}$$

where $\mathbf{H}(\omega) = (-i\omega - \mathcal{L}_{\bar{\mathbf{q}}})$ is the resolvent operator. We can analyse using the SVD so

$$\mathbf{H}(\omega) = \hat{\Psi}\hat{\Sigma}\hat{\Phi}^* \tag{C.12}$$

where $\hat{\Psi}$ and $\hat{\Phi}$ are the left and right singular vectors, and $\hat{\Sigma}$ is the singular value matrix.

C.4 Gain comparison

We can thus compare the method described in 4.2.5 to the method described here. We use a DMD basis with 2 modes to mimic the traditional formulation that only uncorporates

$\overline{\vec{u}}$. The results are shown in figure C.3. We find that the results are very similar, with peak gain corresponding to the same frequency as the peak SPOD mode. The main difference is the magnitude of the modes, which is likely due to differences in normalisation.

Appendix D

Foil convergence analysis

D.1 Shape modification of the NACA0012 foil

We alter the nose of a NACA0012 foil to mimic the general shape of a fish. The foil is modified by subtracting the shape of a sigmoid function from the NACA0012 profile. We then fit an $O(10)$ polynomial to the points, which we use to define the body set for the CFD simulations.

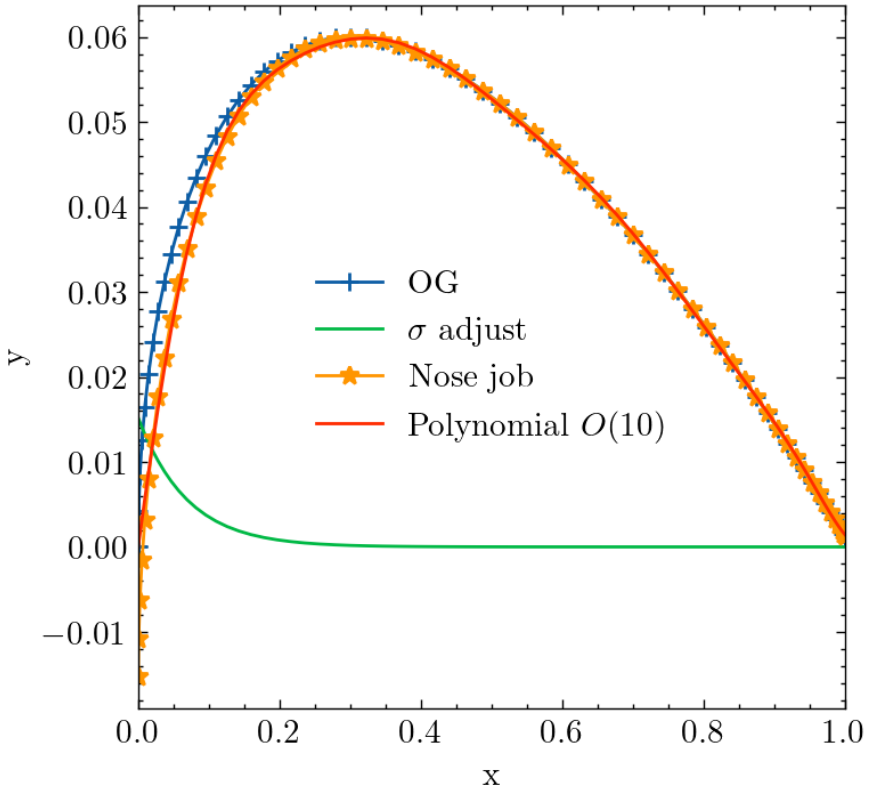

FIGURE D.1: The shape modification of the NACA0012 foil.

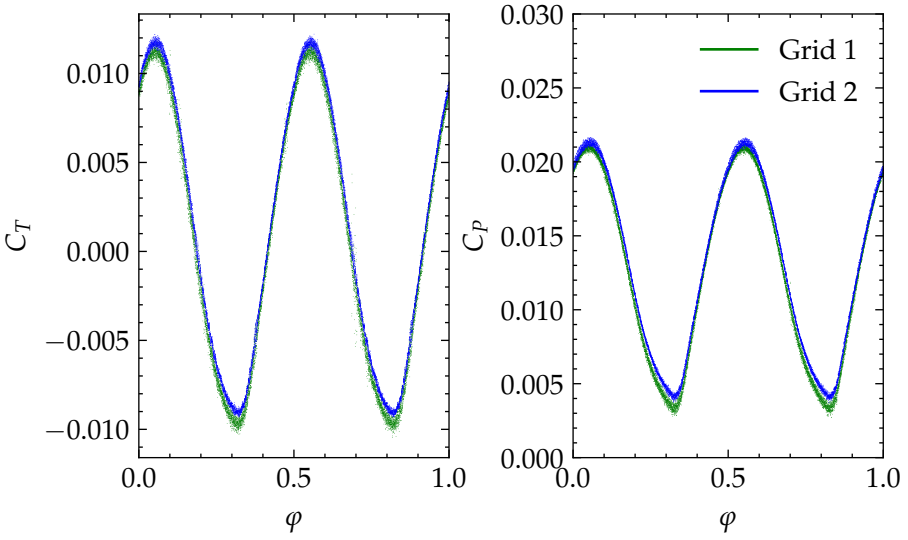

FIGURE D.2: The domain study.

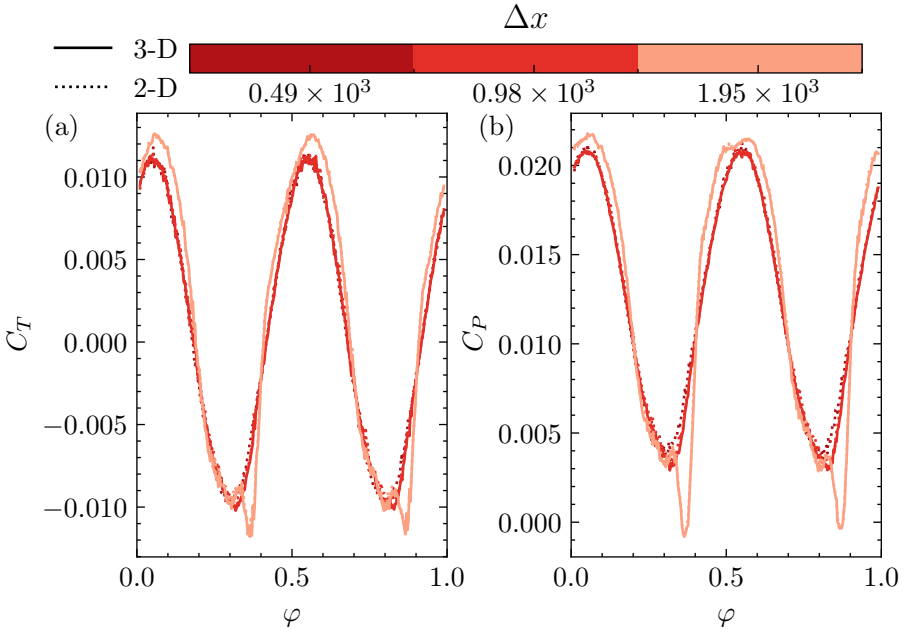

FIGURE D.3: The resolution convergence study for three grid resolutions spanning our working resolution.

D.2 Domain study

For the domain study we compare the power for two differently sized domains. The first domain is the same as the one used in the main text, and the second domain is much larger, with dimensions $x \in [-10, 10]$ and $y \in [-10, 10]$ totalling $\vec{N} =$ points

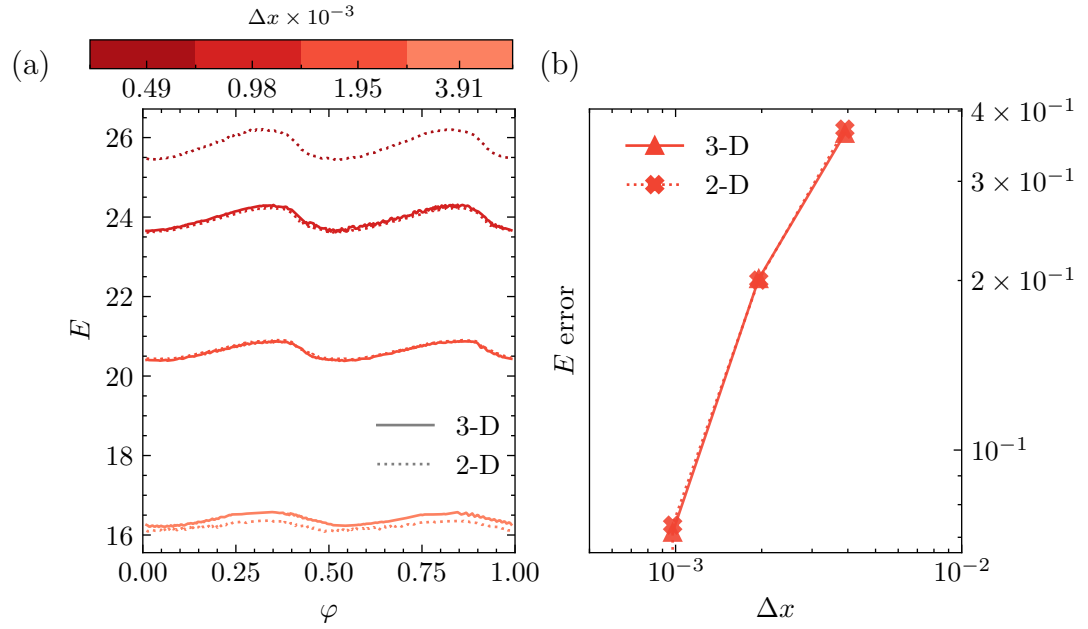

FIGURE D.4: Resolution convergence study for enstrophy showing the time series (a), and the log-log plot of the enstrophy error compared to the highest resolution (b).

D.3 Resolution convergence

For the resolution convergence, we demonstrate that both thrust and power converge with grid resolution. Employing the same domain as in the main text, we vary the grid resolution, covering our working range, to confirm that our results are independent of increased resolution. This is facilitated by illustrating that the two- and three-dimensional simulations yield consistent forces, as depicted by overlaying the two-dimensional results onto the three-dimensional results in figure D.3. Due to feasibility constraints, we cannot run the three-dimensional simulations at the highest resolution, hence we use the two-dimensional results to validate the sufficiency of the highest resolution.

The results, presented in figure D.3, reveal that the lowest resolution leads to a non-physical drop in thrust and power, rendering it unsuitable. In contrast, the highest two resolutions produce results that closely align.

To bolster confidence in our numerical results, we compare our most sensitive metric, enstrophy. Similar to the previous analysis, we demonstrate that the two- and three-dimensional simulations present comparable enstrophy, as shown by superimposing the two-dimensional results onto the three-dimensional results in figure D.4. These findings, displayed in figure D.4, indicate that enstrophy converges with grid resolution. We observe a monotonic convergence to 7%, affirming that our results are numerically stable.

Furthermore, we have ensured that the geometry is adequately resolved. Consequently, we maintain a minimum of 8 grid points across the amplitude of the roughness elements and across the wavelength of the bump. For this egg-carton roughness, this geometric resolution has been shown as sufficient in chapter 2.

References

Afroz, F., Lang, A., Habegger, M. L., Motta, P., and Hueter, R. (2016). Experimental study of laminar and turbulent boundary layer separation control of shark skin. *Bioinspiration & biomimetics*, 12(1):16009. Publisher: IOP Publishing.

Anderson, J. M. (1996). *Vorticity control for efficient propulsion*. PhD thesis, Massachusetts Institute of Technology.

Anderson, W., Barros, J. M., Christensen, K. T., and Awasthi, A. (2015). Numerical and experimental study of mechanisms responsible for turbulent secondary flows in boundary layer flows over spanwise heterogeneous roughness. *Journal of Fluid Mechanics*, 768:316–347. Publisher: Cambridge University Press.

Ankhelyi, M. V., Wainwright, D. K., and Lauder, G. V. (2018). Diversity of dermal denticle structure in sharks: Skin surface roughness and three-dimensional morphology. *Journal of Morphology*, 279(8):1132–1154.

Bale, R., Hao, M., Bhalla, A. P. S., and Patankar, N. A. (2014). Energy efficiency and allometry of movement of swimming and flying animals. *Proceedings of the National Academy of Sciences*, 111(21):7517–7521.

Barros, J. M. and Christensen, K. T. (2014). Observations of turbulent secondary flows in a rough-wall boundary layer. *Journal of Fluid Mechanics*, 748(2):R1. Publisher: Cambridge University Press.

Bechert, D. W., Bruse, M., and Hage, W. (2000a). Experiments with three-dimensional riblets as an idealized model of shark skin. *Experiments in fluids*, 28(5):403–412. Publisher: Springer.

Bechert, D. W., Bruse, M., and Hage, W. (2000b). Experiments with three-dimensional riblets as an idealized model of shark skin. *Experiments in Fluids*, 28(5):403–412.

Bechert, D. W., Bruse, M., Hage, W., Hoeven, J. G. T. V. D., and Hoppe, G. (1997). Experiments on drag-reducing surfaces and their optimization with an adjustable geometry. *Journal of Fluid Mechanics*, 338:59–87. Publisher: Cambridge University Press.

Bechert, D. W., Bruse, M., Hage, W., and Meyer, R. (2000c). Fluid mechanics of biological surfaces and their technological application. *naturwissenschaften*, 87(4):157–171. Publisher: Springer.

Bechert, D. W., Hoppe, G., and Reif, W. E. (1985). On the drag reduction of the shark skin. *AIAA 23rd Aerospace Sciences Meeting, 1985*. Publisher: American Institute of Aeronautics and Astronautics Inc, AIAA.

Boomsma, A. and Sotiropoulos, F. (2016). Direct numerical simulation of sharkskin denticles in turbulent channel flow. *Phys. Fluids*, 28:35106.

Borazjani, I. and Sotiropoulos, F. (2008). Numerical investigation of the hydrodynamics of carangiform swimming in the transitional and inertial flow regimes. *Journal of Experimental Biology*, 211(10):1541–1558. Publisher: The Company of Biologists.

Borazjani, I. and Sotiropoulos, F. (2010). On the role of form and kinematics on the hydrodynamics of self-propelled body/caudal fin swimming. *Journal of Experimental Biology*, 213(1):89–107.

Bottaro, A., Soueid, H., and Galletti, B. (2006). Formation of Secondary Vortices in Turbulent Square-Duct Flow. *AIAA Journal*, 44(4):803–811.

Brent, R. P. (1971). An algorithm with guaranteed convergence for finding a zero of a function. *The Computer Journal*, 14(4):422–425. Publisher: Oxford Academic.

Carling, J., Williams, T. L., and Bowtell, G. (1998). Self-propelled anguilliform swimming: simultaneous solution of the two-dimensional navier–stokes equations and Newton's laws of motion. *Journal of Experimental Biology*, 201(23):3143–3166.

Chan, L., Macdonald, M., Chung, D., Hutchins, N., and Ooi, A. (2015). A systematic investigation of roughness height and wavelength in turbulent pipe flow in the transitionally rough regime. *J. Fluid Mech*, 771:743–777. Publisher: Cambridge University Press.

Choi, H., Moin, P., and Kim, J. (1994). Active turbulence control for drag reduction in wall-bounded flows. *Journal of Fluid Mechanics*, 262:75–110.

Chorin, A. J. (1968). Numerical solution of the Navier-Stokes equations. *Mathematics of Computation*, 22(104):745–762. Publisher: American Mathematical Society (AMS).

Chung, D., Hutchins, N., Schultz, M. P., and Flack, K. A. (2021). Predicting the Drag of Rough Surfaces. *Annual Review of Fluid Mechanics*, 53:439–471.

Cui, G., Pan, C., Wu, D., Ye, Q., and Wang, J. (2019). Effect of drag reducing riblet surface on coherent structure in turbulent boundary layer. *Chinese Journal of Aeronautics*, 32(11):2433–2442. Publisher: Elsevier.

Dawson, S. T., Hemati, M. S., Williams, M. O., and Rowley, C. W. (2016). Characterizing and correcting for the effect of sensor noise in the dynamic mode decomposition. *Experiments in Fluids*, 57(3):1–19. arXiv: 1507.02264 Publisher: Springer Berlin Heidelberg.

Demo, N., Tezzele, M., and Rozza, G. (2018). PyDMD: Python Dynamic Mode Decomposition. *The Journal of Open Source Software*, 3(22):530.

Dewey, P. A., Carriou, A., and Smits, A. J. (2012). On the relationship between efficiency and wake structure of a batoid-inspired oscillating fin. *Journal of Fluid Mechanics*, 691:245–266.

Di Santo, V., Goerig, E., Wainwright, D. K., Akanyeti, O., Liao, J. C., Castro-Santos, T., and Lauder, G. V. (2021). Convergence of undulatory swimming kinematics across a diversity of fishes. *Proceedings of the National Academy of Sciences of the United States of America*, 118(49). Publisher: National Academy of Sciences.

Domel, A. G., Saadat, M., Weaver, J. C., Haj-Hariri, H., Bertoldi, K., and Lauder, G. V. (2018). Shark skin-inspired designs that improve aerodynamic performance. *Journal of the Royal Society Interface*, 15(139):1–9.

Dong, G. J. and Lu, X. Y. (2007). Characteristics of flow over traveling wavy foils in a side-by-side arrangement. *Physics of Fluids*, 19(5):057107. Publisher: American Institute of Physics Inc.

Drucker, E. G. (2002). Experimental Hydrodynamics of Fish Locomotion: Functional Insights from Wake Visualization. *Integrative and Comparative Biology*, 42(2):243–257.

Eloy, C. (2012). Optimal Strouhal number for swimming animals. *Journal of Fluids and Structures*, 30:205–218. arXiv: 1102.0223 Publisher: Elsevier.

Ferziger, J. H., Perić, M., and Street, R. L. (2019). *Computational Methods for Fluid Dynamics*. Springer. Google-Books-ID: i9CpDwAAQBAJ.

Flack, K. A. and Schultz, M. P. (2010). Review of hydraulic roughness scales in the fully rough regime. *Journal of Fluids Engineering, Transactions of the ASME*, 132(4):0412031–04120310. Publisher: American Society of Mechanical Engineers Digital Collection.

Flack, K. A. and Schultz, M. P. (2014). Roughness effects on wall-bounded turbulent flowsa). *Physics of Fluids*, 26(10):101305. Publisher: American Institute of PhysicsAIP.

Fransson, J. H. M., Talamelli, A., Brandt, L., and Cossu, C. (2006). Delaying Transition to Turbulence by a Passive Mechanism. *Physical Review Letters*, 96(6):064501.

Ganju, S., Bailey, S. C. C., Brehm, C., Ganju, S., Bailey, S. C. C., and Brehm, C. (2022). Amplitude and wavelength scaling of sinusoidal roughness effects in turbulent channel flow at fixed Re = 720. *J. Fluid Mech*, 937:22.

García-Mayoral, R., Gómez-De-Segura, G., and Fairhall, C. T. (2019). The control of near-wall turbulence through surface texturing. *Fluid Dynamics Research*, 51(1):011410. Publisher: IOP Publishing.

Goza, A. and Colonius, T. (2018). Modal decomposition of fluid–structure interaction with application to flag flapping. *Journal of Fluids and Structures*, 81:728–737. arXiv: 1711.03040 Publisher: Academic Press.

Grass, A. J. (1971). Structural features of turbulent flow over smooth and rough boundaries. *Journal of Fluid Mechanics*, 50(2):233–255.

Gray, J. (1936). Studies in Animal Locomotion VI. The Propulsive Powers of the Dolphin. *Journal of Experimental Biology*, 13(2):192–199. Publisher: The Company of Biologists.

Guo, P., Zhang, K., Yasuda, Y., Yang, W., Galipon, J., and Rival, D. E. (2021). On the influence of biomimetic shark skin in dynamic flow separation. *Bioinspiration & Biomimetics*, 16(3):034001. Publisher: IOP Publishing.

Hebrank, M. R. (1980). Mechanical properties and locomotor functions of eel skin. *The Biological Bulletin*, 158(1):58–68.

Hendrickson, K., Weymouth, G. D., Yu, X., and Yue, D. K. (2019). Wake behind a three-dimensional dry transom stern. Part 1. Flow structure and large-scale air entrainment. *Journal of Fluid Mechanics*, 875:854–883. Publisher: Cambridge University Press.

Herrmann, B., Baddoo, P. J., Semaan, R., Brunton, S. L., and McKeon, B. J. (2021). Data-Driven Resolvent Analysis.

Hess, F. and Videler, J. J. (1984). Fast Continuous Swimming of Saithe (*Pollachius Virens*): a Dynamic Analysis of Bending Moments and Muscle Power. *Journal of Experimental Biology*, 109(1):229–251.

Hinze, J. O. (1967). Secondary Currents in Wall Turbulence. *The Physics of Fluids*, 10(9):S122. Publisher: American Institute of PhysicsAIP.

Hinze, J. O. (1973). Experimental investigation on secondary currents in the turbulent flow through a straight conduit. *Applied Scientific Research 1973 28:1*, 28(1):453–465. Publisher: Springer.

Hultmark, M., Leftwich, M., and Smits, A. J. (2007). Flowfield measurements in the wake of a robotic lamprey. *Experiments in Fluids*, 43(5):683–690.

Hunt, J. C. R., Wray, A. A., Moin, P., Wray, A. A., and Moin, P. (1988). eddies, streams, and convergence zones in turbulent flows. *Studying Turbulence Using Numerical Simulation Databases, 2. Proceedings of the 1988 Summer Program*.

Jafari, A., McKeon, B. J., and Arjomandi, M. (2023). Frequency-Tuned Surfaces for Passive Control of Wall-Bounded Turbulent Flow – A Resolvent Analysis Study.

Jiménez, J. (2004). Turbulent flows over rough walls. *Annual Review of Fluid Mechanics*, 36(1991):173–196.

Johann Nikuradse (1926). Untersuchung über die Geschwindigkeitsverteilung. *ZAMM - Journal of Applied Mathematics and Mechanics / Zeitschrift für Angewandte Mathematik und Mechanik*, 6(6):503–503. Publisher: John Wiley & Sons, Ltd.

Jovanović, M. R. and Bamieh, B. (2005). Componentwise energy amplification in channel flows. *Journal of Fluid Mechanics*, 534:145–183.

Lang, A. W., Motta, P., Hidalgo, P., and Westcott, M. (2008). Bristled shark skin: a microgeometry for boundary layer control? *Bioinspiration & Biomimetics*, 3(4):046005. Publisher: IOP Publishing.

Lauber, M., Weymouth, G. D., and Limbert, G. (2022). Immersed Boundary Simulations of Flows Driven by Moving Thin Membranes. *Physics of Fluids*. arXiv: 2110.06535v1.

Lauder, G. V., Wainwright, D. K., Domel, A. G., Weaver, J. C., Wen, L., and Bertoldi, K. (2016). Structure, biomimetics, and fluid dynamics of fish skin surfaces. *Physical Review Fluids*, 1(6):1–18.

Leonard, B. P. (1979). A stable and accurate convective modelling procedure based on quadratic upstream interpolation. *Computer Methods in Applied Mechanics and Engineering*, 19(1):59–98. Publisher: North-Holland.

Lighthill, M. J. (1960). Note on the swimming of slender fish. *Journal of Fluid Mechanics*, 9(2):305–317. Publisher: Cambridge University Press.

Lighthill, M. J. (1971). Large-amplitude elongated-body theory of fish locomotion. *Proceedings of the Royal Society of London. Series B. Biological Sciences*, 179(1055):125–138. Publisher: The Royal Society London.

Lin, J. C. (2002). Review of research on low-profile vortex generators to control boundary-layer separation. *Progress in Aerospace Sciences*, 38(4-5):389–420. Publisher: Pergamon.

Lin, J. C., Robinson, S. K., McGhee, R. J., and Valarezo, W. O. (1994). Separation control on high-lift airfoils via micro-vortex generators. *Journal of Aircraft*, 31(6):1317–1323.

Lucas, K. N., Thornycroft, P. J., Gemmell, B. J., Colin, S. P., Costello, J. H., and Lauder, G. V. (2015). Effects of non-uniform stiffness on the swimming performance of a passively-flexing, fish-like foil model. *Bioinspiration & Biomimetics*, 10(5):056019. Publisher: IOP Publishing.

Ludwig Prandtl (1926). Über die ausgebildete Turbulenz. *Verhandl. des II. Int. Kongr. für Techn. Mech.*, pages 62–75.

Luhar, M., Sharma, A. S., and McKeon, B. J. (2014). Opposition control within the resolvent analysis framework. *Journal of Fluid Mechanics*, 749:597–626.

Ma, G. Z., Xu, C. X., Sung, H. J., and Huang, W. X. (2020). Scaling of rough-wall turbulence by the roughness height and steepness. *Journal of Fluid Mechanics*, 900:R7. Publisher: Cambridge University Press.

Maertens, A. P., Gao, A., and Triantafyllou, M. S. (2017). Optimal undulatory swimming for a single fish-like body and for a pair of interactingÂ swimmers. *Journal of Fluid Mechanics*, 813:301–345. arXiv: 1604.01065.

Maertens, A. P. and Weymouth, G. D. (2015). Accurate Cartesian-grid simulations of near-body flows at intermediate Reynolds numbers. *Computer Methods in Applied Mechanics and Engineering*, 283:106–129. Publisher: Elsevier B.V.

Massey, J., Ganapathisubramani, B., and Weymouth, G. (2023). A systematic investigation into the effect of roughness on self-propelled swimming plates. *Journal of Fluid Mechanics*, 971:A39.

McKeon, B. J. and Sharma, A. S. (2010). A critical-layer framework for turbulent pipe flow. *Journal of Fluid Mechanics*, 658:336–382.

Menon, K. and Mittal, R. (2020). Dynamic mode decomposition based analysis of flow over a sinusoidally pitching airfoil. *Journal of Fluids and Structures*, 94. arXiv: 1911.05768 Publisher: Academic Press.

Moody and F., L. (1944). Friction factors for pipe flow. *Trans. ASME*, 66:671–684.

Motta, P. J. (1977). Anatomy and Functional Morphology of Dermal Collagen Fibers in Sharks. (1977):454–464.

Muscutt, L. E., Weymouth, G. D., and Ganapathisubramani, B. (2017). Performance augmentation mechanism of in-line tandem flapping foils. *Journal of Fluid Mechanics*, 827:484–505. Publisher: Cambridge University Press.

Muthuramalingam, M., Puckert, D. K., Rist, U., and Bruecker, C. (2020). Transition delay using biomimetic fish scale arrays. *Scientific Reports*, 10(1).

Muthuramalingam, M., Villemin, L. S., and Bruecker, C. (2019). Streak formation in flow over biomimetic fish scale arrays. *Journal of Experimental Biology*, page jeb.205963.

Napoli, E., Armenio, V., and De Marchis, M. (2008). The effect of the slope of irregularly distributed roughness elements on turbulent wall-bounded flows. *Journal of Fluid Mechanics*, 613:385–394. Publisher: Cambridge University Press.

Nauen, J. C. and Lauder, G. V. (2002). Hydrodynamics of caudal fin locomotion by chub mackerel, *Scomber japonicus* (Scombridae). *Journal of Experimental Biology*, 205(12):1709–1724.

NRT Response Committee (2011). On Scene Coordinator Report Deepwater Horizon Oil Spill. Technical report.

Nugroho, B., Hutchins, N., and Monty, J. P. (2013). Large-scale spanwise periodicity in a turbulent boundary layer induced by highly ordered and directional surface roughness. *International Journal of Heat and Fluid Flow*, 41:90–102. Publisher: Elsevier.

Oeffner, J. and Lauder, G. V. (2012). The hydrodynamic function of shark skin and two biomimetic applications. *Journal of Experimental Biology*, 215(5):785–795. Publisher: The Company of Biologists.

Orr, W. M. (1907). The Stability or Instability of the Steady Motions of a Perfect Liquid and of a Viscous Liquid. Part II: A Viscous Liquid. *Componentwise energy amplification in channel flows*, 27:69–138.

Orszag, S. A. (1971). Accurate solution of the Orr–Sommerfeld stability equation. *Journal of Fluid Mechanics*, 50(4):689–703.

Park, S.-R. and Wallace, J. M. (1994). Flow Alteration and Drag Reduction by Riblets in a Turbulent Boundary Layer. *AIAA JOURNAL*, 32(1).

Perkins, H. J. (1970). The formation of streamwise vorticity in turbulent flow. *Journal of Fluid Mechanics*, 44(4):721–740. Publisher: Cambridge University Press.

Peskin, C. S. (1972). Flow patterns around heart valves: A numerical method. *Journal of Computational Physics*, 10(2):252–271.

Quinn, D. B., Lauder, G. V., and Smits, A. J. (2014). Scaling the propulsive performance of heaving flexible panels. *Journal of Fluid Mechanics*, 738:250–267. Publisher: Cambridge University Press.

R García-Mayoral, J. J. (2011). Drag reduction by riblets. *Philos Trans R Soc A*, 369(1940):1412. Publisher: Royal Society.

Raschi, W. and Musick, J. (1984). Hydrodynamic Aspects of Shark Scales. *Reports*.

Reif, W. (1985). Squamation and ecology of sharks. Courier forschungs-Institut senckenberg. *Cour. Forsch.-Inst. Senchenberg. Frankfurt aM*.

Ribeiro, J. H. M., Yeh, C.-A., and Taira, K. (2020). Randomized resolvent analysis. *Physical Review Fluids*, 5(3):033902.

Rouhi, A., Endrikat, S., Modesti, D., Sandberg, R. D., Oda, T., Tanimoto, K., Hutchins, N., and Chung, D. (2022). Riblet-generated flow mechanisms that lead to local breaking of Reynolds analogy. *J. Fluid Mech*, 951:45.

Saadat, M., Fish, F. E., Domel, A. G., Di Santo, V., Lauder, G. V., and Haj-Hariri, H. (2017). On the rules for aquatic locomotion. *Physical Review Fluids*, 2(8):083102.

Santos, L. M., Lang, A., Wahidi, R., Bonacci, A., Devey, S., Parsons, J., Santos, L. M., Lang, A., Wahidi, R., Bonacci, A., Gautam, S., Devey, S., and Parsons, J. (2021). Passive

Separation Control of Shortfin Mako Shark Skin in a Turbulent Boundary Layer. *Experimental Thermal and Fluid Science*, page 110433. Publisher: Elsevier Inc.

Schlichting, H. (1936). Experimentelle Untersuchungen zum Rauhigkeitsproblem. *Ingenieur-Archiv*, 7(1):1–34. Publisher: Springer-Verlag.

Schmid, P. J. (2010). Dynamic mode decomposition of numerical and experimental data. *Journal of Fluid Mechanics*, 656:5–28.

Schnipper, T., Andersen, A., and Bohr, T. (2009). Vortex wakes of a flapping foil. *Journal of Fluid Mechanics*, 633:411–423. Publisher: Cambridge University Press.

Sommerfield, A. (1908). Ein Beitrag zur hydrodynamischen Erklarung der turbulenten Flussigkeisbewegung. *Atti Congr. Int. Math. 4th Rome*.

Symon, S., Sipp, D., and McKeon, B. J. (2019). A tale of two airfoils: resolvent-based modelling of an oscillator versus an amplifier from an experimental mean. *Journal of Fluid Mechanics*, 881:51–83.

Thekkethil, N., Sharma, A., and Agrawal, A. (2018). Unified hydrodynamics study for various types of fishes-like undulating rigid hydrofoil in a free stream flow. *Physics of Fluids*, 30(7):077107. Publisher: American Institute of Physics Inc.

Trefethen, L. N., Trefethen, A. E., Reddy, S. C., and Driscoll, T. A. (1993). Hydrodynamic Stability Without Eigenvalues.

Triantafyllou, G. S., Triantafyllou, M. S., and Grosenbaugh, M. A. (1993). Optimal Thrust Development in Oscillating Foils with Application to Fish Propulsion. *Journal of Fluids and Structures*, 7(2):205–224. Publisher: Academic Press.

Triantafyllou, M. S., Triantafyllou, G. S., and Gopalkrishnan, R. (1991). Wake mechanics for thrust generation in oscillating foils. *Physics of Fluids A: Fluid Dynamics*, 3(12):2835. Publisher: American Institute of PhysicsAIP.

Tytell, E. D. (2007). Do trout swim better than eels? Challenges for estimating performance based on the wake of self-propelled bodies. *Experiments in Fluids*, 43(5):701–712.

Tytell, E. D. and Lauder, G. V. (2004). The hydrodynamics of eel swimming. *Journal of Experimental Biology*, 207(11):1825–1841.

Ulrike K Müller, Joris Smit, Eize J. Stamhuis, and John J. Videler (2001). How the body contributes to the wake in undulatory fish swimming: flow fields of a swimming eel.

Uzun, A. and Malik, M. R. (2021). Simulation of a turbulent flow subjected to favorable and adverse pressure gradients. *Theoretical and Computational Fluid Dynamics*, 35(3):293–329.

Vanderwel, C. and Ganapathisubramani, B. (2015). Effects of spanwise spacing on large-scale secondary flows in rough-wall turbulent boundary layers. *Journal of Fluid Mechanics*, 774:R2. Publisher: Cambridge University Press.

Vilumbrales-Garcia, R., Kurt, M., Weymouth, G. D., and Ganapathisubramani, B. (2024). Effects of surface roughness on the propulsive performance of pitching foils. *Journal of Fluid Mechanics*, 982:A1.

Von Deyn, L. H., Gatti, D., Frohnapfel, B., Von Deyn, L. H., Gatti, D., and Frohnapfel, B. (2022). From drag-reducing riblets to drag-increasing ridges. *J. Fluid Mech*, 951:16.

Wainwright, D. K. and Lauder, G. V. (2016). Three-dimensional analysis of scale morphology in bluegill sunfish, Lepomis macrochirus. *Zoology*, 119(3):182–195.

Wainwright, D. K., Lauder, G. V., and Weaver, J. C. (2017). Imaging biological surface topography *in situ* and *in vivo*. *Methods in Ecology and Evolution*, 8(11):1626–1638.

Wainwright, S. A., Vosburgh, F., and Hebrank, J. H. (1978). Shark Skin: Function in Locomotion. 202.

Walsh, M. (1982). Turbulent boundary layer drag reduction using riblets. *AIAA*. Publisher: American Institute of Aeronautics and Astronautics (AIAA).

Wen, L., Weaver, J. C., and Lauder, G. V. (2014). Biomimetic shark skin: design, fabrication and hydrodynamic function. *Journal of Experimental Biology*, 217(10):1656–1666. Publisher: Company of Biologists Ltd.

Weymouth, G. D. and Yue, D. K. (2011). Boundary data immersion method for Cartesian-grid simulations of fluid-body interaction problems. *Journal of Computational Physics*, 230(16):6233–6247. Publisher: Elsevier Inc.

Williams, M. O., Kevrekidis, I. G., and Rowley, C. W. (2015). A Data–Driven Approximation of the Koopman Operator: Extending Dynamic Mode Decomposition. *Journal of Nonlinear Science*, 25(6):1307–1346. arXiv: 1408.4408 Publisher: Springer US.

Wu, L., Jiao, Z., Song, Y., Liu, C., Wang, H., and Yan, Y. (2018). Experimental investigations on drag-reduction characteristics of bionic surface with water-trapping microstructures of fish scales. *Scientific Reports*, 8(1):12186.

Yeh, C.-A. and Taira, K. (2019). Resolvent-analysis-based design of airfoil separation control. *Journal of Fluid Mechanics*, 867:572–610.

Zhu, Q., Wolfgang, M. J., Yue, D. K. P., and Triantafyllou, M. S. (2002). Three-dimensional flow structures and vorticity control in fish-like swimming. *Journal of Fluid Mechanics*, 468:1–28. Publisher: Cambridge University Press.

Zurman-Nasution, A. N., Ganapathisubramani, B., and Weymouth, G. D. (2020). Influence of three-dimensionality on propulsive flapping. *Journal of Fluid Mechanics*, 886.